Dynamics of confined biofilaments

Gi-Moon Nam

Dynamics of confined biofilaments

Thèse présentée par

Gi-Moon Nam

Pour obtenir le titre de Docteur de l'Université de Strasbourg

Discipline: Physique

28 Septembre 2012

Membres du Jury:

Directeur de thèse:	**N.-K. Lee** Professeur, Sejong University
Directeur de thèse:	**A. Johner** Directeur de recherche, ICS, Strasbourg
Co-directeur de thèse:	**I. M. Kulić** Chargé de recherche, ICS, Strasbourg
Examinateur:	**T. Charitat** Professeur, UdS, Strasbourg
Examinateur:	**H.-C. Jeong** Professeur, Sejong University
Rapporteur externe:	**J.-F. Joanny** Professeur, Université Paris VI
Rapporteur externe:	**A. Ott** Professeur, Universität des Saarlandes
Examinateur:	**D. Riveline** Directeur de recherche, ISIS, Strasbourg

UNIVERSITÉ DE STRASBOURG

INSTITUT Charles SADRON CNRS - UdS - STRASBOURG

Résumé

Cette thèse est consacrée à la mécanique et à la mécanique statistique de bio-filaments/-polymères et de leur modèle le plus répandu le Worm-Like Chain. Nous calculons en détail quelques propriétés du modèle WLC nous en illustrons les faiblesses et présentons des modèles plus élaborés. Tout au long de ce travail, les filaments sont souvent confinés, par exemple au voisinage d'un plan focal d'observation, entre deux plans rapprochés ou sur des chemins étroits définis par des obstacles, cela aide à révéler leurs propriétés mécaniques.

Les biofilaments considérés sont des structures auto assemblées d'unités nanométriques comme le dimère de tubuline dans les microtubules (MTs), la G-actine dans les filaments et les gels d'actine ou de petites entités (comme la vimentine) associées dans les filaments intermédiaires (IFs). Cette assemblage est quelquefois hiérarchisé au sens que le protofilament conserve en partie son identité dans le microtubule associé, le cas de l'ADN double brin comprenant deux polyméres covalents (les simples brins) associés dans la double hélice étant extrême. Bien que ces filaments aient des structures compliquées et soient souvent intrigants du point de vue de la chimie et de la physique des polymères, le vrai défit reste le lien avec le rôle subtil qu'ils jouent dans la cellule.

Les biopolyméres les plus connus, l'ADN et l'ARN portent de l'information génétique et adoptent des structures bien définies dans les conditions physiologiques. L'ADN consiste en une séquence de paires de bases ou nucléotides empilées de manière hélicoïdale et connectées entre elles par des squelettes covalents. Les biopolymères du cytosquelette l'actine les microtubules et les filaments intermédiaires sont impliqués dans la forme et la motilité de la cellule. Ils assurent également la stabilité mécanique et constituent les voies de circulation des échanges intracellulaires. La structure de base de l'actine est une double hélice, sa polymérisation/dépolymérisation intervient dans la motilité cellulaire. Les microtubules sont des fibres creuses composées de dimères de tubuline assemblés. En fonction du nombre de protofilaments (typiquement de 13 à 15) ; les microtubules adoptent des réseaux cristallins d'hélicité différente.

En dépit de fonctions biologiques et d'architectures très différentes, tous ces polyméres ont été décrits en première approximation comme des fils élastiques infiniment fins, homogènes le long de leur contour ce qui suppose à tout le moins un moyennage. La description mécanique ne fait alors intervenir qu'un petit nombre de "constantes des matériaux" comme le module de courbure et de torsion. Dans le cas le plus simple on ne considère que le module de courbure. Ceci est la base de l'Hamiltonien du modèle WLC. À petite échelle, la molécule est essentiellement rigide alors qu'aux (très) grandes échelles, elle se met en pelote sous l'action du bruit thermique. Pour caractériser la flexibilité on introduit souvent la longueur de persistance qui caractérise le déclin de la corrélation angulaire le long du filament, où l'on admet une décroissance exponentielle de la corrélation. Pour l'ADN double brin, par exemple, un filament de plusieurs dizaines de microns paraît complètement flexible. Bien que la longueur de persistance soit définie simplement sa détermination directe par analyse d'image reste délicate. Il est largement accepté que l'ADN double brin peut être décrit efficacement en tant que WLC, avec aussi un module de torsion, aux tensions et torsions raisonnables, pour la statique comme pour la dynamique. Cela n'est cependant pas trivial car l'ADN "double brin" présente de petites boucles de dénaturation où sa structure est localement fondue.

Généralement cela conduit simplement à la longueur de persistance couramment admise comme moyenne. Récemment il a été avancé que ces boucles dénaturées seraient impliquées dans les coudes observés dans l'ADN double brin fixé au mica par des cations multivalents. Nous devons garder à l'esprit que tous ces filaments possèdent une structure interne au-delà de WLC qui peut se manifester de façon inattendue.

Parmi les biopolymères de la cellule, les MTs sont les plus rigides : ce sont les "poutres du vivant". Leur longueur de persistance est de l'ordre de quelques millimètres. À l'échelle de la cellule, quelques microns, ceci est une valeur très élevée. Les MT sont donc essentiellement droits dans la cellule. La mesure précise de leur longueur de persistance, sensée être une constante, a fait l'objet de beaucoup d'études. Alors que déterminée à partir des fluctuations thermiques d'un filament [1] elle est effectivement une constante, une rigidité dépendant de la longueur a été mesurée sur des MTs collés par une extrémité [2, 3]. Cette dépendance ne s'explique pas dans le cadre du WLC et implique à tout le moins des degrés de liberté interne. En plus de ces propriétés élastiques inattendues, des MTs de forme super-hélicoïdale ont été rapportés [4] qui présentent certaines analogies avec la forme des flagelles. Un modèle récent est basé sur la bi stabilité du dimère de tubuline [5] comme degré de liberté interne. Entre autres ce modèle prédit que les MTs sont polymorphes et qu'ils présentent des changements de

forme. Au début de cette thèse une observation directe du changement de forme qui viendrait étayer la théorie faisait défaut.

Dans **le Chapitre 2**, nous étudions la relaxation d'une chaîne semi-flexible (WLC) confinée, cette relaxation est anisotrope. Pour distinguer entre les quantités longitudinales et transverses nous considérons des frictions par unité de longueur différentes dans la théorie analytique. Au moyen d'arguments d'échelle et de calculs de réponse linéaire, nous établissons une succession de régimes dynamiques caractérisés par une série d'exposants. Ces régimes sont corroborés par des simulations de type Langevin à 2d. Il avait été compris précédemment que la propagation de la tension le long du filament joue un rôle important dans la dynamique aux temps courts pour un filament inextensible. Pour une chaîne fortement confinée dans un tube, le régime "libre" observé aux temps courts s'arrête quand les fluctuations transverses sont confinées pour donner place à un régime intermédiaire caractéristique de la reptation : le filament est enchevêtré avec le potentiel de confinement. Le régimes libre et enchevêtré sont obtenus analytiquement ainsi que leur fonction de crossover, les exposants sont aussi obtenus par des arguments d'échelle. L'analyse du mouvement était à l'origine motivée par des simulations de filaments WLC confinés dans des réseaux d'obstacles assez réguliers. Les résultats de la simulation sont interprétés par la théorie avec l'amplitude des fluctuations transverses mesurées à saturation comme seul ingrédient. En l'absence de paramètre ajustable, l'accord est aussi bon que l'on est en droit d'espérer. Nous étudions aussi la relaxation du filament WLC greffé, libre de tourner autour du point d'ancrage, en absence et présence d'obstacle. Nous nous concentrons essentiellement sur la décorrélation de l'orientation globale du filament et d'une portion terminale de longueur variable. Cette dernière étude est directement motivée par l'étude expérimentale d'un ADN "épinglé" sous une vésicule par des couples biotine/streptavidine présentée ci-dessous.

Dans **le Chapitre 3**, nous effectuons l'analyse d'images d'ADN. L'expérience a été réalisée à l'ICS, dans le groupe de Carlos Marques. L'idée est de mimer in vitro un évènement d'adhésion cellulaire entre une vésicule synthétique et un substrat au moyens de liaisons spécifiques biotine/streptavidine. Le substrat porte des ADN greffés qui sont balayés par la vésicule en cours d'étalement, étirés sous la vésicule et bloqués latéralement par les paires biotine/streptavidine formées. Une analyse d'image détaillée nous permet d'accéder à la répartition de masse le long du contour apparent de l'ADN et, en principe à sa tension locale. L'interprétation des résultats montre une accumulation locale de matière en certains points du contour apparent compatible avec l'existence de portion d'ADN qui n'ont pas eu le temps de relaxer durant le balayage par le front de la vésicule. Nous attribuons cela à l'existence d'un temps de relaxation

topologique plus long que le temps de Zimm. Des ADN avec des conformations de départ différentes se débobinent plus ou moins facilement ce qui se traduit par des frictions internes différentes et des tensions différentes toutes choses égales par ailleurs. L'expérience qui n'était pas destinée à cet usage invite à imaginer des dispositifs autorisant une étude systématique des temps topologiques.

Dans **le Chapitre 4**, nous nous intéressons aux filaments du cytosquelette, plus spécifiquement les propriétés statiques et dynamiques des MTs sont étudiées par analyse d'image. Nous imageons des MT fluorescents en lame mince où les filaments sont quasi aplatis. D'abord nous établissons la statistique de la super-hélicité en estimant le pas de l'hélice (sa période à 2d) et son rayon. Par une analyse d'image quantitative les fluctuations thermiques des MTs sont caractérisées par la longueur de persistance effective qui est en bon accord avec les résultats connus. Parce que nous procédons avec un seul filament nous avons accès à des oscillations de la longueur de persistance effective précédemment très atténuées par une moyenne portant sur des MTs de réseau cristallin différent. Nous présentons divers type de changement de forme de MTs et montrons que ces mouvements sont hautement coopératifs et fortement corrélés le long du filament dans son entier. Bien que ces résultats soient largement compatibles avec la théorie du MT polymorphe développée précédemment nous évitons ici de les sur-interpréter et préférons les considérer pour eux-mêmes afin qu'ils soient également confrontés à d'autres théories (non encore disponibles).

Dans **le Chapitre 5**, nous considérons des filaments hélicoïdaux a priori, décrits par un modèle de WLC augmenté que nous appelons Helical WLC et qui comprend un module de torsion et de courbure ainsi qu'une torsion et une courbure préférées. À 3d l'état fondamental de ce modèle est une hélice qui satisfait la torsion et la courbure préférées partout. Lorsque ce modèle est confiné à 2d, il autorise une diversité de formes allant de sinueuses à circulaires.

De façon similaire des formes sinueuses, spirales ou circulaires sont souvent observées dans la nature. Pour les flagelles, on trouve des formes circulaires et la "coexistence" de formes sinueuses et enroulées le long du flagelle [6]. Nous désignons les formes particulières réalisées par le HWLC par le mot "squeelix". Une propriété remarquable des squeelix est l'alternance de régions de courbure presque uniforme de sens opposés, séparées par d'étroites régions qui concentrent la torsion les "twist-kink". Par analogie avec la physique des solitons nous considérons les twist kinks comme des quasi-particules et discutons la forme du filament et ses fluctuations en termes d'injection, de diffusion et d'interactions de twist-kinks. Le paramètre de contrôle γ, une combinaison sans dimension des quatre paramètres intrinsèques du modèle, gouverne l'énergie

d'injection : pour $\gamma > 1$, les twist-kinks sont thermiquement activés; dans le ces contraire, le système accepte une densité finie de twist-kinks limitée par leur interaction. Nous montrons par simulation Monte Carlo en utilisant la méthode de la densité d'état (Wang-Landau), que le filament confiné présente des transitions entre des états discrets, caractérisés par leur densité de twist-kinks, dont certains favorisent la cyclisation tandis que d'autres sont hyper-flexibles. Le modèle de squeelix s'est révélé utile dans l'étude des MTs quasi-2d présentée dans le chapitre 4. L'idée générale de ce chapitre et de commencer à chercher une signature de la super-hélicité qui puisse clairement émerger des fluctuations thermiques.

Contents

Chapter 1

Introduction

Polymers are large molecules with a mass of at least several kiloDalton built from one or few chemically well defined small (typically of the order of 10^2 Dalton) repeat units [7]. Relevant characteristics of polymers are their molecular weight/weight-distribution, shape (linear or branched), and chemical sequence in case of polymers comprising several monomers, so-called copolymers. In traditional polymers, monomers are covalently bound and a given polymer keeps its integrity over time, unless chemical bonds are broken. If all polymers in a system are identical, the system is called monodisperse, and monodipersity can only be approached in conventional synthesis. Recently, a lot of attention was paid to non-covalent polymers, in which the elementary bricks are reversibly assembled by Hydrogen bonds or ligand-receptor pairs, for example. This is the topic of supramolecular chemistry [8, 9]. Assembled polymers are usually polydisperse, and polymer identity is usually lost over time. They have the ability to self-repair errors occurring during synthesis.

Nature actually uses both ways of polymerization and depolymerization with an amazing efficiency. Biopolymers, like proteins, are covalent polymers produced identical to each other in both sequence and length through a template based synthesis. Examples of proteins appearing in this thesis are tubulins, G-actin, and single stranded DNA produced by monodisperse molecules. Biofilaments are assembled from small units, usually proteins, without many errors or impurities which is quite remarkable as given the numerous species present *in vivo*. Nature uses the reversibility of biofilaments to polymerize/depolymerize structures as needed. Even the well-known double stranded helical DNA presents denaturation loops under physiological conditions and the local denaturation is essential to its function, during transcription for example.

Self-assembly, in a sense, has also its weaknesses, for example abnormal sequences in DNA can cause a decease linked to local mis-folding into a triple helix. It is sometimes helpful to consider biofilaments themselves as composed of intermediate assembled subunits [10, 11]. This is clear for microtubules composed of a variable 13-15 number of protofilaments, which can also exist in an isolated state. On the other side, biofilaments like actin or intermediate filaments can assemble in thicker bundles and also form gels. Polymerization/depolymerization kinetics of assembled biofilaments specially actin and microtubules plays an important role *in vivo* and is the focus of intense work. In this thesis, we will not address these important questions at all and rather consider filaments stabilized again depolymerization *in vitro* by added chemicals like taxol (for microtubules) or phalloidine (for actin). This is the case in the last chapter where conformations of microtubules are analyzed from experimental data. There are numerous indications that some of conclusions reached for stabilized filaments also hold true *in vivo*.

DNA and RNA as well-known biopolymers have a well-defined structure under physiological conditions. DNA consists of a sequence of base pairs or nucleotides that are stacked in a helical manner. These are connected to one another with two sugar-phosphate backbones. Another representative biopolymers are cytoskeleton filaments, the actin-, intermediate-filament, and microtubules. They are involved to determine the shape and motility of cells and also provide mechanical stability and tracks for intracellular transport. The basic structure of actin-filament is a left-handed helix with 6 nm in diameter and helical repeat of period 36 nm [10, 12]. The microtubules have hollow cylindrical structure formed by several protofilaments assembled from tubulin dimers. Depending on the number of associated protofilaments (typically ranging from 13 to 15), the microtubules can adopt lattice types with different helicities (See Fig. 1.3). These filaments also involves in cell motility by spontaneous polymerization/depolymerization dynamics arising at one end of MTs (both ends for actin).

The different structures has different mechanical properties, which is often characterized by the bending and torsional modulus,

$$\begin{aligned} B &= l_p k_{\mathrm{B}} T \quad (\mathrm{bending}) \\ C &= l_t k_{\mathrm{B}} T \quad (\mathrm{torsional}), \end{aligned}$$

where l_p and l_t are called persistence length to bending and twist, respectively, and k_{B} is the Boltzmann constant and T is the temperature. DNA is mechanically stable by forming double-helix structure, the bending modulus is $B/k_{\mathrm{B}}T = 50\,\mathrm{nm}$ [13], but the torsional modulus ranges

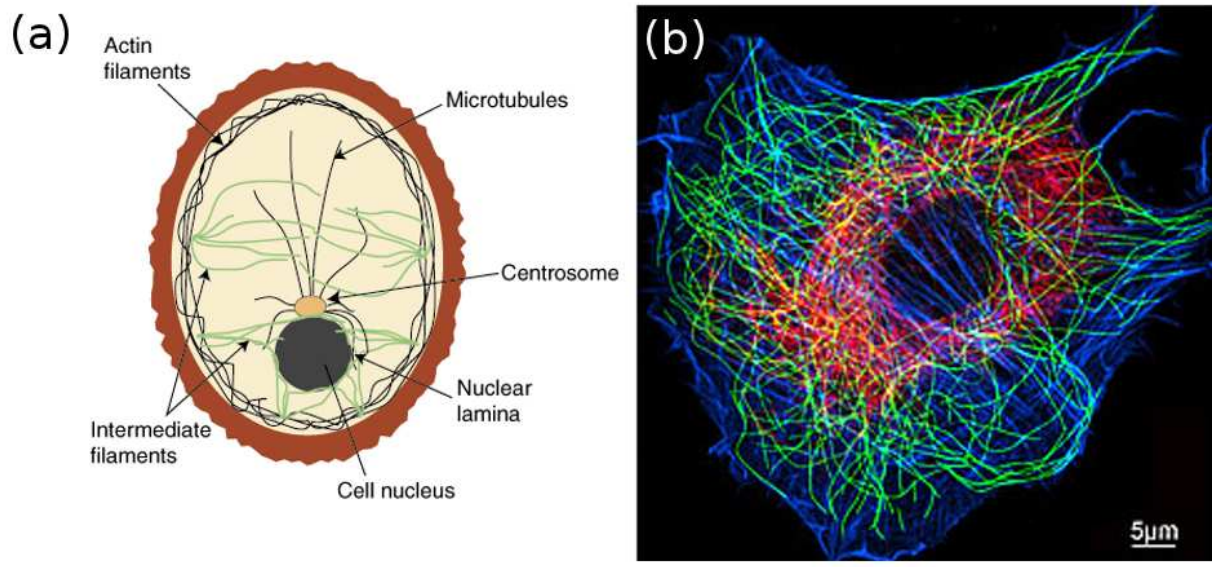

Figure 1.1: (a) Schematic illustration of the organization of cytoskeleton filaments within a cell [18]. (b) Actin- and intermediate-filament are stained blue and red, respectively, and MTs in green [19].

as $C/k_{\mathrm{B}}T = 80 \sim 110$ nm by different approaches [14–16]. On the other hand, the cytoskeleton filaments are dynamically unstable in their structure, therefore the modulus is measured from chemically stabilized filaments. Under physiological conditions, $B/k_{\mathrm{B}}T$ has been experimentally measured for intermediate filaments ($1 \sim 2\,\mu$m) [17], F-actin ($17\,\mu$m) and microtubules (5.2 mm) [1].

Understanding of the mechanics and dynamics of biofilaments has been in focus for last few decades under various conceptual considerations [20–25]. Confinement is one of essential and natural designs to study those properties. Also, it provides better insight into biological process, for example, DNA packaging in viruses [26], DNA segregation in bacteria [27], and protein exiting ribosome through a narrow cylindrical pore [28]. In the case of cytoskeleton filaments, concerning their typical contour lengths of order of few tenth of microns compared to the typical cell size of few microns, they are not only confined in a soft geometrical space but also effectively entangled with each other by forming a network [29, 30] (See Fig. 1.1 for schematic description). In this environment, the filaments often exhibit a peculiar shape of highly curved [31–33], circled shape [34–38], and self-assembled bundles [39–42] (not exactly

due to the confinement though), which certainly could be a good hint for understanding the bulk properties of a single filament. Based on the theoretical studies, many efforts of *in vitro* experiments to mimic the confinement relevant biological process has been intensively made so far.

In experiments, several types of geometrical confinements are modelled as tubelike [43–45], 2D plane [46], nanoslit [47], and a nano-and biaxial-channel [48,49]. Polymer melts or solutions also generate an effective confinement to a wiggled tube which is created by surrounding polymers [21, 50–52]. In particular, 2D confinement is conceptually appealing, but experimentally difficult to realize. Practical examples of polymers confined in 2D are polymers adsorbed to surfaces [46], and polymers constrained under the bilayer of a membrane [53]. In these systems, the polymers are not completely confined but they are considered as quasi-two-dimensional. Confinement is often an experimental necessity, in microscopy all segments need to be nearly in focal plane to be seen and traced. For instance, the DNA molecules in bulk form random coils. When brought into the 2D surface, the coiled DNA is unfolded over the surface. Technically it becomes convenient to monitor the motion of whole segments within the allowed optical resolution.

Theoretical modelling for biofilaments often considers that microscopic interactions arising from a subcomponent of structure are averaged or smoothed away. From the mechanical point of view, therefore, all biofilaments have been tentatively described as a homogeneous slender elastic rod. The description then involves some material constants like B and C. In the simplest case, bending modulus is solely considered. This is the basis of the Worm-like chain (WLC) model (Krathy and Porod [54], 1949) Hamiltonian. At short length scale, the chain is essentially stiff while at large distances thermal fluctuations eventually cause it to coil. An often introduced parameter to characterize differences is the persistence length $l_p = B/k_{\mathrm{B}}T$. Over the distance l_p, the orientation de-correlates along the curvilinear distance over filament, where an exponential decay of the correlation is anticipated for a local flexibility mechanism provided that there is no an extra correlation between sections far apart along the filaments. Under physiological conditions, l_p has been experimentally measured for intermediate filaments ($1 \sim 2\,\mu$m) [17], F-actin ($17\,\mu$m) and microtubules (5.2 mm) [1].

The bending rigidity is an essential ingredient for determining the conformations of biofilaments. Depending on the ratio between contour length L and l_p, the chain conformation can be categorized into three regimes: rod-like ($L \ll l_p$), semiflexible ($L \sim l_p$), and flexible ($L \gg l_p$) as illustrated in Fig. 1.2. The average size of chain is calculated by the mean square end-to-end

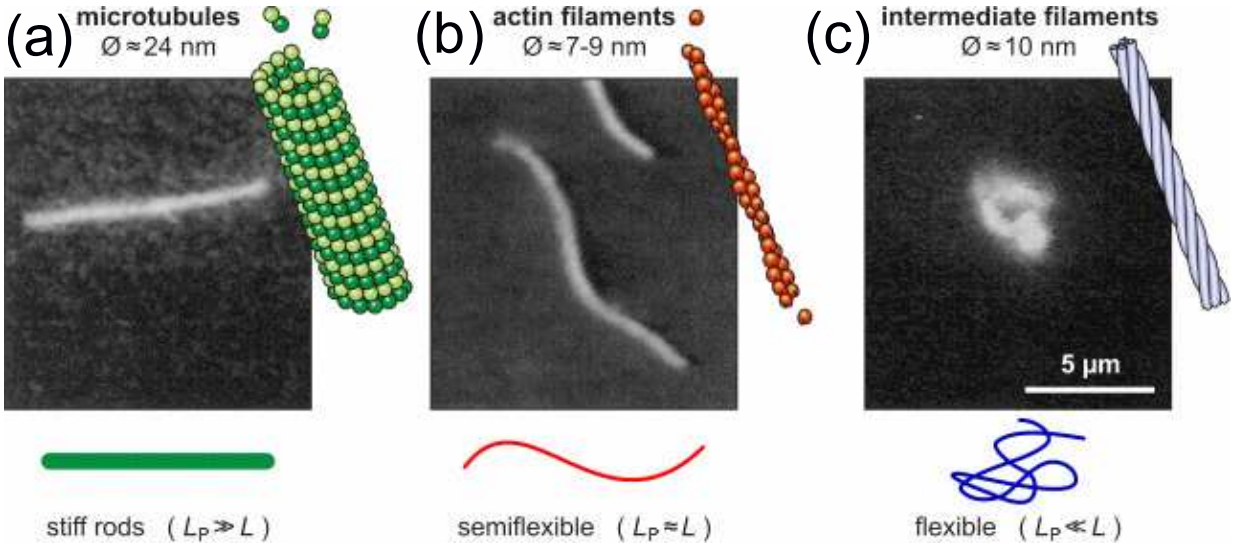

Figure 1.2: Schematic representations and fluorescence images of the three main cytoskeleton components. (a) MTs (b) Actin- (c) Intermediate-filament, three filaments are different in their stiffness l_p and the diameter $\varnothing$. [50]

distance

$$\langle R^2 \rangle = 2l_p^2 \left[L/l_p + e^{-L/l_p} - 1 \right], \tag{1.1}$$

which is also used to determine l_p. In the limit of $L/l_p \gg 1$, the flexible chain becomes random-walk conformation $\langle R^2 \rangle \approx 2l_p L$ with effective bond length $b = 2l_p$ (Kuhn length). In the opposite limit of $L/l_p \ll 1$, the chain behaves like a rod $\langle R^2 \rangle \approx L^2$.

A very long flexible polymer like DNA coil can have a number of possible internal structures. In the region where the segments are highly concentrated, the complex topological states like knots or catenanes (in the presence of enzyme regulation) are naturally emerging [55]. These states can profoundly impact the dynamics of polymer [56, 57], the magnitude of the effect depends strongly on the complexity of the knots [58]. Such complex topological states are indeed observed in the course of DNA replication and recombination [59–61]. This could also be a good example for manipulation of the physical models like ribbon apart from their biological functions. There has been theoretical hypothesis [62–66] to predict the internal structure of DNA. However, such structure is hardly distinguished in the experiment. In spite of the importance of internal structure of DNA molecules, it has never been directly put to a test due to the experimental difficulties.

On the other hand, the cytoskeleton filaments as a representative stiff polymer have a smooth contour and stretched shape. Therefore, the thermal motion can be easily traced in both *in vivo* [33] and *in vitro* [1, 4] experiment. Inspired by several experimental observations [4, 67–70], it has been suggested that the cytoskeleton filaments are adjusted into a 3D helical structure in relatively large length scales. Yet, the characterization of helical state (radius and pitch) has not been documented. For a helical structure, the twisting mode becomes appreciable as much as bending. This feature calls for an adaptation/augmentation of the classical WLC model, which should give rise to qualitatively different features in mechanics and dynamics of cytoskeleton filaments.

In many experiments, the cytoskeleton filaments display distinctive thermal motion [1,4,71], which is characterized quantitatively by the l_p-measurement [1–3, 17]. The order of magnitude of measured l_p agrees between experiments for all filaments, but for the MTs and intermediate filaments, the length-dependent stiffness is observed [2, 3, 17]. This is unprecedented feature because it does not fit with standard WLC model where l_p is given by a constant. Provisional understanding of the length dependency of l_p is attempted based on their highly complicated structure. In terms of structural organization and mechanical properties, it was assumed that the occurrence of axial slipping or shearing between dimers within protofilaments result in the length-dependent stiffness [2,17]. Recently, there was a numerical study arguing that the length dependency of l_p may be a general feature for biofilaments [72]. Therefore, it is still in debate whether l_p is varying with length or not.

Besides the anomalous mechanics, the cytoskeleton filaments keep changing their shapes, which is called polymorphism. This might be in analogy to the bacterial flagella filament, which has a well-known helical structure [74] as shown in Fig. 1.4, plus undergoing conformational transformations by changing the environmental conditions [75, 76]. This feature also might be attributed to the sophisticated structures, but it has not been elucidated. In this sense, it definitely seems necessary to grasp on the inherent structure and mechanisms in a comprehensive manner.

This thesis is devoted to the mechanics and dynamics of bio-filaments and -polymers in the framework of WLC model. By working out several confined properties of the WLC, we will also illustrate some shortcomings and present more advanced models. Throughout this work, filaments are often considered in confined geometries, e.g. vicinity of a focal observation plane, thin slabs, and paths defined by obstacles, all of which help revealing their dynamics and mechanical properties.

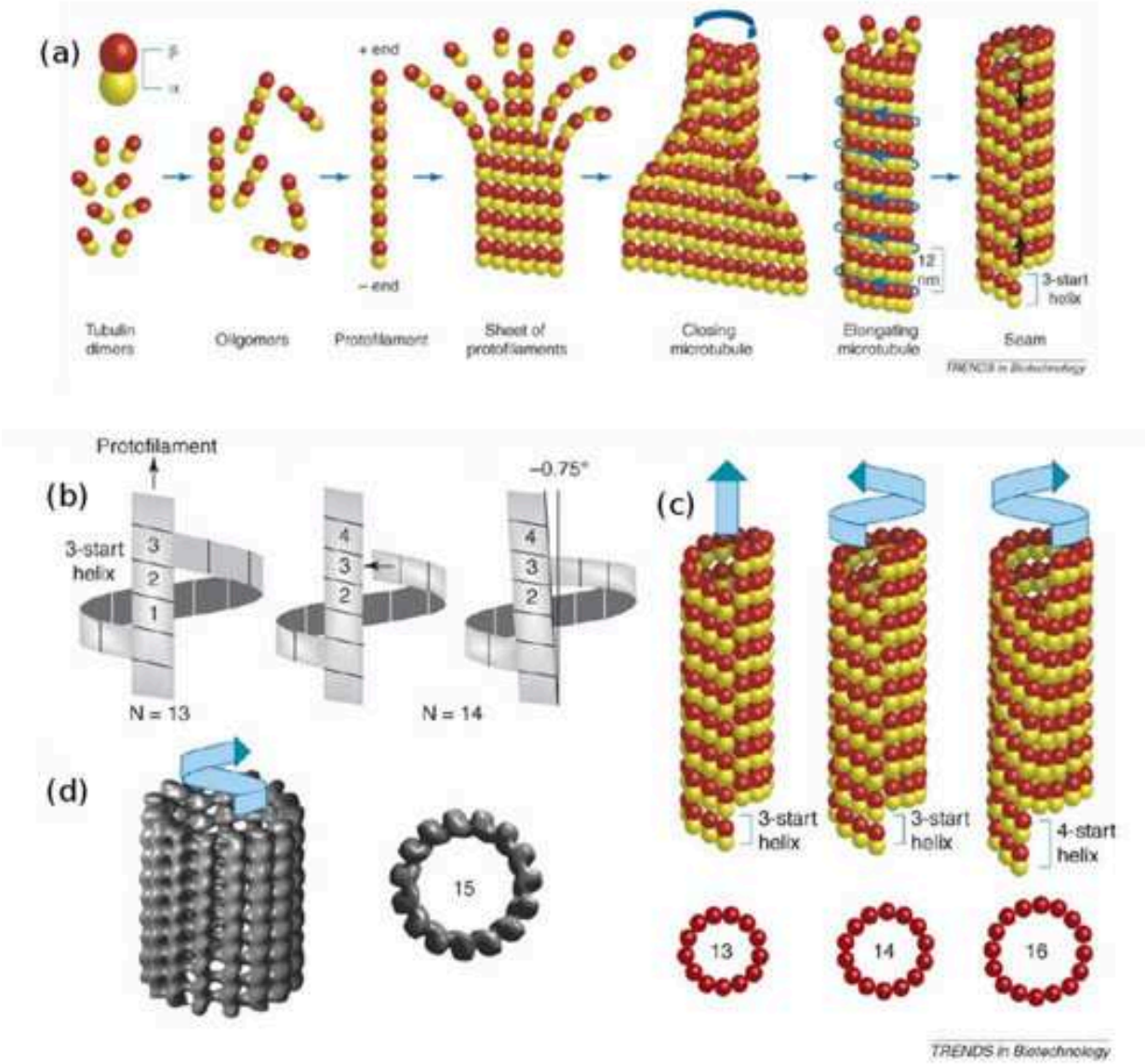

Figure 1.3: (a) Schematic description on self-assembly of MTs. α- and β- tubulin dimers assemble into straight protofilament in alternative manner. The PFs start to interact laterally forming a sheet with characteristic intrinsic inward curvature, and the sheet closes into a tube forming a microtubules. (b) Depending on the number of PFs, MTs has different helical surface lattices, (c) 14- and 16-PFs MTs are left- and right-handed lattice, respectively. (d) Isosurface rendering of the electron density of a 15-PFs MTs are shown to have right-handed helical lattice [73].

In **Chapter 2**, we focus on the relaxation dynamics of a confined stiff filament modelled by the WLC. The construction of the dynamics of the WLC is anisotropic. To keep track of transverse and longitudinal quantities, we consider different frictions per unit length in both directions, at least in analytics. By means of the scaling analysis and explicit calculation in linear response theory, we suggest that the motion is characterized by different exponents corresponding to each dynamic regime. The results are corroborated by 2-d Langevin simulations. It was recognized earlier that tension propagation plays a role in the early dynamics due to the total contour length constraint [77]. For a chain strongly confined in a tube, the early free regime ends when the lateral fluctuations experience confinement, which gives rise to an intermediate dynamic regime illustrative for reptational motion: the filament is entangled with the confining potential. The free regime and the entangled regime are calculated analytically with their crossover function, the kinetic exponents are also predicted by a scaling analysis. The analysis of the motion was primarily motivated by the numerical study of a WLC in an array of obstacles. The findings for the longitudinal short time dynamics are fitted against the theory with the measured transverse fluctuation at saturation as the only input. The agreement between the measured and predicted prefactors is as good as it can reasonably be. In addition, the relaxation of a grafted semiflexible polymer is studied both in absence and presence of the obstacles. The main focus is on the orientational relaxation of the whole chain and of some end-section by measuring auto-correlation functions. The latter study is directly motivated by the DNA pinned under a vesicle experiment described next.

In **Chapter 3**, we analyze the images of DNA molecules obtained from fluorescence microscopy. The experiment was carried out by Carlos Marques group at ICS [53]. This experiment is motivated to mimic a cell adhesion event in vitro between a vesicle and a substrate on which the DNA molecules are end-grafted. When a vesicle spreads over the substrate, a grafted DNA molecule is stretched under vesicle and confined by biotin-straptividin chemical bonds under the vesicle. Careful image analysis allows us to access the internal structure of the DNA molecules. Applying the standard WLC model, we reveal an implication of internal friction of the DNA, which varies from chain to chain. As one possible source of internal dissipation, self-entanglement effects along the DNA contour are discussed. During unraveling of a given coil, friction depends on the internal state ("topology"). We present a scaling argument, based on the so-called gate model, to estimate the relaxation time for a self-entangled chain and find it (much) longer than the Zimm relaxation time. This results in the occurrence of spots concentrated in DNA under the vesicles attributed to sections not relaxed under the current

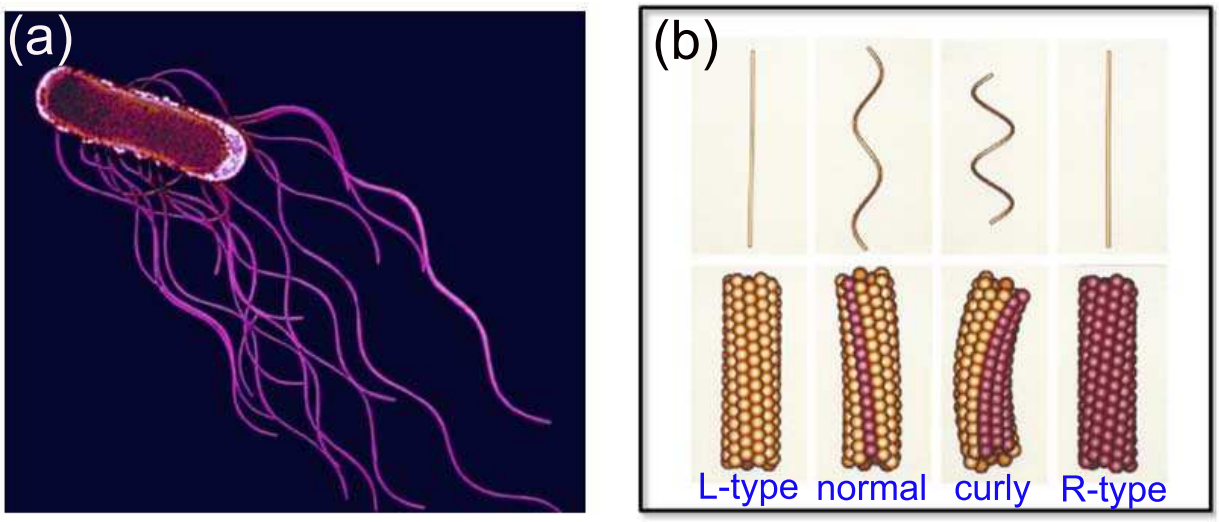

Figure 1.4: Salmonella bacterial flagella (a) Swimming bacteria utilizes their helical flagella for propulsion. (b) Polymorphic model of the filament. The model is based on the one by Calladine (1978). The top panel shows morphology of the filaments and the bottom panel shows the subunit arrangements within a short segment. The filaments are named from left to right: L-type straight, normal, curly and R-type straight. The two subunit colours represent the two distinct states of flagellin. The supercoil in normal is left-handed and in curly is right-handed [74].

spreading velocity. The setup, not designed for this purpose, invites to try and measure the topological relaxation time in dedicated experiments.

In **Chapter 4**, we turn to the cytoskeletal filaments, in particular, the dynamical and mechanical properties of microtubules investigated through the image analysis. The images are taken from the fluorescent MTs thermally fluctuating in the confined slab geometry, where the MTs are almost flattened by the confinement. First, we establish statistics of the MTs helicity by estimating helical pitch (measured as wavelength in 2-d) and radius. By implementing quantitative image analysis, the thermal fluctuations of MTs are characterized by measuring the effective persistence length, which is in good agreement with the previous experiments [2, 3]. As we proceed with one and the same filament while previous experiments averaged over many filaments with likely different lattice helicity, we reveal the predicted fine structure of the persistence length vs. length curve which is otherwise to some extend washed out. We will present several types of conformational changes in MTs shape, and show that the motion is highly cooperative and strongly correlated over the whole MTs contour. Although our findings do not

conflict with the theoretical model developed earlier, we would like our data to be considered *per se* and confronted with other possible theories (yet to come).

Chapter 5 will consider *a priori* helical filament described by the augmented WLC model which we call Helical WLC (HWLC) comprising a twist and bending modulus. In three dimension, the ground state of the model is indeed helical satisfying the preferred twist and curvature everywhere. When confined in two dimensions, the model exhibits a variety of shapes from wavy to circular. Similar shapes such as looped waves, spirals, or circles are often found in nature, for flagella, circular and coexisting of wavy and coiled shape are found [6]. The peculiar shapes obtained from our model are coined the name "squeelix". A remarkable feature of the squeelix is the occurrence of regions of flipped almost uniform curvature separated by "narrow" regions where the twist is concentrated: the twist kinks. In analogy to soliton physics, we introduce the twist kinks as quasi-particles and discuss the filament shape and its fluctuations in terms of twist kink injection, twist kink interaction and twist kink diffusion. The control parameter γ, a dimensionless combination of the four intrinsic model parameters, two elastic ones, two geometrical ones (B, C and intrinsic bending and twist curvature ω_1, ω_3), governs the injection energy: if $\gamma > 0$, twist kinks can only be thermally activated in the reversed case the system accepts a finite twist kink density limited by their mutual interaction. By means of Monte-Carlo simulation using the density of states method, we show that the confined filaments can thermally switch between discrete twist-induced conformational states, with some of them exhibiting enhanced circularization probability while others display hyper-flexibility. The general idea of this chapter is to start setting standards that provide fingerprints for filament super-helicity, which may otherwise remain elusive.

Chapter 2

Dynamics of a confined semiflexible polymer in narrow pores [1]

In this chapter, we study the motion of a single semiflexible filament confined in narrow pores with a diameter less than its persistence length. This gives an opportunity to review dynamics and mechanical properties of a semiflexible chain. By means of scaling arguments and two-dimensional Langevin simulations, we show that the stiff chain kinetics follows the reptation picture, albeit with kinetic exponents (for the central monomer) different from those for flexible chain reptation. For most stages of the dynamics, asymptotic power laws from scaling is complemented by prefactors obtained analytically. These are calculated for an infinite chain confined by a harmonic potential: the transverse and longitudinal dynamics of the chain are explicitly investigated in the linear response regime.

2.1 A brief review on reptation dynamics of a flexible chain

The dynamics of dense solution of long linear polymers is successfully described by the celebrated reptation picture first proposed for a chain in an array of fixed obstacles [21,78,79]. A segment of a long flexible polymer in a melt or dense solution experiences confinement to an effective tube due to topological interactions. The tube diameter a, typically a few nanometers, is larger than

[1] This chapter presents results published in J. Chem. Phys. **103** 044908 (2010) and Eur. Phys. J. E **32** 119 (2010), respectively.

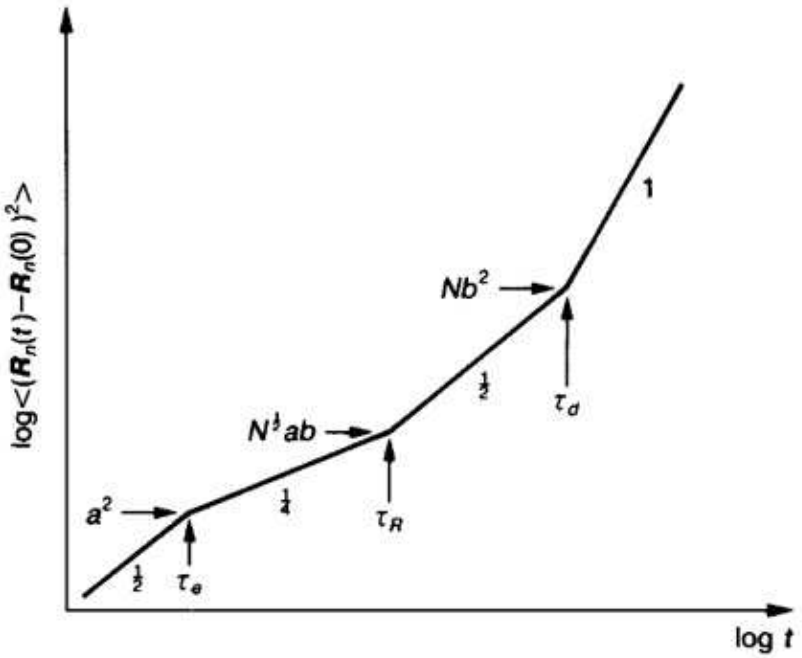

Figure 2.1: Mean square displacement (MSD) of a central monomer $g_1(t) = \langle(\mathbf{R}_n(t) - \mathbf{R}_n(0))^2\rangle$ for the reptational motion of a flexible chain is plotted logarithmically as a function of time [78]. The MSD shows four different dynamic regimes (See the text for a brief explanation).

the monomer size b, typically $1/10$ of a nanometer, but much smaller than the polymer coil size of order hundred nanometers. The reptational motion of flexible chains is often characterized by the mean square displacement (MSD) of the central monomer $g_1(t)$ (termed $\phi_n(t)$ in Ref. [78]), which shows four different kinetic exponents corresponding to different dynamic regimes as shown in Fig. 2.1. These exponents are confirmed by several numerical studies [80–82]. At short times the monomers are governed by free Rouse dynamics $g_1(t) \propto t^{1/2}$. After the so-called entanglement time τ_e, the monomers are confined by surrounding chains. The segmental Rouse motion takes place along the Random-Walk (RW)-type tube, projection to the geometrical space thus leads to $g_1(t) \propto t^{1/4}$. At Rouse time τ_R, the internal degrees of freedom are relaxed but the chain still experiences tube confinement. The central monomer shows Fickian diffusion along the RW-type tube, one hence finds $g_1(t) \propto t^{1/2}$. After the reptation time τ_d, the chain has left the initial tube and Fickian diffusion is observed $g_1(t) \propto t^1$. Taking into account tube length

fluctuations [78, 79], the reptation time for flexible chains of length S is $\tau_d \sim S^3(1 - a/\sqrt{Sb})$ this can be translated in an effective (depending on S) exponent larger than 3. A more detailed description of the reptation dynamics can be found in Ref [78].

2.2 Application of reptation picture to a stiff chain

Recently, numerical studies by several authors show that the reptation picture applies to stiff chains in very entangled solution [83–87]. The chain rigidity is described by the persistence length l_p, which is the decay length of the tangent vector correlations. Morse and other authors reported that in highly entangled solution, the middle monomer's mean square fluctuation develops a "plateau" as an indication of reptational motion along the tube defined by surrounding other chains [84]. Reptation dynamics is also observed numerically for semiflexible polymers diffusing through porous media [88].

In this chapter, we study the motion of a single semiflexible non extensible chain diffusing through porous media. We present results from computer simulations and propose a scaling analysis extending previous results on free filaments [89] to the case of confined filaments. For a free *flexible* chain, the motion of the central monomer is sub-diffusive until it is correlated along the whole chain and Fickian diffusion sets in. On the other hand, due to the anisotropic nature of fluctuations, the free dynamics of a *semiflexible* chain is much richer. It has been shown numerically and by scaling arguments [89] that transverse and longitudinal displacements do initially grow with different powers of time. The anisotropy in the friction per unit length (similar to the one for a rigid rod [78]) has less impact. We will nonetheless distinguish between transverse $\zeta_\perp$ and longitudinal $\zeta_\parallel$ friction per unit length in the formulas for technical reasons and some of results apply in three-dimension where $\zeta_\perp \simeq 2\zeta_\parallel$ (in free space). In our two-dimensional(2-d) Brownian Dynamics simulation $\zeta_\perp$ and $\zeta_\parallel$ are taken to be identical [90]. If we have in mind chains on a solid substrate with no-slip boundary condition for hydrodynamics, this is reasonable [91].

2.3 Scaling theory

We use the continuous Worm-like Chain (WLC) model which successfully describes a number of synthetic polymers as well as DNA [92]. It is ruled by the bending Hamiltonian $H = \frac{1}{2}k_{\mathrm{B}}Tl_p\int_0^S\left(\frac{\partial^2\mathbf{r}(s)}{\partial s^2}\right)^2 ds$ where the persistence length l_p is linked to the bending modulus $l_pk_{\mathrm{B}}T$ and s is the arclength parameter ranging from 0 to the chain contour length S. For the stiff chain fragments or strongly confined weakly fluctuating chains we considered here, the Monge representation is generally used where only transverse fluctuations around the straight shape are taken into account.

$$H_0/k_{\mathrm{B}}T = \frac{1}{2}l_p\int_0^S\left(\frac{d^2\mathbf{r}_\perp}{ds^2}\right)^2 ds. \tag{2.1}$$

The simplified Hamiltonian (Eq. 2.1) allows to access the transverse fluctuations of a free chain accurately. Balancing the frictional force with the bending force $-\frac{\partial H_0}{\partial r_\perp}$ and random force$f_\perp$ leads to the Langevin equation for transverse fluctuations:

$$\zeta_\perp\frac{\partial r_\perp}{\partial t} = -l_pk_{\mathrm{B}}T\frac{\partial^4 r_\perp}{\partial s^4} + f_\perp \tag{2.2}$$

In this work, the thermal energy is taken as unit $k_{\mathrm{B}}T = 1$.

2.3.1 Equilibrium fluctuations

We present a scaling analysis for a semiflexible chain confined by a harmonic potential. For a free chain equilibrium fluctuations are dominated by the smallest wave vector of order $1/S$. As a result, fluctuations per unit chain length are given as $\langle\delta r_\perp^2\rangle/S = S^2/l_p$ and $\langle\delta r_\parallel^2\rangle/S = S^3/l_p^2$ [93]. The very same quantities can be obtained for chains in a slit of width h. The correlation length l_1 in a slit has been first derived by Odijk [24] as $l_1 = (h^2l_p)^{1/3}$. The length l_1 can be thought of as the typical distance along the chain between contacts with the slit walls, where the chain is deflected by the slit boundaries. The scaling argument hence states that the bending energy of an arc of length l_1 spanning the slit laterally is comparable to the thermal energy. As a consequence, l_1 also gives the confinement energy $F = S/l_1$. The longest wavelength is now $\sim l_1$ rather than $\sim S$ hence $\langle\delta r_\perp^2\rangle = l_1^3/l_p \sim h^2$ and $\langle\delta r_\parallel^2\rangle/S = l_1^3/l_p^2$. The longest wavelength l_1 along the contour has a longitudinal extension $l_1(1-h^2/l_1^2) = l_1(1-l_1/l_p)$ and the longitudinal chain extension is thus $L = S(1-l_1/l_p)$. These results suppose strong confinement $h < l_p$ to ensure weak fluctuations. We may apply these results to estimate the

correction to the disentanglement time τ_d due to end-to-end length fluctuations. The time τ_d for a chain to diffuse out of its tube can be measured as the decay time of the chain end-to-end vector correlation. The shortest tube length L_{short} within typical thermal fluctuations is $L_{short} \approx L - \sqrt{\langle \delta r_\parallel^2 \rangle}$. Accordingly, we estimate $\tau_d = L_{short}^2 S \zeta_\parallel$ to be

$$\tau_d = \zeta_\parallel S^3 \left(1 - \frac{l_1^{3/2}}{S^{1/2} l_p} \right). \tag{2.3}$$

Here we approximate the average longitudinal chain extension as $L \approx S$ neglecting small correction l_1/l_p. Writing $\tau_d \sim S^{\nu_d}$, we obtain the effective (chain length dependent) exponent ν_d from the logarithmic derivative, $\nu_d = \mathrm{d}\log\tau_d/\mathrm{d}\log S$.

$$\nu_d = 3 + \mathrm{const.}\frac{h}{(l_p S)^{1/2}} \tag{2.4}$$

In the limit that $l_p \to b$, $h \to a$, the exponent recovers the estimate for a flexible chain given in Section 2.1 [78, 79].

2.3.2 Transverse dynamics

Transverse dynamics of a free chain is described easily starting from Eq. 2.2 [89, 94, 95]. The longest relaxation time for a stiff chain of length S can be read as $\tau_S = \zeta_\perp S^4/l_p$ from Eq. 2.2 . Conversely after a time t a section of size $l(t) = (t l_p/\zeta_\perp)^{1/4}$ relaxes. Inserting the relaxed length into the transverse static fluctuation, we get $\langle \delta r_\perp^2(t) \rangle = l^3(t)/l_p = (t/(\zeta_\perp l_p^3))^{3/4} l_p^2$. For a free filament, we may write down the general form $\langle \delta r_\perp^2(t) \rangle = (t/(\zeta_\perp l_p^3))^{3/4} l_p^2 \mathcal{F}(l(t)/S)$ with an unknown scaling function $\mathcal{F}(x)$ and $\mathcal{F}(0) = 1$. The short time behaviour $\sim t^{3/4}$ should crossover to Fickian diffusion for large times, hence $\mathcal{F}(x) \sim x$ for large x.

Let us turn to the chain confined in a tube of radius $a \sim h$. Free dynamics is preserved and $\langle \delta r_\perp^2(t) \rangle \propto t^{3/4}$ for short times $l(t) < l_1$ when the central monomer freely explores the tube section. The transverse fluctuation reaches the tube diameter at the entanglement time

$$\tau_e = \zeta_\perp l_1^4/l_p, \tag{2.5}$$

and the topological constraints become relevant. For times (much) larger than τ_e, the transverse fluctuation of the central monomer saturates at the tube width $\langle \delta r_\perp^2(t) \rangle \sim h^2$. This suggests

that the amplitude of transverse fluctuation until saturation is governed by the following scaling relation with a new scaling function $\mathcal{F}_\perp(t/\tau_e)$,

$$\begin{aligned} \langle \delta r_\perp^2(t) \rangle &= h^2 \mathcal{F}_\perp(t/\tau_e) \quad \text{with } \tau_e = \zeta_\perp l_p^3 (h/l_p)^{8/3} \\ \mathcal{F}_\perp(x) &\sim x^{3/4} \quad (x \to 0), \quad \mathcal{F}_\perp(x) \sim 1 \quad (x \to \infty). \end{aligned} \tag{2.6}$$

Fickian diffusion is expected after the disentanglement time τ_d.

2.3.3 Longitudinal dynamics

Due to the coupling between longitudinal and transverse fluctuations, describing the longitudinal fluctuations is more delicate. Using the naive argument as for the transverse fluctuation leads to identify $\langle \delta r_\parallel^2(t) \rangle$ with the equilibrium fluctuation of $S/l(t)$ independent sections of size $l(t)$, hence $\langle \delta r_\parallel^2(t) \rangle = (S/l(t))(l(t)^4/l_p^2) = S\langle \delta r_\perp^2(t) \rangle / l_p$. This result independent of $\zeta_\parallel$ is in fact incorrect. The reason is that tension propagation does not allow for this motion as pointed out by Ref. [89]. Following Ref. [89], we use linear response and relate the longitudinal fluctuation $\langle \delta r_\parallel^2(t) \rangle$ to the average displacement $\langle \delta r_\parallel(t) \rangle$ under a weak external longitudinal force $f_\parallel$, $\langle \delta r_\parallel(t) \rangle = f_\parallel \langle \delta r_\parallel^2(t) \rangle$. Assuming the previous estimate of the longitudinal fluctuation, the frictional force under the resulting motion would be $f_{frict} = \zeta_\parallel S(S/l_p)\langle \delta r_\perp^2(t) \rangle f_\parallel / t$ and it should balance the external force. The authors of Ref. [89] conclude that only a chain section of length $l_2(t) = l_p \left(\frac{t}{l_p^3 \zeta_\parallel^4 \zeta_\perp^{-3}} \right)^{1/8}$ can be equilibrated after time t. Hence, the chain segment $l_2(t)$ is set into motion with velocity $v \sim f_\parallel / (\zeta_\parallel l_2(t))$ and drifts a distance $\langle \delta r_\parallel(t) \rangle = f_\parallel t / (\zeta_\parallel l_2(t))$. Applying the fluctuation dissipation theorem again leads to the final result of the longitudinal fluctuation of a free chain: $\langle \delta r_\parallel^2(t) \rangle = l_p^2 \left(\frac{t}{l_p^3 \zeta_\parallel^{4/7} \zeta_\perp^{3/7}} \right)^{7/8}$.

When a chain is confined in a tube, the transverse fluctuation saturates after time τ_e. On the other hand, the tension propagates along the filament in the time τ_σ. Depending on the ratio between τ_e and τ_σ, different kinetic regimes should be considered. In case of $\tau_\sigma < \tau_e$ that the longitudinal tension is equilibrated before the transverse fluctuation saturates, both longitudinal and transverse fluctuation grow with $\sim t^{3/4}$. This regime is satisfied for a short stiff or ill-confined filament and less relevant to our work.

Another regime is $\tau_e < \tau_\sigma$, where the transverse fluctuation is equilibrated before longitudinal tension propagates over a whole filament. For smaller times the chain behaves like a

free chain and the previous result applies as $\langle \delta r_\parallel^2(t) \rangle \sim t^{7/8}$. At larger times there is an intermediate regime $\tau_e < t < \tau_r$, where the (longitudinal) internal modes relax before the chain, now correlated over its whole length, diffuses along the one-dimensional tube. (The expression for the internal relaxation time τ_r is derived later in Eq. 2.8). The latter diffusion regime should obey $\langle \delta r_\parallel^2(t) \rangle = t/(\zeta_\parallel S)$ for $t > \tau_r$. In the intermediate regime of internal longitudinal relaxation, lateral fluctuations are relaxed. The dynamics must hence be independent of the transverse friction $\zeta_\perp$. In particular, the dynamical correlation length $l_3(t)$ should be independent of the transverse friction $\zeta_\perp$. The crossover scaling from $l_2(t)$ to $l_3(t)$ has the following form: $l_{3,2}(t) = l_2(t)\mathcal{G}(t/\tau_e)$ with $\mathcal{G}(x) = 1$ for small arguments. For large arguments, the transverse friction has to drop out from the asymptotics. Taking into account the expression of $l_2(t)$, this imposes $\mathcal{G}(x) \sim x^{3/8}$ for large arguments. The explicit asymptotics $l_3(t)$ is deduced as $l_3(t) = l_p\sqrt{\frac{t}{\zeta_\parallel l_1^3}}$. Applying linear response and fluctuation-dissipation theorem, we obtain the longitudinal MSD in this regime:

$$\langle \delta r_\parallel^2 \rangle = h^2 \sqrt{\frac{t}{\zeta_\parallel l_1^3}}. \tag{2.7}$$

This intermediate longitudinal regime smoothly crosses over to Fickian diffusion along the tube at the internal relaxation time τ_r:

$$\tau_r = \zeta_\parallel l_1^3 \left(\frac{S}{l_p}\right)^2 = \zeta_\parallel S^2 h^2 / l_p. \tag{2.8}$$

In the crossover region $t \sim \tau_r$, the chain ends are only marginally correlated and $\langle \delta L^2 \rangle \sim 2\langle \delta r_\parallel^2 \rangle$ on the other hand L should almost show equilibrium fluctuations described earlier $\sim S l_1^3/l_p^2$. Eq. 2.7 indeed satisfies $\langle \delta r_\parallel^2 \rangle \sim S l_1^3/l_p^2$ for $t \sim \tau_r$.

Formally the expressions obtained for τ_e and τ_r do not ensure that the necessary condition $\tau_r > \tau_e$ is satisfied. The physical reason is clear: we do not expect the $\sqrt{t}$ regime for a rod (in a smooth, say cylindrical, confinement) neither for a free chain. More precisely, the width of the $\sqrt{t}$ regime can be characterized by $\tau_r/\tau_e = \frac{\zeta_\parallel}{\zeta_\perp}\frac{S^2}{l_p^2}\left(\frac{l_p^2}{\langle r_\perp^2 \rangle}\right)^{1/3}$ which should be larger than unity (at the scaling level). In the simulation, the $\sqrt{t}$ regime will often be found to extend over more than one decade in time with an amplitude close to the predicted one (more precise predictions beyond scaling will be given below). This regime is not seen for the stiffest or ill-confined chains.

At the disentanglement time τ_d discussed earlier (Eq. 2.3), the diffusion becomes d-dimensional.

	$t < \tau_e$	$\tau_e < t < \tau_r$	$\tau_r < t < \tau_d$	$t > \tau_d$
$\nu_\perp$	3/4	0	0	1
$\nu_\parallel$	7/8	1/2	1	1

Table 2.1: Kinetic exponents for the mean square displacement $\langle \delta r^2_{\perp,\parallel} \rangle \propto t^{\nu_\perp,\nu_\parallel}$

Longitudinal chain fluctuations are summarized as follows.

$$\langle \delta r^2_\parallel(t) \rangle = \begin{cases} l_p^2 (\frac{t}{l_p^3 \zeta_\parallel^{4/7} \zeta_\perp^{3/7}})^{7/8} \mathcal{F}_{\parallel,1}(t/\tau_e) \quad (t < \tau_r) \\ \mathcal{F}_{\parallel,1}(x) \sim 1\,(x \to 0), \quad \mathcal{F}_{\parallel,1}(x) \sim x^{-3/8}\,(x \to \infty) \\ \\ h^2 \sqrt{\frac{t}{\zeta_\parallel l_1^3}} \mathcal{F}_{\parallel,2}(l_p \sqrt{\frac{t}{\zeta_\parallel l_1^3}}/S) \quad (\tau_r < t < \tau_d) \\ \mathcal{F}_{\parallel,2}(x) \sim 1\,(x \to 0), \quad \mathcal{F}_{\parallel,2}(x) \sim x\,(x \to \infty). \end{cases}$$

The kinetic exponents in various regimes are summarized in Table 2.1.

The motion of the central monomer in the direction perpendicular to the initial end-to-end vector measured in simulations also reflects tube undulations explored by the central monomer during its longitudinal motion. Assuming that tube wiggles reflect transverse equilibrium chain fluctuations (as is shown by the simulation results), the associated perpendicular fluctuations grow with time as $\langle \delta r^2_\perp \rangle \sim \langle \delta r^2_\parallel \rangle^{3/2}/l_p$, which exceeds h^2 at large enough times. In the regime of internal relaxation ($\tau_e < t < \tau_r$), $\langle \delta r^2_\perp \rangle = h^2 \{1 + (h/l_p) \left(t \zeta_\parallel^{-1} l_1^{-3} \right)^{3/4} \}$ where the second term, due to longitudinal diffusion along undulations, eventually dominates for somewhat larger chains ($S > l_p^2/l_1$). In the reptation regime, $\langle \delta r^2_\parallel \rangle \sim t/(\zeta_{||} S)$ leads to

$$\langle \delta r^2_\perp \rangle \sim l_p^2 \frac{t^{3/2}}{(\zeta_{||} S l_p^2)^{3/2}}. \tag{2.9}$$

After the internal (longitudinal) relaxation time τ_r, we hence expect an upturn $\sim t^{3/2}$ coming out the plateau of the transverse fluctuations.

Some results obtained for infinite chains confined by a harmonic potential [96] will be used later for a semi-quantitative fitting of the data. We present the scaling results with the numerical prefactors below. The detailed calculation will be given in Section 2.5. As in the simulation,

we put here $\zeta_\perp = \zeta_\parallel = \zeta$.

$$\begin{aligned}
\langle r_\perp^2(t)\rangle &= 2\frac{\Gamma[1/4]}{3\pi}\left(\frac{t}{\zeta l_p^3}\right)^{3/4} l_p^2 \quad (t<\tau_e)\\
\langle \delta r_\parallel^2(t)\rangle &= \frac{1}{2^{7/8}\Gamma[15/8]}\left(\frac{t}{\zeta l_p^3}\right)^{7/8} l_p^2 \quad (t<\tau_e)\\
\langle \delta r_\parallel^2(t)\rangle &= l_p^2\left(\frac{\langle r_\perp^2\rangle}{2\pi l_p^2}\right)^{1/2}\sqrt{\frac{t}{\zeta l_p^3}} \quad (\tau_e<t<\tau_r)\\
\frac{\tau_r}{\tau_e} &= \left(2\frac{\Gamma[1/4]}{3\pi}\right)^{4/3}\frac{S^2}{4l_p^2}\left(\frac{l_p^2}{\langle r_\perp^2\rangle}\right)^{1/3}
\end{aligned} \tag{2.10}$$

2.4 Simulation

2.4.1 Simulation descriptions

Confinement with obstacles

We modelled a semiflexible chain immersed in 2-d matrix containing obstacles as shown in Fig. 2.2. In practice, obstacles are repulsive to each monomer so that traveling across the obstacles is not allowed. Series of point obstacles in 2-d can substantially reduce the chain fluctuation. Furthermore, chain connectivity does not allow to circumvent obstacles. We introduce obstacles of various surface densities $c = 1/h^2$ with h being the typical distance between them. Two types of obstacle arrangements are considered: regular obstacles on a square lattice and quasi regular distributions where the positions of obstacles are perturbed (by a random displacement smaller than the lattice spacing) away from the lattice sites. The latter we term (weakly) disordered below. For the disordered obstacle densities we consider here, the aim is to suppress square lattice artifacts, like the occurrence of straight easy-diffusion paths. At any time, close obstacles define a tube for a given chain, we may assume the tube diameter to be approximately h. As the lateral diffusion is restricted, the motion of chains takes mainly place along the longitudinal direction.

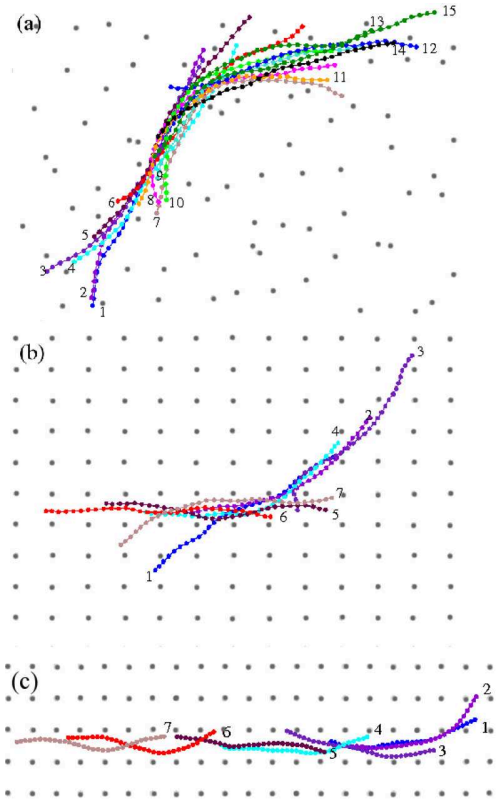

Figure 2.2: Configuration chain $S = 32b$, $l_p = 70b$ of diffusive motion with obstacles in disordered/regular distribution. The trajectories are captured at every $200\,t_0$ in disordered matrix (a) $c = 1/(5b)^2$, and at every $1000\,t_0$ in regular matrix (b) $c = 1/(5b)^2$ and (c) $c = 1/(3b)^2$. The numbers indicate snapshots in chronological order.

Langevin simulation

For a confined chain described above, we performed Langevin simulations. The Brownian force gives rise to a microscopic time scale associated with the diffusive motion of one monomer $t_0 = b^2/D$, which is used as the unit time. Langevin equation for each monomer is integrated with step size $\delta t = 2.5 \times 10^{-4} t_0$. In order to describe the movement of a monomer, we integrated the following Langevin equation:

$$\zeta \frac{d\mathbf{r}_i}{dt} = \mathbf{F}_i^{bend} + \mathbf{F}_i^{link} - \nabla U_i^{LJ} + \mathbf{f}_i, \tag{2.11}$$

Here we assume that the friction coefficient ζ is uniform for the simulations, and it is

related to the diffusion constant D via $\zeta = k_B T/D$. Each chain consists of N-monomers and the position of i-th monomer is described by $\mathbf{r}_i$. The corresponding local tangent vector is $\mathbf{u}_i = \mathbf{r}_{i+1} - \mathbf{r}_i$. The bending force $\mathbf{F}_i^{bend}$ is derived from the bending energy of discrete form for a WLC model, $\mathbf{F}_i^{bend} = -\frac{\partial \phi^{bend}}{\partial \mathbf{r}_i}$, $\phi^{bend} = \frac{l_p k_B T}{b} \sum_{i=1}^{N-1} (1 - \mathbf{u}_i \cdot \mathbf{u}_{i+1}/b^2)$ [97, 98]. The link force $\mathbf{F}_i^{link}$ provides the connectivity to the chain. For all monomers connected, we add the standard finitely-extensible-nonlinear-elastic (FENE) potential between neighboring monomers [99].

$$U^{FENE}(r) = \begin{cases} -0.5 k_b l n[1 - (r^2/r_0^2)], & r \leq r_0 \\ \infty, & r \geq r_0 \end{cases}, \tag{2.12}$$

where we choose $r_0 = 1.5b$ and the molecular spring constant to be $k_b = 12,\ 74,\ 150\, k_{\mathrm{B}}T/b^2$ for $l_p = 10b,\ 70b,\ 140b$, respectively, in order to keep the bond length to be unity. The total Lennard-Jones potential U_i^{LJ} acting on i-th monomer is the sum of all interaction potentials $U_{i,j}^{LJ}$ from all other monomers and obstacles, which is given by

$$U_{ij}^{LJ} = \begin{cases} 4\epsilon[(\sigma/r_{ij})^{12} - (\sigma/r_{ij})^6 + 1/4], & r_{ij} \leq 2^{1/6}\sigma \\ 0, & r_{ij} \geq 2^{1/6}\sigma \end{cases}, \tag{2.13}$$

where σ is related to the monomeric volume size and set to be unity. The energy strength ϵ is chosen to be 0.025 for both nearest monomer interactions and monomer-obstacle interactions so that the excluded volume is large enough to prevent crossing obstacles and at the same time keep the volume of obstacle as small as possible. The interplay of all interactions determines the bond length to be $1.01b$ with negligible fluctuation (less than 2%). The bond length fluctuation rules the very short time kinetics ($t < t_0$) and is characterized by Rouse-like MSD with $t^{1/2}$ growth. In the remainder, we always discard this early regime. The Brownian force $\mathbf{f}_i$ is assumed to be Gaussian with zero mean and auto-correlation given by $\langle \mathbf{f}_i(t)\mathbf{f}_{i'}(t')\rangle = 4D\delta(t-t')\delta(i-i')$.

We considered stiff chains consisting of $N = 8,\ 16,\ 32,\ 64$ monomers for various values of $l_p = 10b,\ 70b,\ 140b$. Chain length $S = Nb$ varies from $0.05 l_p$ to $6 l_p$.

2.4.2 Simulation Results

Diffusion constant

In a 2-d porous media, the lateral chain fluctuations are restricted and central monomers follow the tube defined by surrounding obstacles (See Fig. 2.2). At regular matrix, the orientational

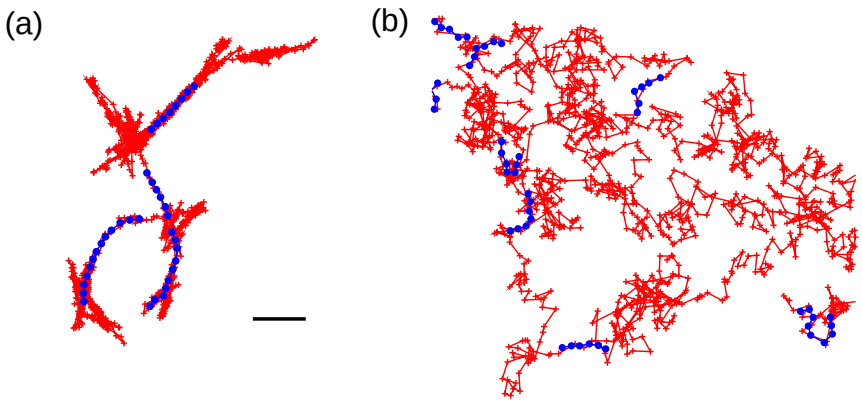

Figure 2.3: Center of mass trajectories of a chain $N = 32$, $l_p = 70b$ in a disordered matrix. (a) $c = 1/(3b)^2$ (b) $c = 1/(40b)^2$. The scale bar has a length $10b$.

degree of freedom is suppressed at high obstacle density but diffusion in longitudinal direction is not restricted. At disordered matrix, the tube ends choose renewal directions resulting in a tube shape similar to the relaxed conformation in the obstacle-free space. Fig. 2.3 demonstrates the trajectories of the center of mass motion ($N = 32, l_p = 70b$) on *disordered* matrices. At low obstacle density ($h = 40b$), the center of mass trajectories are like random-walks (see Fig. 2.4). Upon further confinement, the chain has an inclination of moving straight along the longitudinal direction. The center of mass mainly travels along the longitudinal direction of the chain (see Fig. 2.3(a)) and seldom switches the direction of motion. The very stiff filaments ($S \ll l_p$) kinetics resemble the kinetics of needle-like molecules discussed by [100–102].

The diffusion constant D_N in d-dimensional space is defined through

$$2dD_N = lim_{t\to\infty}\left[\frac{\langle(\delta R(t))^2\rangle}{t}\right]. \tag{2.14}$$

The long time dynamic behavior recovers Fickian diffusion, which assumes that the diffusion constant is $D_N = k_BT/N\zeta$ with ζ being the frictional coefficient of a monomer. Figure 2.4 shows the obstacle density dependence of $\langle(\delta R(t))^2\rangle/D_Nt$ at both regular and disordered obstacle distribution. At low obstacle density ($cS^2 < 1$), chains are not confined, the values of $\langle(\delta R(t))^2\rangle/D_Nt$ collapse to the value 4 of free chain diffusion in 2-d. The difference in diffusion trajectories on regular or disordered matrix is more pronounced at high obstacle density. When the obstacle distribution is regular, the motion in longitudinal direction is not hindered even at

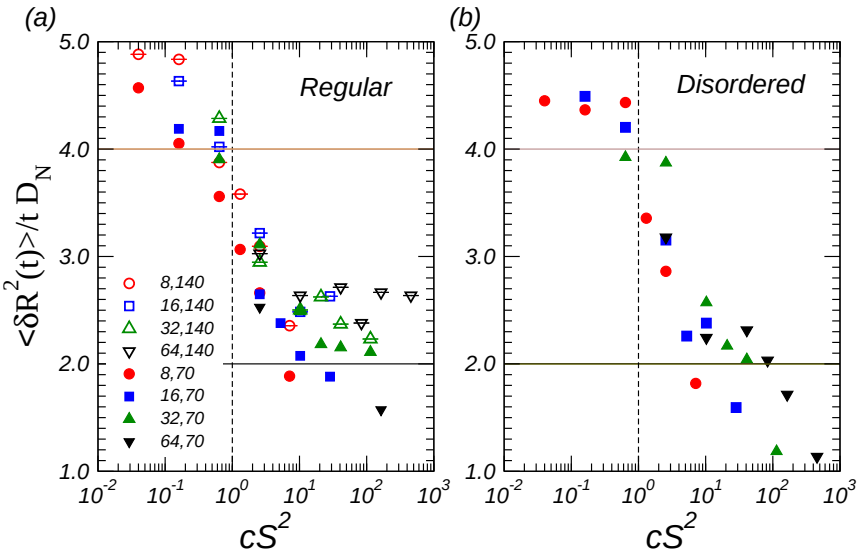

Figure 2.4: (a) Diffusion constant of a chain ($l_p = 70b$ (filled), $l_p = 140b$ (empty)) at regular distribution of obstacles (b) with disordered obstacle distribution. The numbers in the legend are values of chain lengths and l_p. Two solid lines in each panel show the level of diffusion constant of a free chain in 2-d (higher) and 1-d (lower), respectively and the dashed line indicates the obstacle concentration where chains start to be confined.

high obstacle density. As the motion is effectively confined to a tube, the translational mean square displacement per unit time becomes half of the free chain value, $\langle(\delta R(t))^2\rangle/D_N t \sim 2$, at large obstacle density, indicating that the diffusion is mainly one-dimensional. When the chain moves through disordered obstacles, $lim_{t\to\infty}(\delta R(t))^2/D_N t$ is further reduced beyond 2 suggesting that the diffusion constant (expected for asymptotically long times) is lowered by bending energy barriers associated with changes of direction.

Relaxation time τ_d

While diffusing through the 2-d matrix, the rotational correlation of the end-to-end vector of the chain decays. We define the unit vector along the end-to-end vector direction $\mathbf{P}(t) = \frac{\mathbf{r}_N(t)-\mathbf{r}_1(t)}{|\mathbf{r}_N(t)-\mathbf{r}_1(t)|}$ at time t. Then the relaxation of auto-correlation function $\langle \mathbf{P}(t)\cdot\mathbf{P}(0)\rangle$ decays exponentially with characteristic time τ_d.

The chain length dependence of the relaxation time τ_d is shown in Fig. 2.5 for various values of h at both regular and disordered matrix. The theoretical estimates for the reptation time

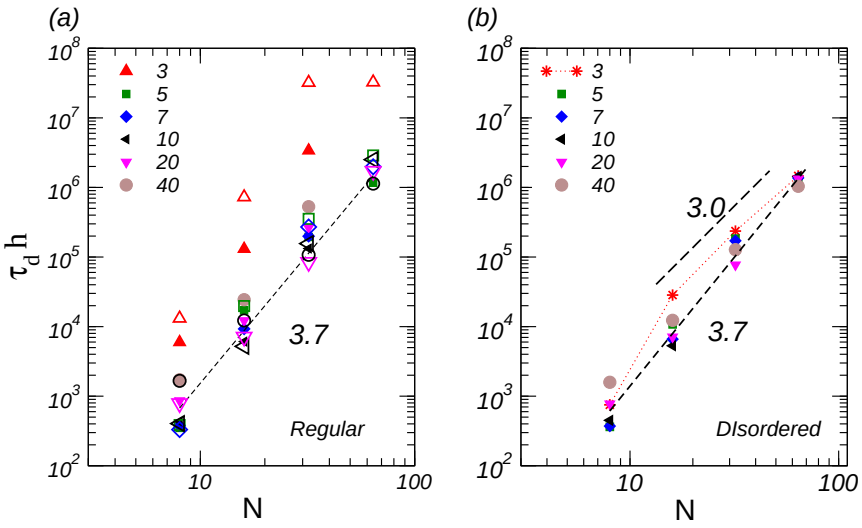

Figure 2.5: Orientational relaxation time τ_d vs. N for a chain diffusing in (a) a regular matrix and (b) a disordered matrix. The numbers in the legend indicate the average obstacle spacing h for each symbol. The chain persistence lengths are $l_p = 70b$ for closed symbols and $l_p = 140b$ for open symbols. The values in y-axis are multiplied by h.

(shown in Section 2.3.1) agree with our simulation results on disordered matrix. For $h = 3b$, relaxation time shows $\tau_d \sim N^3$, as predicted in the limit of $h \ll l_p\sqrt{N}$. At moderate density, we find the relaxation time τ_d scales approximately $\tau_d \sim N^{3.7}$. For short segments $S \sim h$ ($h = 40b$), the exponent becomes smaller than 3.7, as expected from Eq. 2.4.

At regular matrix with high obstacle density ($S \sim l_p \gg h = 3b$), τ_d increases with N faster than $\sim N^{3.7}$. The chain is almost completely squeezed and end-reorientation through obstacles requires large bending.

In our study, translation characterized by the chain self-diffusion time and reorientation characterized by τ_d do generally not grow with the same power of chain length. This is in contrast with experimental results for reptation in the melt [103] where a consistency condition requires the test chain and the matrix chains (providing the obstacles) to behave alike.

Kinetic exponent

In order to investigate the influence of confinement on bending fluctuations in each dynamical regime, we evaluated the MSD of center of mass $\langle(\delta R_{CM}(t))^2\rangle$ and the MSD of central monomers $g_1(t)$. The MSD of center of mass $\langle(\delta R_{CM}(t))^2\rangle$ shows $\sim t$ behaviour for all kinetic

regimes except for a weak plateau region around τ_e (in log/log representation), which is not characteristic enough to describe the reptation kinetics. What is expected and observed from the data (not shown) is that below τ_e both longitudinal and transverse motions of the center of mass are diffusive while above τ_e only the longitudinal motion is diffusive (the transverse fluctuation saturates). Hence the slope of the MSD of center of mass just decreases by a factor 2 around $t \sim \tau_e$. The MSD of central monomers $g_1(t) = \langle(\mathbf{r}_{N/2}(t) - \mathbf{r}_{N/2}(0))^2\rangle$ typically show three kinetic exponents as expected from scaling theory. In order to verify the proposed scaling exponents, we further decompose the mean square displacement of the center monomer into two components. At given time t, the displacement $\mathbf{r}_{N/2}(t) - \mathbf{r}_{N/2}(0)$ is projected to the local chain tangent $\mathbf{e}^{||}$ and its normal vector $\mathbf{e}^{\perp}$ at $t = 0$.

$$\begin{aligned} g_1(t) &= g_1^t(t) + g_1^l(t) \\ g_1^t(t) &= \langle|\mathbf{r}_{N/2,\perp}(t) - \mathbf{r}_{N/2,\perp}(0)|^2\rangle \\ g_1^l(t) &= \langle|\mathbf{r}_{N/2,||}(t) - \mathbf{r}_{N/2,||}(0)|^2\rangle. \end{aligned} \tag{2.15}$$

In Fig. 2.6, the intermediate $\sim t^{0.5}$ regime is clearly seen, where transverse fluctuation is expected to be saturated. For short times ($t < \tau_e$) where $g_1(t) \sim t^{3/4}$, $g_1(t)$ is mainly dominated by growth of the transverse fluctuations. After the entanglement time $t > \tau_e$, the longitudinal MSD grows while the transverse MSD saturates, the growth of $g_1(t) \sim t^{0.5}$ mostly reflects longitudinal fluctuation. The reptation regime is followed by $\sim t^1$, where both transverse and longitudinal fluctuations grow as t^1. The intermediate regime showing $g_1(t) \sim t^{0.5}$ is the signature of confined dynamics.

Figure 2.6(b) and (c) demonstrate such longitudinal/transverse MSD of a filament $N = 64$, $l_p = 70b$ embedded in matrices with disordered obstacles. In the absence of obstacles, the short time behavior of $g_1^t(t)$ and $g_1^l(t)$ show transverse and longitudinal dynamic growth $\sim t^{3/4}$ and $\sim t^{7/8}$, respectively, as expected from free filament kinetics. Both $g_1^t(t)$ and $g_1^l(t)$ become diffusive in long time limit. In the presence of obstacles, the early free kinetics is interrupted by confinement at time $\tau_e \sim h^{8/3} l_p^{1/3}$ when the chain starts experiencing obstacles. The transverse fluctuation $g_1^t(t)$ saturates at a "plateau" level, imposed by the tube width. The plateau value in $g_1^t(t)$ corresponds to the size of average monomeric fluctuation within the tube $\sim h^2$. As the chain enters the reptation regime, the longitudinal relaxation at intermediate times ($\tau_e < t < \tau_r$) is depicted by $g_1^{||}(t)$ that grows like $\sim t^{0.5}$ as predicted from Eq. 2.7. When obstacles are rare, $\sim t^{7/8}$ regime of free filament-like fluctuation is seen at short times. In the limit of large obstacle

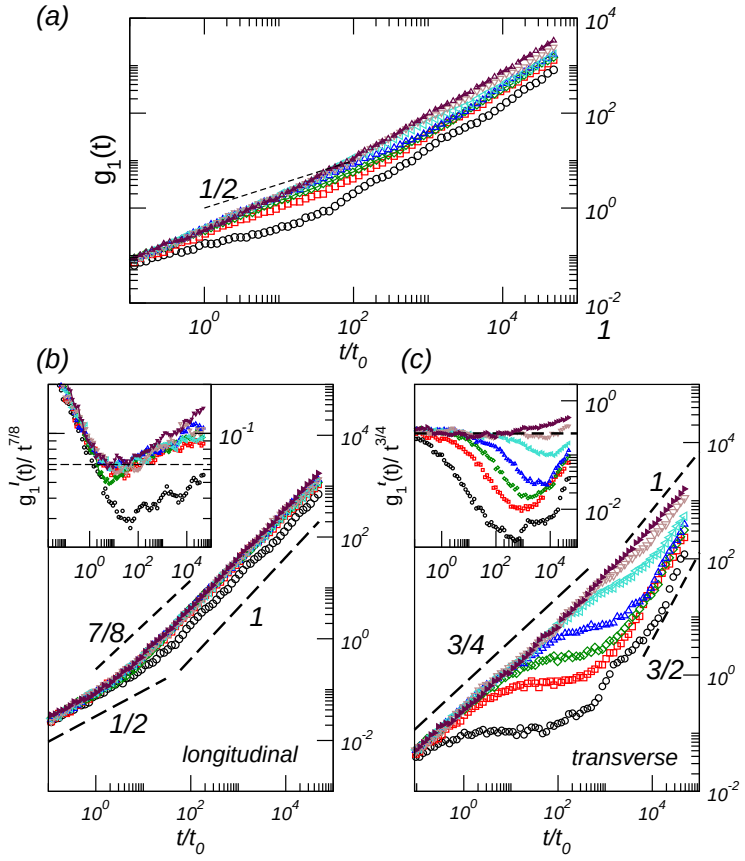

Figure 2.6: Time dependent growth of g_1 $l_p = 70b$, $N = 64$. The obstacle are distributed with weak disorder with average spacing h, which is decreasing from top to bottom, $h = \infty, 40, 20, 10, 7, 5, 3b$ (a) top panel is $g_1(t)$ (b) longitudinal MSD of central monomers with an inset showing $g^l/t^{7/8}$. (c) transverse MSD of central monomers and the inset is $g^t/t^{3/4}$.

density such as $h = 3b$, the intermediate regime already starts at short times and is followed by t^1 regime. No free longitudinal regime can be seen in this case. After relaxation of the internal degrees of freedom, the longitudinal MSD grows with time $\sim t^1$ in the reptation regime while transverse MSD shows a sharp upturn $\sim t^{3/2}$ (Eq. 2.9). For the intermediate obstacle density we expect to see $\sim t^{0.5}$ between $t^{7/8}$ and t^1 regimes. (Nevertheless, in our simulation with short chains $l_p = 70b$, $N = 64$, it was difficult to see $\sim t^{0.5}$ regime after $t^{7/8}$ at intermediate obstacle density.)

Our theory predicts the prefactors (Eq. 2.10) of time dependent transverse/longitudinal MSD. The transverse fluctuation under strong confinement is predicted to be independent of

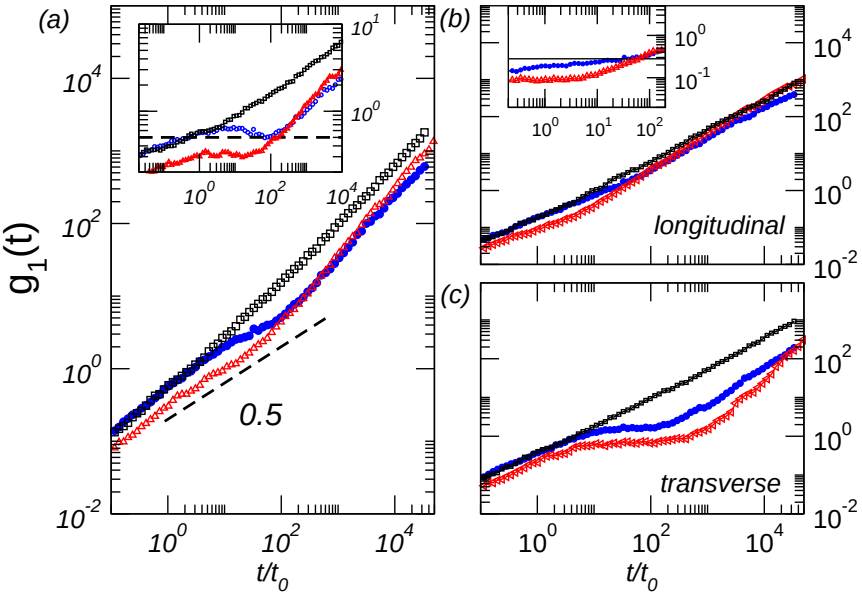

Figure 2.7: The central monomer MSD $g_1(t)$ for a chain of length $N = 64$ with $l_p = 10b$ (middle in blue) is compared with $l_p = 70b$ (bottom in red) on a regular matrix with $h = 5b$. The top curve (in black) is for $l_p = 10b$ in unconfined matrix with $h = 40b$.

l_p. Nevertheless the data in Fig. 2.7 show an increase of the plateau value for weaker confinement where $l_p = 2h$, $S \gg h$. Below, we use the measured value of transverse fluctuation $\langle r_\perp^2 \rangle$ as an input for evaluating Eq. 2.10.

- **Amplitude of $t^{7/8}$ in the early longitudinal MSD g_1^l.**
  The plateau value 0.065 measured from the inset of Fig. 2.6(b) is compatible with the prefactor 0.04, of $t^{7/8}$ calculated from Eq. 2.10 with $l_p = 70b$, $\zeta = 1$.

- **Amplitude of $t^{3/4}$ in the early transverse MSD g_1^t.**
  The plateau value 0.27 measured from the inset of Fig. 2.6(c) is in accordance with the prefactor 0.27 of $t^{3/4}$ calculated from Eq. 2.10, with $l_p = 70b$, $\zeta = 1$.

- **Extension of the intermediate regime and amplitude of $t^{1/2}$ in g_1^l.**
  Fig. 2.7 shows the influence of stiffness on the length of the intermediate kinetic regime $\sim t^{0.5}$. For $N = 64$, chains with $l_p = 10b$, $70b$ are compared. The cross over time τ_r where t^1 diffusion sets in is smaller for stiffer chain ($l_p = 70b$), which agrees with Eq. 2.8. The plateau value for a chain with stiffness l_p is expected to be $\propto \sqrt{\langle r_\perp^2 \rangle / l_p}$. The plateau

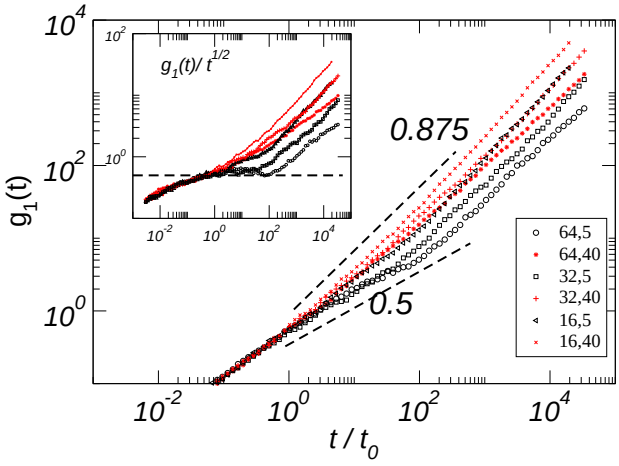

Figure 2.8: The growth of MSD $g_1(t)$ for $l_p = 10b$, $N = 16, 32, 64$ are shown for $h = 5b$ (black) and $h = 40b$ (red). The inset shows $g_1(t)$ normalized by $t^{0.5}$. The numbers in the legend are chain lengths N and obstacle spacing h.

value 0.2 measured from the inset of Fig. 2.7(b) is close to the prefactor 0.16 of $t^{1/2}$ calculated from Eq. 2.10 with $l_p = 10b$, $\langle r_\perp^2 \rangle = 1.7b^2, \zeta = 1$. The measured ratio 3.85 of the plateau values between two chains with $l_p = 10b$ and $l_p = 70b$ is in good agreement with the value 4.12 predicted from Eq. 2.10. The ratio between τ_r and τ_e is calculated from Eq. 2.10 as ~ 25 and measured from the $\sim t^{1/2}$ regime to be about ~ 20 when $l_p = 10b$. When $l_p = 70b$, both predicted value and measured values of τ_r/τ_e are about $2-3$, which is markedly smaller. We can hardly observe the $t^{1/2}$ regime for shorter chains ($N = 32$, $l_p = 70b$, $h = 5b$). Figure 2.8 demonstrates the range of parameters where the intermediate $t^{0.5}$ can exist when a chain with given persistence length $l_p = 10b$ varies its length ($S/l_p > 1$) as $N = 16, 32, 64$ under "tube widths" $h = 5b$ and $40b$. When $h = 5b$, the intermediate regime $t^{0.5}$ appears for longer chain lengths $N = 32, 64$ but not for $N = 16$ and when $h = 40b$ the chain is never confined enough to show $t^{1/2}$ regime.

In Fig. 2.9, we illustrate the influence of disorder in the obstacle distribution. The transverse fluctuation g_1^t in the reptation regime is larger for disordered matrix when obstacle spacing is larger than $h = 3b$ as disorder in obstacle arrangement allows larger fluctuation for less confined chains. At the tightest confinement $h = 3b$ where $h/l_p \ll 1$, however, g_1^t is smaller at the disordered matrix. In the case $l_p \gg h$, a chain is constrained by many gates within one persistence length. Due to the chain stiffness the effective tube diameter is controlled by

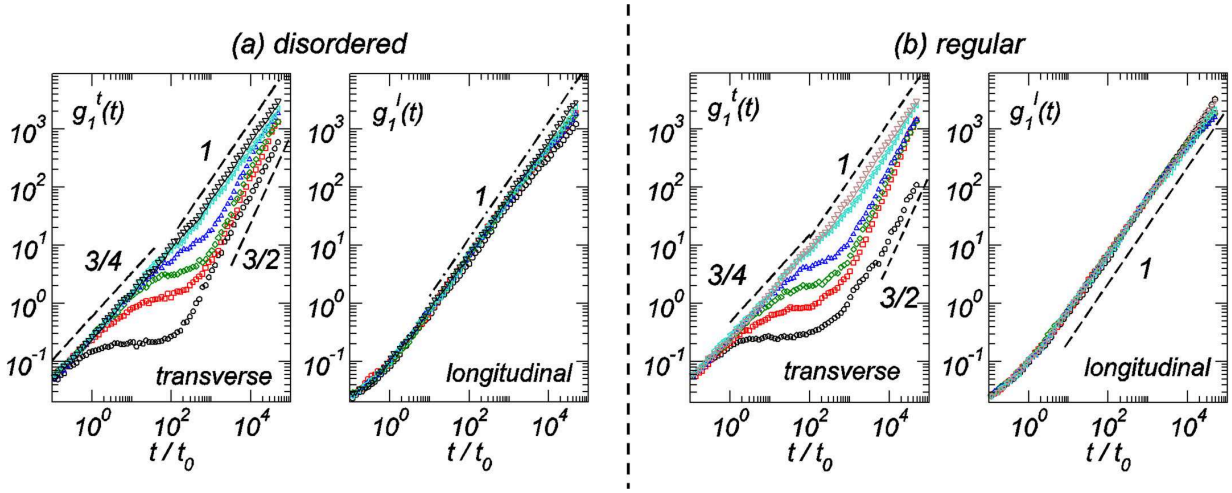

Figure 2.9: Transverse/longitudinal component of $g_1(t)$ for $l_p = 70b, N = 32$ in (a) a disordered matrix and (b) a regular matrix. The average obstacle spacing h is decreasing from top to bottom, $h = \infty, 40, 20, 10, 7, 5, 3b$. The transverse fluctuation in the reptation regime is larger in the disordered matrix for $h > 3b$.

the tightest obstacles. In this limit the fluctuation is now smaller with disorder. The $g_1^t \sim t^1$ regime sets in earlier in the regular matrix when average obstacle spacing is $h > 3b$. We do not observe any $\sim t^{1/2}$ regime from longitudinal component of $g_1^l(t)$ as expected for very short chains $S/l_p \ll 1$. At all obstacle densities, longitudinal fluctuations collapse on top of each other at early times, indicating that the dynamics is controlled by the chain frictional coefficient only. At long times, the larger obstacle density plays a role on the chain diffusion as also discussed earlier in Section 2.4.2 and 2.4.2.

Below, we summarize the obstacle density dependence of semiflexible chain kinetics captured by MSDs of monomers.

- **Low obstacle concentration** $(S < h)$
  The influence of obstacles is negligible, and the free chain kinetics is recovered. The transverse fluctuation grows with $\sim t^{3/4}$ and the longitudinal fluctuation with $\sim t^{7/8}$.

- **Moderate obstacle concentration** $(h/l_p \leq 1,\ S > h)$
  The transverse kinetic exponent varies $\sim t^{3/4}$, t^0, and $t^{3/2}$ before the Fickian diffusion $\sim t^1$. The longitudinal fluctuation shows $t^{7/8}$ at earlier times before the confinement affects the chain motion. At entanglement time, chain enters reptation regime where

MSD grows with $t^{1/2}$ followed by $\sim t^1$. The exponent 0.5 is only seen for longer chains ($S \geq l_p$)

- **Large obstacle concentration** ($h/l_p \ll 1$, $h = 3b$) The longitudinal fluctuation at very short time is already confined and kinetics is depicted by exponent 0.5 followed by 1. The exponent 0.5 is not seen for very short chains ($S \ll l_p$). In dense regular matrix, the Fickian diffusion sets in earlier.

2.5 Drift and diffusion of a semiflexible chain confined by a harmonic potential

2.5.1 Equilibrium statistics of the confined filament

Let us consider a Worm Like Chain of total length S and persistence length l_p laterally confined by a Harmonic potential of stiffness κ_h per unit length $V_{conf} = \int_{-S/2}^{S/2} \frac{1}{2}\kappa_h r_\perp^2(s)ds$, where the curvilinear coordinate along the chain is ranging from $-S/2$ to $S/2$. In practice we consider chains of length $S \to \infty$ with (quasi) continuous spectrum. Let us introduce the Fourier transform $\mathrm{f}_q = \int_{-S/2}^{S/2} \mathrm{d}s\, \mathrm{f}(s) \exp(-iqs)$, $\mathrm{f}(s) = \frac{1}{S}\sum_q \mathrm{f}_q \exp(iqs)$. In the limit of continuous spectrum the sum over q turns into an integral $\frac{1}{S}\sum_q \to \int_{-\infty}^{+\infty} \frac{\mathrm{d}q}{2\pi}$. We represent the total Hamiltonian accounting for bending energy and confinement in Fourier space as:

$$H = \frac{1}{S}\sum_q (l_p q^4 + \lambda q^2 + \kappa_h) r_{\perp,q}^2/2 - \lambda S, \tag{2.16}$$

where we introduced the force λ ultimately taken to be zero to ease the calculation of averages. Here and below we use thermal units with $k_\mathrm{B}T = 1$. The free energy of the quadratic Hamiltonian Eq. 2.16 can be expressed as a sum over Fourier modes:

$$F = \frac{\alpha}{2}\sum_q \log(l_p q^4 + \lambda q^2 + \kappa_h) - \lambda S + \mathrm{const}, \tag{2.17}$$

with α the number of transverse directions. Below, we will use the continuous limit and omit the inessential constant:

$$F = S\frac{\alpha}{2}\int \frac{dq}{2\pi}\log(l_p q^4 + \lambda q^2 + \kappa_h) - \lambda S. \tag{2.18}$$

Obviously the average transverse displacement vanishes $\langle r_\perp \rangle = 0$. The transverse fluctuation averaged along the chain $\frac{1}{S}\int_{-S/2}^{S/2} \mathrm{d}s \langle r_\perp^2 \rangle$ is obtained by taking the derivative of the free energy per unit length with respect to $\kappa_h/2$ at $\lambda = 0$:

$$\langle r_\perp^2 \rangle = \int \frac{\alpha}{\kappa_h + l_p q^4}\frac{\mathrm{d}q}{2\pi}, \tag{2.19}$$

where we do not mention the unessential average along the chain anymore. Calculating the integral we get:

$$\langle r_\perp^2 \rangle = \frac{\alpha}{2\sqrt{2}}\frac{l_1^3}{l_p}. \tag{2.20}$$

The fluctuation $\langle r_\perp^2 \rangle$ is governed by the static correlation length $l_1 = l_p(\kappa_h l_p^3)^{-1/4}$ in the confining potential. Thus the harmonic potential with stiffness κ_h is related to the effective channel width h by $h = \langle r_\perp^2 \rangle^{1/2} \sim l_p^{1/8}\kappa_h^{3/8}$. The length l_1 is the typical contour length between two deflected points due to confinement [25]. In the following, in view of later generalization, we will use the correlation length l_1 rather than the stiffness κ_h explicitly related to the harmonic potential. Integrating Eq. 2.20 back with respect to $\kappa_h/2$, we obtain the confinement energy $F = S\frac{\alpha}{\sqrt{2}l_1}$. We may also take the limit $\kappa_h \to 0$ of a free chain. The fluctuation is then governed by the chain length S, the integral in Eq. 2.19 is diverging like $\sim 1/(l_p q_{min}^3)$ with $q_{min} \sim 1/S$ in accordance with the scaling $\langle r_\perp^2 \rangle \sim S^3/l_p$ [90, 93, 94].

The first derivative of the free energy with respect to λ gives the average chain extension $\langle L \rangle$ and the second derivative its fluctuation $\langle \delta L^2 \rangle$:

$$\langle L \rangle = -\frac{\partial F}{\partial \lambda} = S - S\frac{\alpha}{2}\int \frac{dq}{2\pi}\frac{q^2}{l_p q^4 + \lambda q^2 + \kappa_h} \tag{2.21}$$

$$\langle \delta L^2 \rangle = S\frac{\alpha}{2}\int \frac{dq}{2\pi}\frac{q^4}{(l_p q^4 + \lambda q^2 + \kappa_h)^2} \tag{2.22}$$

By setting $\lambda = 0$, we obtain

$$\langle L \rangle = S\left(1 - \frac{\alpha}{4\sqrt{2}}\frac{l_1}{l_p}\right) \tag{2.23}$$

$$\langle \delta L^2 \rangle = \frac{\alpha}{16\sqrt{2}}\frac{S l_1^3}{l_p^2}. \tag{2.24}$$

We apply the above expressions for the average extension and its fluctuation for a free chain by setting $\kappa_h = 0$ in the integrals. The integrals are now formally divergent and dominated by $q_{min} \sim 1/S$ in agreement with the scaling $\langle \delta L^2 \rangle \sim \frac{S^4}{l_p^2}$ [90, 93, 94].

2.5.2 Transverse dynamics

We consider a very long almost straight filament with a transverse force distribution $f_\perp(s,t)$ applied at positive times. The transverse response function $R_\perp(s,t)$ measures the response (average displacement here) after a time t to the excitation (transverse force, $f_\perp$) a distance s away. The average displacement is given by the weighted sum of the force at previous times and different position as follows

$$\langle r_\perp \rangle = \int_{-\infty}^{\infty} ds' \int_0^t dt' R_\perp(s - s', t - t') f_\perp(s', t'). \tag{2.25}$$

Often we will specialize to the case of a force applied in the middle of the filament ($s = 0$). In the harmonic confinement potential, the dynamical equation for the average displacement under an external force distribution $f_\perp(s,t)$ is given by

$$\zeta_\perp \frac{\partial \langle r_\perp \rangle}{\partial t} = -l_p \frac{\partial^4 \langle r_\perp \rangle}{\partial s^4} - \kappa_h \langle r_\perp \rangle + f_\perp, \tag{2.26}$$

where $\zeta_\perp$ is transverse frictional coefficient per unit length[2]. After Fourier-Laplace transformation, we obtain,

$$p\zeta_\perp \langle r_{\perp,q} \rangle = (-l_p q^4 - \kappa_h)\langle r_{\perp,q} \rangle + f_{\perp,q}, \tag{2.27}$$

[2]When hydrodynamic interactions are taken into account, the frictional coefficients per unit length, $\zeta_\parallel$ and $\zeta_\perp$, are similar to those for a rod and carry logarithmic corrections in free space, $\zeta_\parallel = 2\pi\eta_s/\log(S/b)$, $\zeta_\perp \approx 4\pi\eta_s/\log(S/b)$ with η_s being solvent viscosity and b the chain thickness. In our case of fluctuating filaments, the upper cut-off length S is replaced by the longitudinal/transverse dynamic correlation length respectively. For confined filaments the details of hydrodynamic boundary conditions matter.

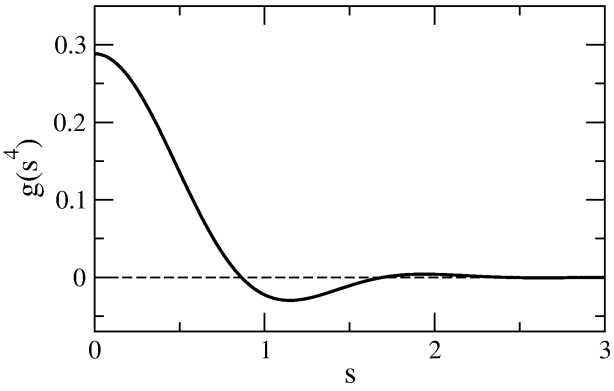

Figure 2.10: The position dependence part $g(\tilde{s}^4)$ in response function $R_\perp(s,t)$. The region of negative values suggest that the corresponding chain section moves opposite direction against applied force at $\tilde{s}=0$.

where p is the Laplace variable conjugated to time. The response function is written as $R_\perp(q,p)=\langle r_{\perp,q}\rangle/f_{\perp,q}$ after Fourier-Laplace transformation, which can be read from Eq. 2.27:

$$R_\perp(q,p)=\frac{1}{p\zeta_\perp+l_pq^4+\kappa_h}. \tag{2.28}$$

Using the fluctuation-dissipation theorem, the response function gives also access to the transverse fluctuation of the center monomer. The fluctuation-dissipation theorem is given as being written here for the transverse fluctuation:

$$\langle r_\perp(s,t)r_\perp(0,0)\rangle=\int_t^\infty R_\perp(s,t')\mathrm{d}t'. \tag{2.29}$$

A similar equation holds for longitudinal fluctuations where transverse quantities are replaced by longitudinal quantities (with also a different response function). The proper response function for the central monomer $R_\perp(s=0,p)$ is obtained from Eq. 2.28 through the inverse Fourier transform: $R_\perp(s=0,p)=\int_{-\infty}^{\infty}R_\perp(q,p)\frac{dq}{2\pi}$. Performing this integral, the drift of the center monomer reads:

$$\langle r_\perp^c(0,t)\rangle=f\langle r_\perp^2\rangle\frac{\gamma(\frac{3}{4},t\kappa_h/\zeta_\perp)}{\Gamma(\frac{3}{4})}, \tag{2.30}$$

where $\langle r_\perp^2\rangle$ stands for the equilibrium fluctuation (Eq. 2.20) in the direction of the force (hence $\alpha=1$ should be taken in Eq. 2.20) and $\Gamma(\beta)$, $\gamma(\beta,x)$ are the complete and incomplete Gamma

functions of index β. The small argument expansion $\gamma(\beta, x) \sim x^\beta/\beta$ restores the free transverse drift $\frac{f\Gamma(1/4)}{3\pi}(t\zeta_\perp^{-1}l_p^{-3})^{3/4}l_p^2$. This power law asymptotics was previously given in Ref. [94]. At large times the average transverse displacement saturates, the ratio of the complete to incomplete Gamma function goes to unity, and the static fluctuation-dissipation theorem is recovered.

Dynamical fluctuations are also given by the fluctuation-dissipation theorem: $\langle(\delta r_\perp^c)^2\rangle = \frac{2\alpha}{p}R_\perp(s=0,p) = 2\alpha\langle r_\perp^c\rangle/f$ and dominate over drift at small enough time/force. Below, we now describe how the shape of the filament develops in time. To that end, we need $R_\perp(s,t)$ which gives the average transverse velocity through $\langle\frac{\mathrm{dr}_\perp}{\mathrm{dt}}\rangle = R_\perp(s,t)f$. Using $R_\perp(q,t) = \frac{1}{\zeta_\perp}\exp\left(-\kappa_h t/\zeta_\perp\right)\exp\left(-l_p q^4 t/\zeta_\perp\right)$, we express $R_\perp(s,t)$ by means of hypergeometrical series.

$$\begin{aligned} R_\perp(s,t) &= \frac{1}{\zeta_\perp}\left(\frac{\zeta_\perp}{l_p t}\right)^{1/4}\exp(-\kappa_h t/\zeta_\perp)\mathrm{g}(\tilde{\mathrm{s}}^4) \\ \text{with}: \quad \tilde{s} &= \frac{s}{\lambda_t},\ \ \lambda_t \equiv 4\left(\frac{\zeta_\perp}{l_p t}\right)^{-1/4}, \end{aligned} \tag{2.31}$$

where $\tilde{s}$ is the curvilinear coordinate reduced by the actual correlation length λ_t at time t. The scaling function $\mathrm{g(x)}$ giving the shape of the velocity profile along the filament can be expressed as:

$$\mathrm{g(x)} = \frac{1}{\pi}\left(\Gamma[\frac{5}{4}]\mathrm{F}[\{\},\{\frac{1}{2},\frac{3}{4}\},\mathrm{x}] - 2\sqrt{\mathrm{x}}\Gamma[\frac{3}{4}]\mathrm{F}[\{\},\{\frac{5}{4},\frac{3}{2}\},\mathrm{x}]\right),$$

with hypergeometrical series depending on one set of indices only (the set $\{a_i\}$ is empty),

$$\mathrm{F}[\{\mathrm{a_i}\},\{\mathrm{b_j}\},\mathrm{x}] = \sum_{\mathrm{n}=0}^{\infty}\Pi_{\mathrm{i,j}}\frac{\Gamma[\mathrm{a_i}+\mathrm{n}]\Gamma[\mathrm{b_j}]}{\Gamma[\mathrm{a_i}]\Gamma[\mathrm{b_j}+\mathrm{n}]}\frac{\mathrm{x}^\mathrm{n}}{\mathrm{n!}}.$$

The function $\mathrm{g}(\tilde{s}^4)$ is plotted as a function of $\tilde{s}$ in Fig. 2.10. It oscillates and changes sign first at about $\tilde{s} = 0.86$. The region of negative values suggests that the corresponding chain section moves opposite direction against applied force at $s = 0$. The length scale of oscillations is given by the transverse dynamic correlation length λ_t in Eq. 2.31. These oscillations are reminiscent of the static correlations obtained by Choi et al. [104], which can be also derived from the dynamic response function Eq. 2.28 with $p = 0$.

For a finite filament, the correlation length eventually reaches the filament length. At larger time, the shape becomes sensitive to the boundary condition applied at the end of filament. In principle, the linear response function can also be applied to a free filament ($\kappa_h = 0$), where the response by a constant transverse force f will be eventually large. In

this case, it is important to discuss the limitation of the linear response. Recently, Obermayer and Hallatschek [105] argued that the first non-linearity arises from the coupling of longitudinal and transverse response. The qualitative argument is the following: due to filament length conservation, a large lateral deformation can only develop upon dragging in length from the side, hence creating a longitudinal motion. The associated drag force generates a tension distribution along the filament. This tension σ acts against developing curvature along the filament via the standard restoring force $\sigma\Delta^2 r_\perp$, which is non-linear in $r_\perp$ and f. Repeating the scaling arguments of Ref. [105] in our notations leads to the crossover time $t_{n.l.}$

$$t_{n.l.} \sim \frac{\zeta_\perp^{11/7}\zeta_\parallel^{-4/7} l_p^3}{(f l_p)^{16/7}}. \tag{2.32}$$

After time $t_{n.l.}$, the response is not linear. At early times, the linear response applies as the fluctuation dominates over drift at weak force regime $f\langle r_\perp\rangle < 1$, this criterion defines the characteristic time t_f

$$t_f \sim \frac{\zeta_\perp l_p^3}{(f l_p)^{8/3}}. \tag{2.33}$$

Formally, there is a time window $t_f < t < t_{n.l.}$ to see a clean drift which is linear in force at strong force regime $f l_p \gg 1$. Considering $1\, k_\mathrm{B}T = 4.1$ pN·nm, $f = k_\mathrm{B}T/l_p \sim 0.1$ pN corresponds to the stretching transition. At weak force regime $f l_p < 1$, on the other hand, the linear regime is washed out by fluctuations, and the nonlinear response sets in before t_f. We come back to the propagation of tension described in Section 2.3.3. Recently, nonlinear dynamics is described in response to sudden changes in externally applied forces [106], where the tension dynamics within the various asymptotic limits is investigated for particular scenarios.

2.5.3 Longitudinal dynamics

We introduce the longitudinal coordinate $r_\parallel(s)$. At equilibrium (in the absence of force) the variation of $\langle r_\parallel\rangle(s)$ is almost proportional and very close to that of s in the weak fluctuation regime of interest [107]. At the expanse of a slight renormalization of s, we may hence replace $\langle r_\parallel\rangle$ by s and define the relevant deviation $\delta r_\parallel = r_\parallel - s$ with zero average at equilibrium. In the following, we will omit small inessential corrections arising from the renormalization of s. As mentioned in Ref. [89], due to filament incompressibility, longitudinal fluctuations

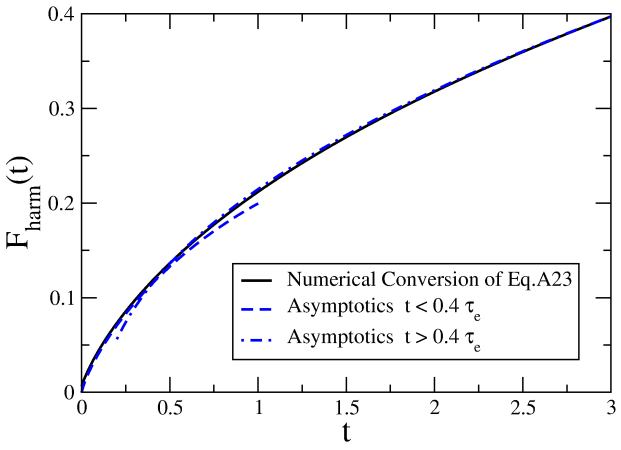

Figure 2.11: Scaling function F_{harm} obtained by numerical back transform of Eq. 2.39 together with the matched asymptotics, Eq. 2.42.

are limited by the propagation of the tension σ. Filament incompressibility expressed to the lowest order by $\left\langle \frac{\mathrm{d}r_{\parallel,s}}{\mathrm{d}s} \right\rangle \approx 1 - 1/2 \left\langle \left(\frac{\mathrm{d}r_{\perp,s}}{\mathrm{d}s} \right)^2 \right\rangle$ induces coupling between the longitudinal and transverse displacements $iq\langle \delta r_{\parallel,q} \rangle = -q^2 \frac{1}{S} \langle r_{\perp,q} r_{\perp,-q} \rangle / 2$. There is the linear relation between the deformation $\left\langle \frac{\mathrm{d}\delta r_{\parallel}}{\mathrm{d}s} \right\rangle$ and the tension σ related to the incompressibility constraint, explicitly:

$$\left\langle \frac{\mathrm{d}\delta r_{\parallel}}{\mathrm{d}s} \right\rangle = J\sigma, \tag{2.34}$$

where the compliance J happens to have dimension of length ($k_{\mathrm{B}}T = 1$). We anticipate this relation to be local in space (J does not depend on q) but not in time, thus J may depend on the Laplace variable p. An explicit derivation is given in Appendix 5.6 as

$$J = \frac{l_1^3}{l_p^2} \frac{1}{2\sqrt{2}\{1 + (1+\tilde{p})^{1/4}\}\{1 + (1+\tilde{p})^{1/2}\}} \quad \text{with} \quad \tilde{p} = p\tau_e, \tag{2.35}$$

where τ_e is the entanglement time introduced earlier as $\tau_e = \zeta_\perp / 2\kappa_h = \zeta_\perp l_1^4 / 2 l_p$.

All we need is to calculate the longitudinal response function which also gives access to the fluctuations. Under the external force f_q, the response $\langle \delta r_{\parallel,q} \rangle$ satisfies the dynamical equation:

$$\zeta_\parallel \frac{\mathrm{d}\langle \delta r_{\parallel,q} \rangle}{\mathrm{d}t} = \frac{\mathrm{d}\sigma_q}{\mathrm{d}s} + f_q, \tag{2.36}$$

with $\zeta_\parallel$ being longitudinal frictional coefficient per unit length.

Next we are going to use the compliance J to express the longitudinal response function. Inserting $iq\langle\delta r_{\parallel,q}\rangle = J\sigma_q$ in the longitudinal dynamical equation Eq. 2.36 yields the response function $R_\parallel(q,p) = \langle\delta r_{\parallel,q}\rangle/f_q$ as a function of J:

$$R_\parallel(q,p) = \frac{1}{p\zeta_\parallel + q^2/J}. \tag{2.37}$$

As for the transverse motion described in the Section 2.5.2, the longitudinal motion of the central monomer is described by the integral of the response function over reciprocal space, $\langle\delta r_\parallel^c\rangle = \frac{f}{p}\int \frac{\mathrm{d}q}{2\pi} R_\parallel(q,p)$. Doing the integral we obtain:

$$\langle\delta r_\parallel^c\rangle(p) = \frac{f}{2}\frac{J^{1/2}l_p^{3/2}}{p^{3/2}(\zeta_\parallel l_p^3)^{1/2}}. \tag{2.38}$$

The crossover between the free regime and longitudinal relaxation regime occurs around the time τ_e. It is convenient to use the reduced time t/τ_e conjugated to $\tilde{p}$ and rephrase the Laplace transform ($f(\tilde{p}) = f(p)/\tau_e$):

$$\begin{aligned}\langle\delta r_\parallel^c\rangle(\tilde{p}) &= \frac{f}{\sqrt{2}}\frac{l_1^3}{l_p}\left(\frac{\tau_e}{\zeta_\parallel l_1^3}\right)^{1/2}\mathrm{F}_{harm}(\tilde{p}) \\ \mathrm{F}_{harm}(\tilde{p}) &= \frac{1}{2^{5/4}}\frac{1}{\sqrt{1+(1+\tilde{p})^{1/4}}\sqrt{1+(1+\tilde{p})^{1/2}}}\frac{1}{\tilde{p}^{3/2}}.\end{aligned} \tag{2.39}$$

For large times $t \gg \tau_e$ ($p \ll 1$), we obtain a $\sqrt{t}$ asymptotics:

$$\langle\delta r_\parallel^c\rangle(t) = \frac{f}{2^{7/4}\sqrt{\pi}}\frac{l_1^3}{l_p}\sqrt{\frac{t}{\zeta_\parallel l_1^3}}. \tag{2.40}$$

This regime corresponds to relaxed transverse fluctuations and is hence independent of $\zeta_\perp$. A similar $t^{1/2}$ regime is reported in Ref. [94] which misses the earlier $t^{7/8}$ regime arising from the tension propagation. In the theory of rheology [85–87], this regime is manifested in a $\omega^{1/2}$ dependency of the shear moduli. It arises from the compliance J going to a constant value.

For small times $t \ll \tau_e$ ($\tilde{p} \gg 1$), free dynamics is recovered:

$$\langle \delta r_{\parallel}^{c} \rangle (t) = \frac{f}{2^{11/8}\Gamma(\frac{15}{8})} l_p^2 \left(\frac{t}{\zeta_{\perp}^{3/7} \zeta_{\parallel}^{4/7} l_p^3} \right)^{7/8}. \tag{2.41}$$

It is convenient to also represent the scaling function F_{harm} as a function of reduced time $\tilde{t} = t/\tau_e$. The inverse Laplace transform of $\mathrm{F}_{harm}(\tilde{p})$ obtained numerically from the Stehfest algorithm is plotted in Fig. 2.11 together with the matched asymptotics:

$$\mathrm{F}_{harm}(\tilde{t}) = \begin{cases} \frac{\tilde{t}^{7/8}\left(-\frac{2\sqrt{\tilde{t}}}{\Gamma\left(\frac{19}{8}\right)} - \frac{8\sqrt[4]{\tilde{t}}}{\Gamma\left(\frac{17}{8}\right)} + \frac{16}{\Gamma\left(\frac{15}{8}\right)} \right)}{32\sqrt[4]{2}}, & \left(\tilde{t} < 0.4\right) \\ \frac{32\tilde{t}-3}{64\sqrt[4]{2}\sqrt{\pi\tilde{t}}}, & \left(\tilde{t} > 0.4\right) \end{cases} \tag{2.42}$$

We can apply the fluctuation dissipation theorem to calculate the longitudinal fluctuation of the "middle monomer" $\langle (\delta r_{\parallel}^{c})^2 \rangle = \frac{2}{p} \int \frac{\mathrm{d}q}{2\pi} R_{\parallel}(q,p)$, as we did for the transverse fluctuations. We obtain: $\langle (\delta r_{\parallel}^{c})^2 \rangle = \frac{2}{f} \langle \delta r_{\parallel}^{c} \rangle$. More details on longitudinal dynamics can be found in Ref. [96]

2.6 Conclusion

In this chapter, we studied the reptational kinetics of a stiff semiflexible chain by means of scaling analysis and computer simulations. We mainly consider rather stiff chains of length shorter than (or comparable to) the persistence length whose free conformations are almost straight. In the presence of obstacles, the tube in which the chain is living is only weakly curved. As the obstacle density increases, the free dynamics changes to reptational dynamics. Like for flexible chains in a polymer melt, the tube picture can be applied in order to characterize the chain motion. The free anisotropic dynamics is recovered at early times $t < \tau_e$. After the entanglement time τ_e, transverse modes are equilibrated but the chain is not yet correlated over its whole length, longitudinal modes have to relax. In this intermediate relaxation regime, the longitudinal fluctuations grow as $\sim \sqrt{t}$. Finally chain ends are correlated after time $\tau_r \sim S^2$. The chain then diffuses globally along the tube and tube renewal takes place. The end-to-end orientation relaxes upon tube renewal with characteristic time $\tau_d \sim S^3$. Note that the intermediate $\sqrt{t}$ regime is absent for short/ill-confined chains, for which the longitudinal tension is equilibrated before transverse fluctuation saturates.

Our results are supported by Langevin simulations. To illustrate the anisotropic chain dynamics, we study the mean square displacement of the central monomer and its transverse and longitudinal components. This allows to clearly see the exponents for transverse and longitudinal fluctuations of a free chain reported previously [89]. In the presence of obstacles, an intermediate slow regime opens between the free chain regime and the diffusive regime. It has the $\sim t^{1/2}$ signature of the internal relaxation as predicted from our scaling arguments.

Upon developing our theory, we study the linear response of a semiflexible chain to an external force, in which different transverse and longitudinal frictions per unit chain length are used. This helps to make the physics more transparent at many places: for example, the transverse friction drops out after the entanglement time τ_e. To avoid the inessential complexity due to the various boundary conditions, we formally considered an infinite filament. Our results are general at short times when the application point of the force does not correlate to the boundary. Using the calculated response functions, the fluctuation of the central monomer is explicitly obtained. The expected "plateau" values estimated by power law asymptotics in the explicit calculations are in good agreement with those from the simulations. Also, results apply to three dimensional space where the friction is anisotropic. Finally even on a substrate transverse and longitudinal friction with the substrate could be different if the filament has proper structure.

In this chapter, we did not exhaust the problem of WLC in obstacles and additional effects could arise from tube curvature for example. Reorientation mechanisms of a chain could be another additional effect on reptational dynamics in obtacles. In Appendix 5.6, we briefly present simulation results on the reorientation dynamics of a grafted semiflexible chain in both the absence and presence of obstacles. The system studied here also has some relevance to dense solution of semiflexible chains and some of our results have their counterpart in rheology as mentioned above. Again some hydrodynamic effects should be expected at short times and activation barriers against reptation should slow down long time dynamics.

Chapter 3

Scraping and stapling of end-grafted DNA chains by a bio-adhesive spreading vesicle [1]

This study is particularly motivated by the recent experiment [53], in which stained end-grafted DNA molecules about 20 μm long are scraped away and stretched out by the spreading front of a bio-adhesive vesicle. Tethered biotin ligands bind the vesicle bilayer to a streptavidin substrate, stapling the DNAs into frozen confinement paths. We performed quantitative image analysis of the stapled DNA which gives access, within optical resolution, to the local stretching values of individual DNA molecules swept by the spreading front. This significantly provides evidence of self-entanglements by revealing the chain internal friction and topological complexity.

3.1 Experimental background

When a bio-adhesive phospholipid vesicle is brought into contact with a surface coated with end-grafted λ-phage DNAs, the spreading front of the adhesive patch [108] propagates outwards from a nucleation center, acting as a scraper that strongly stretches the DNA chains. Moreover, the multiple bonds created during vesicle spreading effectively staple the stretched chains in the gap between the membrane and the substrate, confining the DNA chains in a tunnel-like channel as depicted in Fig. 3.2. The chain configuration starts thus at its fixed

[1] This chapter presents results published in *Phys. Rev. Lett.* **105**, 088101 (2010)

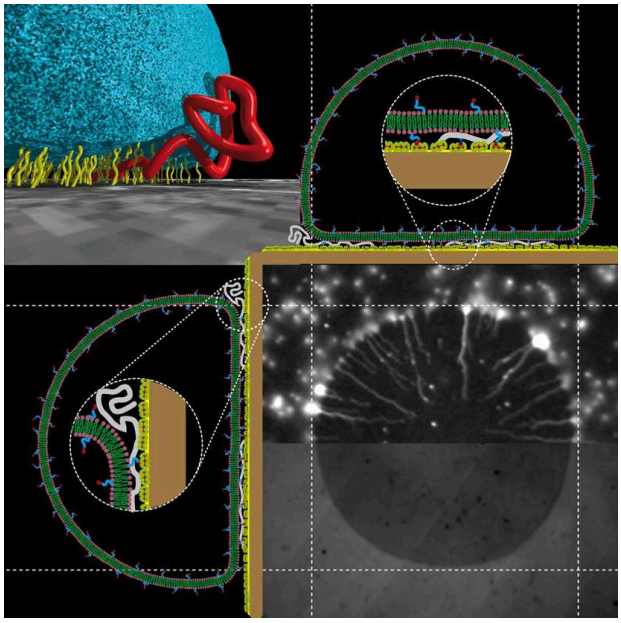

Figure 3.1: The top left image shows schematically the confinement geometry of the DNAs analyzed. A phospholipid giant unilamellar vesicle is attached to a substrate by short polymer anchors. The spreading of this attachment region scraps the end-grafted DNA molecule, stretching and stapling it between the membrane and the substrate as the adhesion front advances. The bottom right image combines in a janus display i) a typical optical fluorescence image where the stretched DNAs are seen as bright lines and the coiled DNA regions as bright light spots; ii) a typical RICM image where the adhesion patch appears as a darker disk. The bottom left and top right drawings further show typical features of the confined geometry.

end-grafted point at the streptavidin substrate. This surface-attached protein layer of receptors strongly binds the tethered biotin ligands carried by some of the bilayer phospholipids. From its grafted end, the chain meanders through the forest of short polymer tethers that connect the phospholipid membrane above the chain to the protein bed below it, eventually exiting the adhesive gap to adopt a coil-like configuration in the corner between the almost vertical vesicle wall and the horizontal protein surface.

A more detailed description on experimental methods and materials can be found in Ref. [53]. Briefly, the vesicles are prepared by electroformation, from a mixture of two lipids (Avanti Polar Lipids): 1,2-dioleoyl-sn-glycero-3-phosphocholine (DOPC) and 1,2-distearoyl-sn-glycero-3-phosphoethanolamine-N-(biotinyl(polyethylene glycol)2000) (DSPE-PEG2000-biotin) in different ratios. The biotinilated lipids allow the vesicles to strongly bind to a glass substrate

covered with streptavidin, which also anchor biotinilated λ-phage DNAs, with average end-grafting density of $1/(5\mu\text{m}^2)$, well below the surface overlapping concentration.

The conformations of the individual grafted DNA molecules were observed by fluorescence microscopy, the λ-DNAs being stained with YOYO-1 (Molecular Probes), as shown in Fig. 3.1 and Fig. 3.2(a). The localization and extension of the adhesive patch were determined by Reflection Interference Contrast Microscopy (RICM), see Fig. 3.1. A typical DNA image consists of a bright head part located outside the adhesive patch region and of a tail located inside. The whole conformation can also be located under the adhered membrane without a bright head. We distinguish between headed and non-headed conformations and name them *tadpoles* and *tapeworms*, respectively, see Fig. 3.3. Conformational relaxation is never observed throughout the experimental time, and DNA configurations remain as produced by the spreading and stapling process.

3.2 Image analysis

Figure 3.2 illustrates the conformational analysis performed from each DNA fluorescence image. The pixel size corresponds to 0.18 μm, thus fully stretched λ -phage DNA with contour length $S = 19.8$ μm would span 110 pixels[2]. Since one phospholipid occupies a cross-sectional area of 0.75 nm^2, a fraction n of biotinilated phospholipids corresponds to a ligand surface density $\sigma = 1.33\ n$ nm^{-2}. We have analyzed over 200 images of DNA obtained for various values of ligand fractions $n = 1/25,\ 1/50,\ 1/500$ and $1/5000$ corresponding respectively to $\sigma = 5.33 \times 10^{-2},\ 2.66 \times 10^{-2},\ 2.66 \times 10^{-3}$ and 2.66×10^{-4} nm^{-2}. After extracting a single DNA image from the fluorescence images, we first subtract the grey level of the background to obtain 3-dimensional representations of the intensity as shown in Fig. 3.2(b). After rotation each DNA image provides the intensity distribution $I(x, z)$ as displayed in Fig. 3.2(c). The cross-sectional distribution, i.e the distribution in the direction orthogonal to z, is measured to be Gaussian. For most tailed configurations the width of the Gaussian distribution $w(z)$ is almost constant along the z-direction, as shown in the inset of Fig. 3.2(d) and the height of the distribution $I_{\max}(z)$ is hence proportional to the cross-sectional intensity. The height of the intensity profile $I_{\max}(z)$ along the z-direction is shown in Fig. 3.2(d) together with a typical Gaussian cross-section.

[2]We excluded configurations when the total intensity was considerably different from the most probable value ($\sim$ 15%), thus avoiding error sources related to unusual DNA segments such as broken ones.

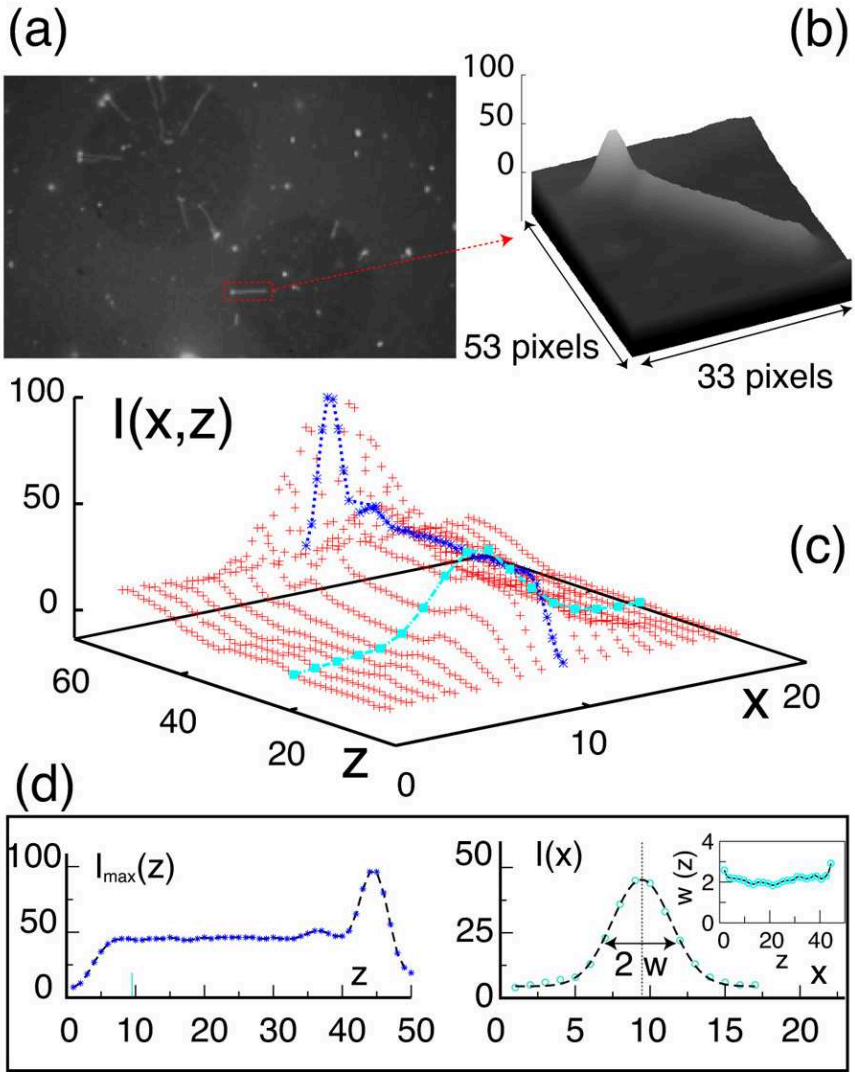

Figure 3.2: (a) A typical DNA fluorescence image and (b) a 3-d intensity representation of a single DNA cropped from the image. (c) The cross-sectional areas are fitted by Gaussian distribution and the peak of each Gaussian distribution is marked by dark blue star. (d) Intensity profiles of a single DNA image along the longitudinal direction (left) and cross-sectional distribution (right).

Assuming an homogeneous random distribution of fluorophores along the DNA backbone, one expects the intensity of each pixel $I(x,z)$ to be proportional to the DNA length it stores. After normalization with the total intensity $I_t = \sum_{x,z} I(x,z)$ of monodisperse DNAs, the reduced intensity $i(x,z) = I(x,z)/I_t$ can be interpreted as the fraction of the DNA segments located in the pixel. The normalized cross-sectional intensity can be defined as

$$m(z) = \left[\sum_x i(x,z)\right] \times (\text{DNA contour length in pixels}) - 1, \tag{3.1}$$

which is measured at a distance z away from the grafting position giving the relative excess length of DNA along z. The total contour length of DNA is about 110 pixels. For fully stretched DNA, it is a value of $m = 0$.

The insets in Fig. 3.3(b) exhibit conformations and typical profiles of the relative excess length $m(z)$ for tadpoles and tapeworms at ligand fractions $n = 1/50$ corresponding to an obstacle density $\sigma = 2.66 \times 10^{-2}$ nm^{-2}. As expected for tadpoles, the m values are sharply peaked at the edge of the membrane due to the fluctuating coil. The confined part of a tadpole, the tail, has small $m(z)$ values and is hence stretched. Significantly, tapeworms are less stretched than tadpoles and exhibit a much larger dispersion in stretching values. The mean plateau height $\bar{m}$ for each DNA is defined for each intensity profile. For various values of ligand fractions n, we obtained mean values $\langle m \rangle$ by averaging plateau heights $\bar{m}$ of up to 10 chains. Figure 3.3(b) shows dependence of $\langle m \rangle$ on the binders density n for both tapeworms and tadpoles, providing a quantitative measure for the differences in stretching between both configurations. We also measured mean-square average values $\langle \delta m^2 \rangle = \langle (m(z) - \bar{m})^2 \rangle$ by averaging first over the chain extension and then over different chains. Standard deviations $\langle \delta m^2 \rangle^{1/2}$ range for the tadpoles from 0.4 at the highest ligand densities to 0.7 for the lowest, while the corresponding tapeworm values are roughly twice as large in the corresponding range $[0.7 - 1.3]$. We now confront results from our local conformational analysis with theoretical predictions for confined semi-flexible worm-like chains.

3.3 Model and theories

The scraping and stapling process stretches the DNA and freezes in its tunnel primitive path. The tunnel has two-dimensional (z,x) shape confining the chain. In the vertical direction y,

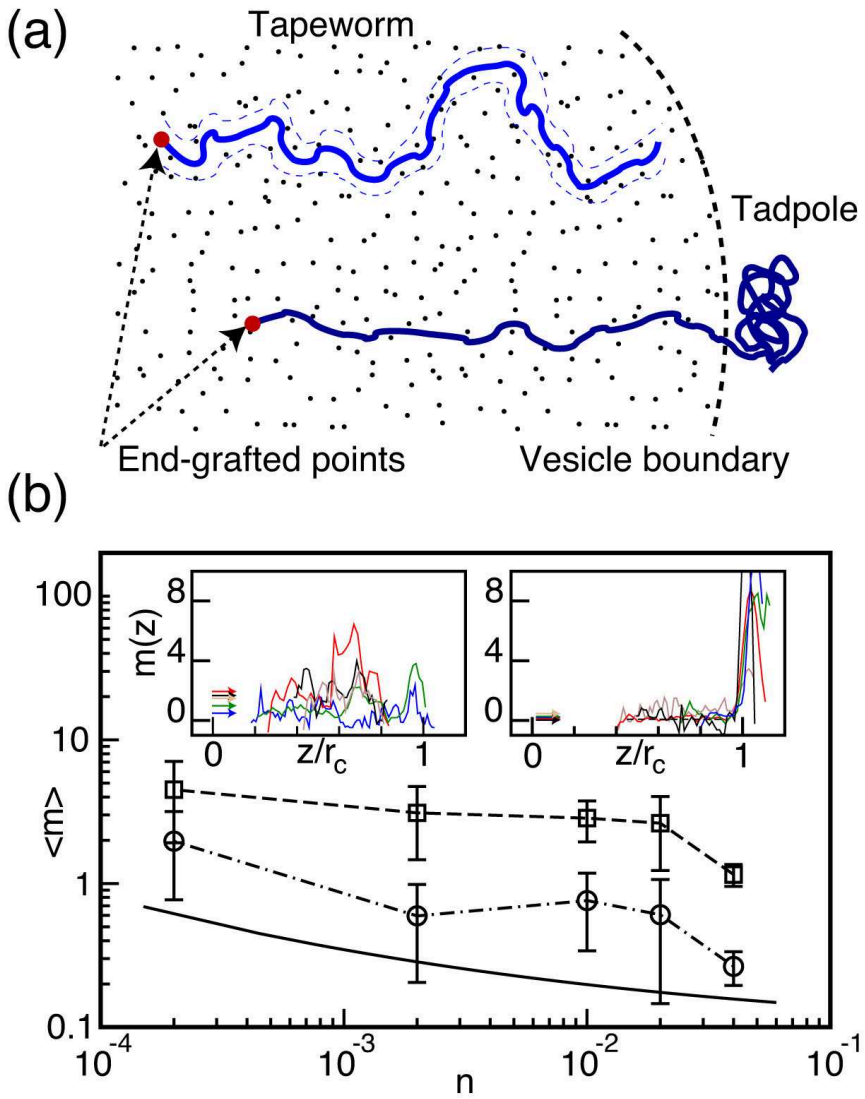

Figure 3.3: (a) Illustration of the conformations of a *tapeworm* (a DNA chain fully confined below the membrane) and a *tadpole* (a DNA chain having only a fraction of its length, the tail, confined below the membrane, while the rest of the chain, the head, is in a coiled configuration outside the adhesive patch.) (b) Typical profiles of the relative excess length $m(z)$ of tapeworms and tadpoles are shown in the left and right insets, respectively, at ligand fraction $n = 1/50$. The average values $\bar{m}$ of the plateau heights are there indicated by arrows, and z is rescaled by the membrane radius r_c. The curves in the figure show $\langle m \rangle$ (an average of $\bar{m}$ values of up to ten chains) as a function of the ligand fraction n for i) tapeworms (dashed line) and ii) tadpoles (dot dashed line). The continuous line shows theoretical predictions for semi-flexible chains in a confinement tunnel (See Eq. 3.3 and text thereafter). Clearly, confinement effects alone cannot explain the data, which demonstrates the existence of a longer sub-optical primitive path for the confining tunnel.

the tunnel size is determined by the distance h between the membrane and the substrate, with roughly $h \simeq 10$ nm as estimated from RICM. In the direction x parallel to the plane the tunnel size d is defined by the distance between multiple bonds connecting the membrane to the substrate $d \simeq \sigma^{-1/2} = 0.9\ n^{-1/2}$ nm. One has $d \simeq 5$ nm for the densest binding with n=1/25 and $d \simeq 60$ nm for the loosest with n=1/5000.

At the end of the spreading process, the chain can relax within its tunnel where it is still expected to display confined thermal fluctuations. Given the sub-optical nature of the tunnel dimensions h and d, such thermally induced fluctuations, easily seen in the coil head of the tadpoles, cannot be observed neither for the tapeworms nor for the tail sections of the tadpoles. Also, escape from the primitive path tunnels was never observed, consistent with typical distances d between binders smaller than the DNA persistence length $\ell_p \simeq 70$ nm, $0.07 < d/\ell_p < 0.90$. Note that the shape of the tunnel primitive path can only be experimentally determined up to the optical resolution, hence significant undulations can still be present even within a frozen, optically straight path. Confined thermal fluctuations and sub-optical waviness of the primitive path provide thus two possible sources for accounting for the DNA length storage, which is measured by the $m > 0$ values of the relative excess length. Small local entanglements resilient to unwinding during scraping provide a third possible storage source for the relative excess length that we will extensively discuss in this chapter.

3.3.1 Worm like chain confined by a harmonic potential

Here, we consider a confined semi-flexible chain of length S with persistence length l_p by the harmonic potential to vertical and lateral direction. The dimensions are $(h, d) \ll \ell_p$ for each direction, where the chain is stretched by force f. As studied in Chap. 2, the Hamiltonian is written in Fourier space as

$$H = \frac{S}{2}\sum_q \left(k_B T \ell_p q^4 + f q^2 + \kappa_{h,x}\right) x_q x_{-q} + \frac{S}{2}\sum_q \left(k_B T \ell_p q^4 + f q^2 + \kappa_{h,y}\right) y_q y_{-q}, \qquad (3.2)$$

where the chain is described by the parametric representation $x(z)$, $y(z)$ along the longitudinal direction of DNA and its Fourier transforms x_q, y_q. For each direction, we introduced the different amplitude of harmonic potential as $\kappa_{h,x}$, $\kappa_{h,y}$. The mean square amplitudes are saturated in each dimension as $\langle x^2 \rangle = d^2$ and $\langle y^2 \rangle = h^2$ at zero force. Using Eq. 2.21 with fixed two

amplitudes, the average of the relative excess length is calculated as

$$1-\frac{\langle L\rangle}{S}=\frac{1}{4}\left(\left[\frac{\ell_p}{d}\right]^{\frac{4}{3}}+\tilde{f}\right)^{-\frac{1}{2}}+\frac{1}{4}\left(\left[\frac{\ell_p}{h}\right]^{\frac{4}{3}}+\tilde{f}\right)^{-\frac{1}{2}}, \tag{3.3}$$

where $\langle L\rangle$ is the average projected length of the chain measured along the tunnel and $\tilde{f}=f\ell_p/(k_{\mathrm{B}}T)$ is the value of the force in its natural units $k_BT/\ell_p=0.06$ pN for $l_p=70$ nm. Relating Eq. 3.3 with the analysis, the relative excess length is estimated as $1-\langle L\rangle/S=\langle m\rangle/(1+\langle m\rangle)$. At zero force, one gets $0.1<\langle m\rangle<0.5$ for $2\times10^{-4}<n<4\times10^{-2}$. Clearly, the excess length stored in the thermal fluctuations cannot account for excess length values up to $\langle m\rangle=4$ as observed from the experiments as seen in Fig. 3.3. This implies that the actual confining tunnel follows a longer wiggled sub-optical primitive path.

The shape of the primitive path is determined by the pinning process occurring at the adhesive front, it thus reflects the conformation of the DNA chains at the junction between the tunnel under obstacles formation and the free coil head. The spreading process applies a force to the coiled head by a combination of hydrodynamic stresses and direct membrane-DNA interactions, which induces the average stretching state captured by the stapling mechanism. In this case, therefore, the relevant force extension relationship does not depend on the confinement. An interpolation formula that accounts both for the strong stretching regime described by the limit of zero confinement in Eq 3.3 and for the weak stretching limit where the extension is determined by the linear response of the fluctuating coil can be written as [92]:

$$\tilde{f}=\frac{\langle z\rangle}{S}+\frac{1}{4\left(1-\langle z\rangle/S\right)^2}+\frac{1}{4}, \tag{3.4}$$

where $\langle z\rangle$ is the average projected length.

Using Eq. 3.4 with $\langle m\rangle=S/\langle z\rangle-1$, force values are obtained in the range $0.85<\tilde{f}<15$ for the tadpole conformations and $0.35<\tilde{f}<1.3$ for the tapeworms. Note that forces of order $\tilde{f}\simeq1$ or $f\simeq k_{\mathrm{B}}T/\ell_p=0.06$ pN are expected from the entropic repulsion between a wall and a polymer, larger forces must be related to different effects like the hydrodynamic stresses generated by the strong shear region in the immediate vicinity of the advancing front. Estimates based on the observed maximum velocity $v=10$ μm s^{-1} [53] and a gap height h of order of 10 nm lead to a shear rate $\dot{\gamma}=vh\sim10^3$ s^{-1} which can easily account for the highest observed stretching values. However, observed spreading processes are smooth, the

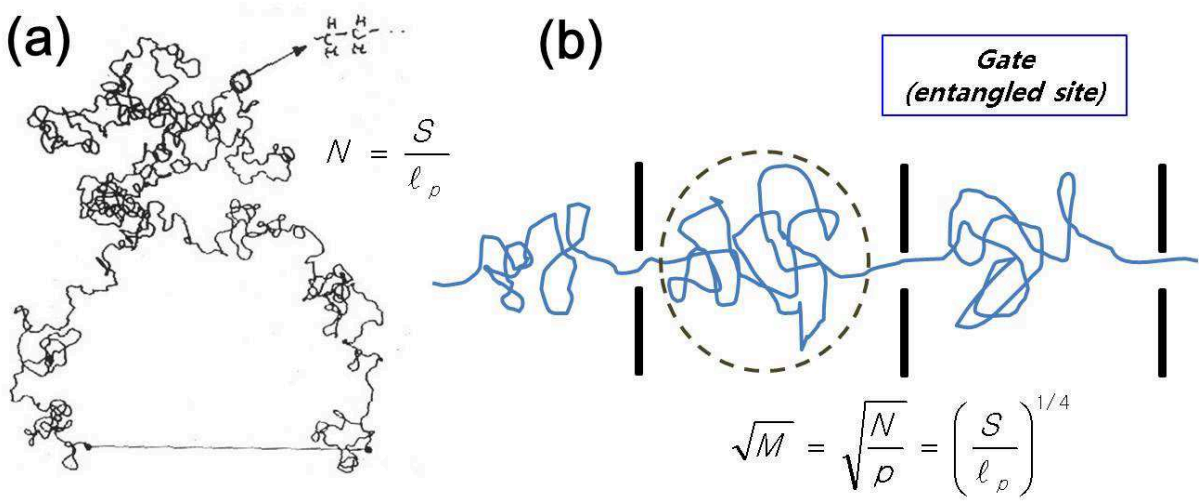

Figure 3.4: Schematic description on self-entanglement effect and its gate model. (a) A long Gaussian chain of length S and l_p is expected to have average number of monomers $N = S/l_p$. (b) The relaxation of unwinding the self-entanglement is depicted in the gate theory, where a gate corresponds to a knot (See the text for details).

velocity measured from the spreading front decreases linearly from the initial nucleation site to the final maximum adhesion patch radius. The measured differences of stretching behaviour between the tapeworms and the tadpoles can thus only be accounted for by additional friction sources, we argue in the following that they are caused by internal friction forces related to self-entanglements.

3.3.2 Self-entanglement of the DNA

As an additional frictional source, we consider a self-entanglement of the DNA, which means a configuration of the chain that acts like a gate [109, 110] through which the unwinding coil needs to be threaded for relaxation. By studying the relaxation process, especially, we try to account for the different internal structure of a DNA. In the absence of self-entanglements, the scraping mechanisms can only induce a modification of the chain configuration from a coil to an open and extended shape, provided that the largest relaxation time for chain is smaller than the characteristic time of vesicle spreading. The longest relaxation time simply scales as $\tau \sim R^2/\mu \sim R^2\zeta$, where the mobility is given by $\mu = k_{\mathrm{B}}T/\zeta$ with friction coefficient ζ. For the

chain without self-entanglements, the longest relaxation time is described by Zimm dynamics. The Zimm relaxation time is then obtained as $\tau_Z \sim N^{3/2}$ with $R \sim N^{1/2}$ and $\zeta \sim N^{1/2}$. From the experiment, we can convert this into real time in order to compare with vesicle spreading velocity. For a coil of radius $R \sim 1$ μm and water viscosity $\eta = 10^{-3}$ Pa·s, and associated friction ζ is given by the Stokes friction $\zeta \sim \eta R$. The longest Zimm relaxation time is estimated as $\tau_Z \sim R^2\zeta/(k_{\rm B}T) = \eta R^3/(k_{\rm B}T) = 0.2$ s which is smaller than the vesicle spreading time $\tau_S \sim 10$ s observed from the experiment.

In the presence of p self-entanglements, on the other hand, the chain relaxation time can be simply estimated from p and ζ_1, where ζ_1 is the local friction from a gate due to local contacts and is arguably higher than hydrodynamic friction. For the experimental conditions described here, the DNA chain can be pictured as a Gaussian chain with $N = S/\ell_p \sim 300$ monomers of size ℓ_p as shown in Fig. 3.4. Considering thus Gaussian statistics, the averaged number of self-entanglements p, involving monomers distant along the chain, is expected to be given by $p = \sqrt{S/\ell_p}$ and the number of monomers M in a polymer strand between two gates by $M = N/p = \sqrt{S/\ell_p}$. The friction from one gate ζ_g is therefore $\zeta_g = \sqrt{M}\zeta_1$ and the total friction estimated by this model reads $\zeta = p\zeta_g = (S/l_p)^{3/4}\zeta_1$. As a consequence, the relaxation time τ_E that takes the chain to relax self-entanglements is estimated as $\tau_E \sim R^2\zeta \sim N^2 N^{3/4} = N^{11/4}$, which is larger at least by three orders of magnitude where the power of N is only compared[3]. than the Zimm time estimated above as $\tau_{\rm Z} \sim N^{3/2}$.

3.4 Conclusion

The fundamental differences in our experiments between tadpole and tapeworm configurations, observed under the same vesicle, can be fully understood by invoking such long self-entanglement relaxations. Upon scraping, a chain with no self-entanglements in the polymer section that undergoes unwinding can be pushed to the border of the adhesive patch in a smooth manner, leading to a tadpole configuration. If the spreading membrane comes across one self-entanglement during the scraping process, it will locally stretch the chain but eventually will roll over it letting behind the excess of chain contour length that was not able to unwind. This corresponds to the tapeworms configurations that are confined below the adhesion patch and display large

[3]Considering the power of N alone as $N^{3/2}$ and $N^{11/4}$, the later is longer by three orders of magnitude. Since the topological constraint is less important than that in the melt, the prefactor of $N^{11/4}$ must be small. Still $\tau_{\rm E}$ must be longer than $\tau_{\rm Z}$.

stretching fluctuations. Note that heterogeneities in the spatial distribution of the binders cannot account for the observed stretching variations. The existence of self-entanglements in polymer chains has been theoretically conjectured for more than two decades within the framework of Renormalization Group theory computing statistics of contacts between two Gaussian chains [64] and of mutual entanglements[4] [63]. In spite of the importance of self-entanglements for understanding polymer chain dynamics, these theories have never been put to test, because of the intrinsic difficulty of demonstrating the presence of such chain configurations [111]. We have shown here that the scraping and stapling of an end-grafted DNA chain by the spreading front of a bio-adhesive vesicle provide an unique experimental geometry sensitive to long relaxation processes as those expected from self-entanglements.

[4]The exponent Z is defined from $\tau_E \sim N^Z$. While our simple argument suggests $Z = 11/4$ the more sophisticated calculations lead to $Z \approx 3$. There is a finite probability P_0 for two half-chains not to intersect at all $P_0 \propto N^{-5/16}$ (to second order in $\epsilon = 4 - d$ where $d = 3$) [64]

Chapter 4

Observation of cooperative conformational change of microtubules

In this chapter, we investigate the dynamics and mechanical properties of MTs by observation of image data obtained from experiment. The image contains the fluorescently labelled MTs fluctuating in a thin geometry (between two glass slides), in which they display a distinctive thermal motion and shapes certainly different from those of a simple WLC model. One of notable observations is the presence of a coherent sinusoid wavy shape of MTs under confinement. Acknowledging the importance of wavy shape, we first investigate the properties of this higher order structure and find an interesting relation between the helical radius and its wavelength. In addition to characterizing static feature of this helical superstructure, we present several types of conformational changes in MTs shape. We show that the conformational transitions, which can be easily detected in fluorescence microscopy, are highly correlated over the whole MT contour length. By using a quantitative MT contour fitting analysis, the transitions are directly measured as in-plane curvature evolution over time. The very high cross-correlation coefficients of distant segments curvatures reveal the evidence for very high cooperativity of the observed conformational transitions. Such a high degree of cooperativity is consistent with the recently formulated hypothesis of mechanical multistability of the MTs tubulin dimer's structure, in which at least two discrete curvature states are most likely observed under the experimental conditions investigated here. Finally, by observing the partially attached MTs, we measure the controversial persistence length for a clamped MTs. In particular, we show that the position-dependent lateral fluctuations along the MT lead to apparent length-dependence

of the persistence length.

4.1 Introduction

Polymorphic transitions are found everywhere in nature from the simplest bacterial biofilaments to most complex organisms. The term polymorphism refers here to the ability of the constituent units (monomers) to switch between two or more conformational states. Through inter-unit mechanical coupling the behaviour of a lattice of polymorphic units can become highly cooperatively organized in rather complex manners. In the bacterial flagellum, environmental perturbations can trigger sudden cooperative polymorphic transitions between helical states with different pitches and handedness [112]. Another remarkable instance of polymorphic transition is the tail sheath contraction of a T4 bacteriophage [113]. An active ATP-driven polymorphic transition is also found in nature, for instance during the rotary transformation of the helical sheath in Spiroplasma [114]. Polymorphic filament motifs can also be found in the cytoskeleton in eukaryotic cells: actin-rings undergoing a light-induced conformational transition and supercoiling [115] were observed, as well as taxol-stabilized microtubules forming unusual superhelical structures [4]. Tubulin conformational multistability appeared as an indispensable ingredient for an explanation attempt of the helical shapes [116].

In this chapter, we present new observations on fluorescently labelled taxol-stabilized MTs placed in a thin chamber. Tracing the MT's contours, we find that they displays wavy shapes of micron size of wavelength and radius. Typical geometrical characteristics are of helical filaments confined in 2D. Comparison between the experimental data and the theory of confined helices, so-called squeelices, allow us to go back to the three dimensional native bending and torsional properties of the helical MT. Most notable finding is that the MTs undergo highly cooperative conformational transitions in a discrete and spontaneous way, which is manifested by time-traced mean curvature of non-overlapping regions.

We observe two kind of conformational transitions: correlated curvature reorientations (we call as curvature flipping) and curvature magnitude transitions corresponding to transformations from curved to straight shapes (and vice versa). These conformational transitions show a high degree of cooperativity corroborated by correlation coefficient between adjacent arcs showing switching. Permanent switching of the tubulin dimers between straight-curved state and cooperative interactions along the protofilaments axis were hypothesized as a basic ingredient of

the theoretical model proposed in [116]. This polymorphic MT model predicts a degeneracy of the superhelical ground state and thus a permanently but coherently MT reshaping with an evolving reference ground-state configuration, due to thermal fluctuations. We provide also new measures of the persistence length versus the MT's length which displays a non-monotonic, oscillatory behavior around a nearly linearly growing average in qualitative agreement with the theory of polymorphic tube model [116].

Our observations provide evidence that MTs are not simple semi-flexible chains or Euler beams, but highly complex supramolecular structures whose basic elements can switch and interact, giving rise to very complex large scale transformations. If these properties of MTs persist *in vivo* (without taxol agent), the most inherent and distinct consequence of the underlying mechanism lies in the possibility of signal transmission along the contour via a long-range conformational switch.

4.2 Experiment and MTs contour fitting routine

4.2.1 Sample preparation

Tubulin was purified, taxol stabilized, mixed with a small amount (1%) of rhodamine labelled tubulin and polymerized as described in Ref. [2]. A small quantity of the microtubule solution ($0.2 - 0.5\ \mu l$) was placed between two precleaned cover slides and immediately observed on a Nikon Te-2000E inverted microscope equipped with an 60X water immersed objective and a Hamamatsu Em-CCD camera.

The images we acquired are sequences of frames at video rate 33 frames per second with the time interval for each frame $1/33$ sec. Pixel size is $0.266\,\mu$m, and the typical MTs in the images has contour length ranging from few microns to several tenth of microns. The MTs are confined between two cover glasses with the thickness of layer less than $1\,\mu$m, which is comparable to previously reported value of helical radius of MTs $1 \sim 2\,\mu$m [4], where the MTs are slightly squeezed (depending on the variable height of the chamber size) in quasi-2d slab. Under the experimental conditions used and without special treatment of the glass surfaces, the microtubules occasionally tend to adsorb in the partial regions close to their ends while the largest portion of their contour remains free from attachment. This useful coincidence was employed to study also partially grafted MTs and allowed us to discriminate between trivial rotary motions of the filament and true conformational rearrangements.

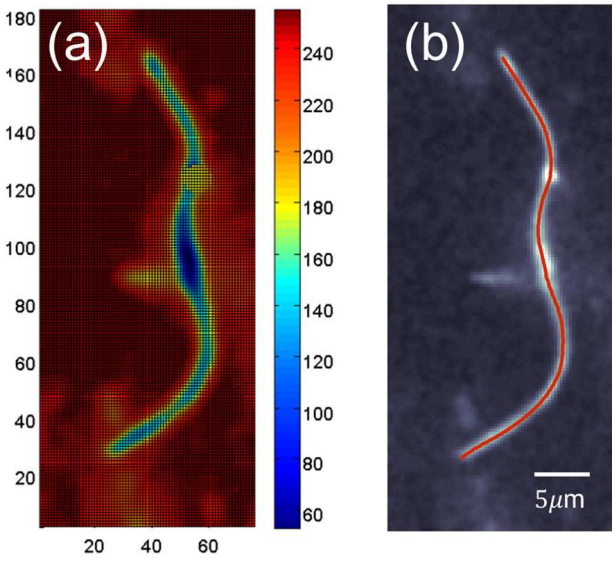

Figure 4.1: (a) Top view of inverse intensity landscape, where the image size is given by pixels and the color indicates the depth. (b) The fitted contour (shown in red) is superimposed onto corresponding image.

4.2.2 Filament tracing

As the MTs are in a quasi-2d geometry, we have digitalized and analyzed their projected 2d contours. The vertical displacement from focal plane of some MTs displays strong variations which is seen as non-uniform intensity along the contour, but the majority of MTs investigated was flat enough to be analyzed with a simple 2d contour algorithm.

For the contour fitting, we basically use two different methods to handle the image data and to extract the MTs contour. The first is a custom ImageJ plugin called JFilament [117]. These software are useful tools for editing the image data and extracting the MT contours automatically or semiautomatically. In particular, JFilament is used to make an initial guess to the MTs contour. For more refined contour fitting, we have developed our own custom fitting algorithm based on the Monte-Carlo method. In this algorithm, we simulated a stiff polymer fluctuating on the energy landscape which is phenomenologically created from the image as shown in Fig. 4.1(a). The total energy of confined chain consists of bending, link, and external potential (obtained from image), $E_{total} = E_{bend} + E_{link} + E_{ext}$. The chain has N monomers typically chosen as a spacing of $0.5 - 1$ pixel. Each monomer is connected by a FENE potential along the contour (See Chap. 2.4.1 for the formulas). The energy landscape is constructed by

the interpolated intensity at each inter-pixel location, in which the continuous energy map is made by interpolation as

$$E_{ext} = \frac{\frac{I_1}{d_1} + \frac{I_2}{d_2} + \frac{I_3}{d_3} + \frac{I_4}{d_4}}{\frac{1}{d_1} + \frac{1}{d_2} + \frac{1}{d_3} + \frac{1}{d_4}}, \tag{4.1}$$

where d_i is a distance from i-th vertex having intensity I_i. The simulated chain is subjected to the energy landscape, and fluctuating along the energy minimum path. The final configuration is time-averaged for several hundreds of chain configurations. Figure 4.1(b) shows an extracted contour superimposed onto the corresponding image. Time sequenced contours are obtained by the same procedure as above for each frame by using the previous frame contour as an initial guess for the next frame. In this algorithm, the chain length is fixed for all frames, so that it can cover the areas of weak intensity resulted from a temporary motion out of focal plane. By tuning the stiffness of chain, the fitting become robust and uninterrupted even in the regions where the intensity is locally irregularly dispersed by the other MTs.

4.3 Characterization of the MTs superhelical shapes

In our experiments, thermal fluctuations of taxol-stabilized MTs were recorded by video microscopy. In a typical experiment, a portion of MTs is fully adsorbed to the glass surface (and thus not fluctuating) likely due to the multivalent ion (Mg^{2+} is part of the buffer solution) mediated MT-glass surface interaction. However another portion of MTs (typically about 50-60% of them) exhibits both a surface fixed and a freely fluctuating part. We have also witnessed the process of desorption from the surface and vice versa adsorption. When MTs are fully adsorbed often irregular and random shapes are observed, possibly because they got quenched during the rapid adsorption process in non-equilibrium configurations.

Apart from this portion of random surface quenched states, we found that a free and sometimes adsorbed MTs exhibit a distinct wavy shape under the confinement. This seems to reflect a 3-dimensional superhelical structure. Such a large scale helical structure of MTs was already suggested by Venier et al. [4], but never fully characterized in literature. A number of MTs comprising distinct wavy shapes enables us to collect statistics and investigate the detailed features of the shapes. For 148 wavy shaped MTs, we have measured their apparent projected pitch and the radius of the superstructure. Figure 4.2 shows the MTs shapes and statistics of helical pitch P and radius R. In Fig. 4.2(a), we present the histogram of pitch, where we provide the

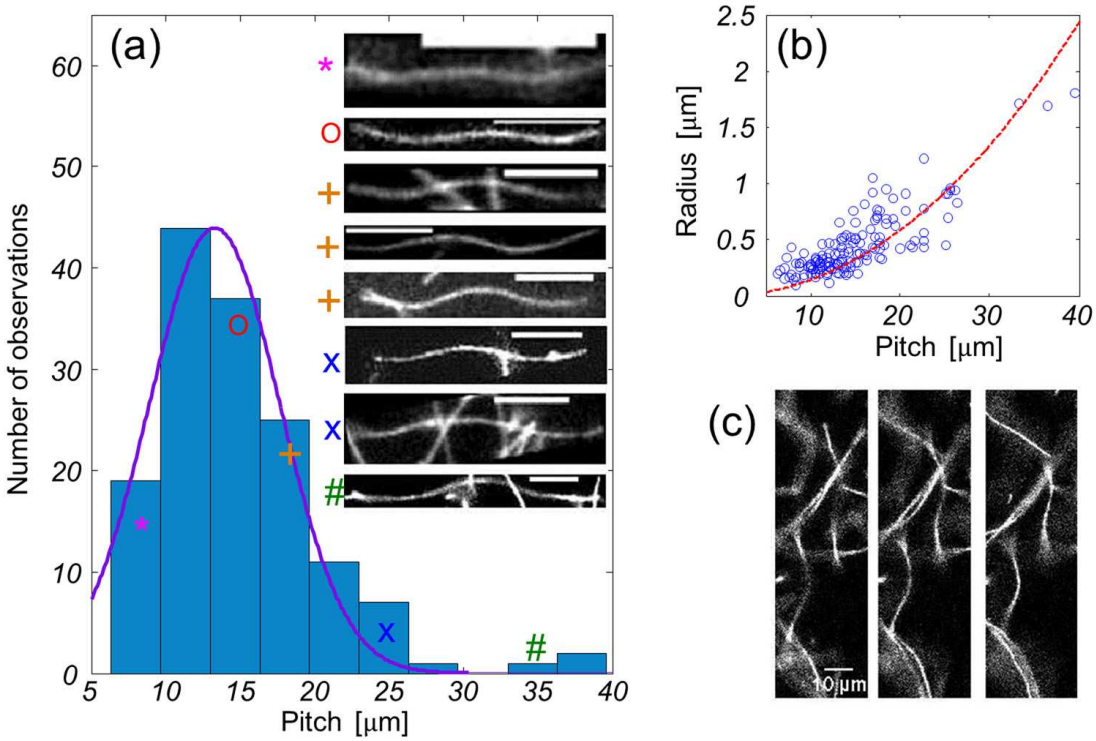

Figure 4.2: Helicity of MTs (a) The histgram of the pitch is plotted with the Gaussian fit of mean pitch:$13.27\,\mu$m and STD:$4.36\,\mu$m. The images in inset show typical wavy shape of a squeezed MTs, the scale bar is $10\,\mu$m for all images. The measured pitches for each MTs are denoted as the same symbol with those on the histogram. (b) The relation between pitch and radius is obtained from the individual MTs, data fit is done with the formula of a squeezed helix (See text for details). (c) Scanning of 3d stacks of the image, showing the right-handedness of the MTs. The height difference between each stack is $0.5\,\mu$m.

Gaussian fitting with the mean wavelength of about $13\,\mu$m and the standard deviation $4.36\,\mu$m. This value is close to the wavelength $15\,\mu$m of superhelical structure observed by Venier et al. [4]. Typical wavy shapes of squeezed MTs with various wavelengths are shown in inset of Fig. 4.2(a). For better view of the structure of the MTs of small wavelength, the images are scaled to the same size, but the scale bar still indicates the same length for all images. As shown in Fig. 4.2(b), typical amplitude R of the MTs varies with their wavelength. This dependency, although qualitatively different, was also observed for the bacterial flagella filament [112], and interpreted in terms of cooperative conformational transitions between between helical states with different R, P, and handedness. However, the failure to reproduce the MTs $P-R$ relation

with this classical Calladine polymorphic flagellin model fit [112, 118] indicates that the relation for MTs is qualitatively different.

To reproduce the observed correlation $P - R$, which is approximately parabolic in nature, we assumed a simple geometric model of a single (quasi 2-d squeezed) helical state with a constant lattice curvature ω_1 but a possibly variable pitch P. From simple geometry, by assuming that the shape is approximately made of a sequence of circular arcs, we can derive a relatively simple connection between the radius and pitch. Then geometrical analysis produces the relation $R = \frac{1}{\omega_1}(1 - \sqrt{1 - (\frac{\omega_1 P}{4})^2})$, which is used for data fitting in Fig. 4.2(b) (in red) with the best fitted radius of curvature $\omega_1^{-1} \approx 21\,\mu$m.

Another structural feature of the helix is its handedness. Although the handedness of the superstructure is believed to have something to do with a lattice type [116], it has not been documented yet. Due to the limitation of our 2d fluorescence optical method, and the large and rapid fluctuations of the MT shapes, it was not possible to give a definite statement on the handedness of the underlying structures. To approach the handedness problem which is intrinsically three dimensional, we have performed 3-d scans of the samples by moving of the automatic microscope stage of partially confined MTs. The recorded z-stacks were still too noisy to allow fully automatic 3d reconstruction. However a visual scan through the z-stack Fig. 4.2(c) indicated a right-handed structure. With only a limited number of samples that could be reliably treated in this manner, we can only cautiously state that the helices were right-handed but at this point cannot exclude the possibility of the existence of the other handedness as well.

4.4 Polymorphic dynamics of MTs

Our observation of helical MT states appears to support the hypothesis that MTs are a complex, possibly polymorhpic filaments. We then ask that such a polymorphic structure can switch its shape spontaneously as we know this from the bacterial flagella [112, 119]. Many observations are associated with some type of "frozen-in" curvature which is much larger than the fluctuations around the reported one in the literature [1, 120]. The origin of this frozen-in curvature becomes more clear in the observations from the previous chapter 4.3, where the MTs are in fact superhelically curved sturctures.

Our observations provide first evidence that the helical intrinsic curvature of MTs is not frozen but rather can undergo conformational transitions leading to large scale reshaping. An

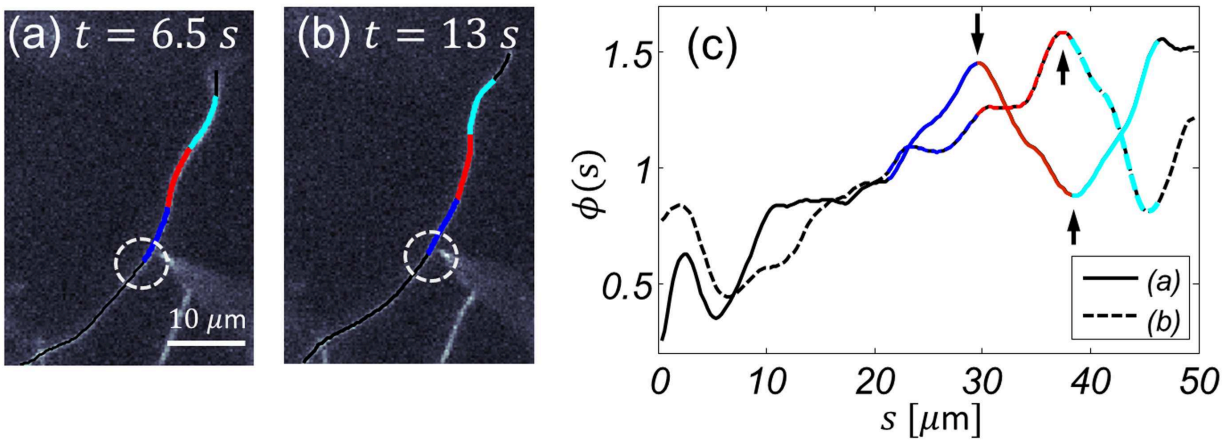

Figure 4.3: Two distinctive shape of MTs at different time (a) $t = 6.5\,\mathrm{s}$ (a) $t = 13\,\mathrm{s}$. (c) Tangent angle $\phi(s)$ plotted along arc-length s for MTs of (a) and (b), and arrow indicates the inflection point. The color code for each segment is same for three panels.

example for this behavior can be seen in Fig. 4.3, where we trace a single MT contour in time and the fitted contour is superimposed onto the corresponding image. For this MTs, the segments showing most significant motion are marked in different colors. Two segments in red and light blue of several microns flip their curvature in opposite direction to each other between time $t = 6.5\,\mathrm{s}$ and $t = 13\,\mathrm{s}$. For a quantitative analysis, we measured the tangent angle $\phi(s)$ along arc-length position s. Figure 4.3(c) shows tangent angle profiles for the same MTs at different time stage. At $t = 6.5\,\mathrm{s}$, the angle $\phi(s)$ varies linearly with s for three segments in different color, which means that those segments have constant curvature given by local curvature $\phi'(s)$. At later time $t = 13\,\mathrm{s}$, the segments in red and light blue remain in circular arcs, but the phase has inverted in their respective manner. For the section in dark blue, both the portion and curvature is decreased without phase flipping, which is likely because the conformational transition is slightly prevented by its proximity to the attachment region (dotted circle in while).

In order to quantify the cooperativity of transitions, we introduce mean curvature $\overline{\kappa}(\Delta s) = (\phi(s + \Delta s) - \phi(s))/\Delta s$ over a certain range of arc-section Δs and trace $\overline{\kappa}$ in time for non-overlapping regions of MTs. Based on the theoretical background on an usual WLC model, we do not expect any spacial correlation between curvatures over a distance of the persistence length. However, the MTs do display a clear time-correlation between segment curvatures many microns apart, which indicates the involvement of true conformational transition of the lattice.

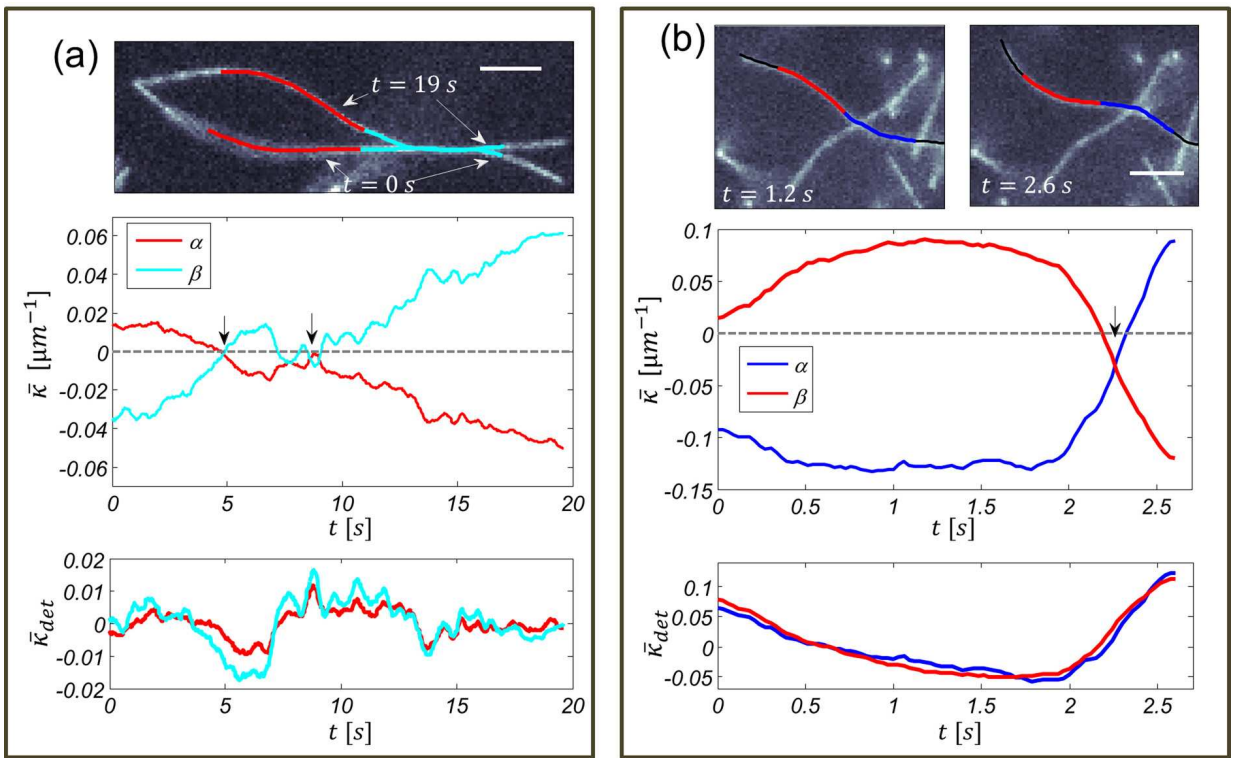

Figure 4.4: Highly cooperative MTs curvature reorientations: plot of $\overline{\kappa}$ and $\overline{\kappa}_{det}$ over non-overlapping arc-sections α and β. In both panels of (a) and (b): (Top) fitted contours of those sections are superimposed onto the image, (Middle) $\overline{\kappa}$ plotted with time for both sections α and β, and the arrow indicates the cross point of the curvature, (bottom) time-detrended curvature of those two sections. Scale bar is $5\,\mu$m. Correlation coefficient between two adjacent arc-sections are obtained as (a) $r_{\alpha,\beta} = 0.9936$ and (b) $r_{\alpha,\beta} = 0.9786$.

Figure 4.4 shows some examples of highly cooperative MTs curvature reorientations. These phase flipping are seen as strongly correlated motion along the contour. Each arc-section is chosen from the tangent angle profiles as described above. For both MTs of Fig. 4.4, a clear crossover in mean curvature is found as indicated by arrows. As shown in the middle graph of Fig. 4.4(a), the first crossover at $\overline{\kappa} = 0$ indicates the MTs in straight shape at $t = 5\,$s, subsequently fluctuating for few seconds, and flipped over after second crossover at about $t \approx 9\,$s. This indicates that two sections do not evolve independently but in a very cooperative manner, which is confirmed by time-detrended[1] mean curvature $\overline{\kappa}_{det}$ (shown in the bottom

[1]Detrend removes a linear trend from a data set by subtracting the straight line which is best linear fit for

of Fig. 4.4). From the detrended mean curvature, the motion of two sections indices α and β of MT in Fig. 4.4(a) appears as highly synchronized displaying the correlation coefficient[2] $r_{\alpha,\beta} = 0.9936$. For the MTs in Fig. 4.4(b), the two selected sections are oriented inversely with constant curvatures before the transition. This is typical feature of the squeezed helical state. The transition takes place at about $t = 2.3\,\mathrm{s}$, the mean curvature for two sections is $\overline{\kappa} < 0$ at the crossover. Therefore, the segment β (in red) becomes straight before segment α (in blue) whose flipping motion is slightly delayed. Nonetheless, both the detrended mean curvature analysis and the correlation coefficient of $r_{\alpha,\beta} = 0.9786$ indicate high degree of cooperativity.

In the previous examples one could to some extent object that some type of (although unlikely) secondary effects could lead to a rotation of the whole filament despite visible surface adsorption and give rise to the observed correlations. However, there is another more clear class of transitions that cannot be associated with such rotation effects. It involves conformational changes from a curved to straight state and vice versa as shown in Fig 4.5. In the time course of such transition, the entire filament is visibly in the focal plane without intensity variations (within < 0.5 micron) implying that no spacial rotation could account for the effect.

For the MTs in Fig. 4.5(a), one can easily see that only partial segments are involved in the conformational transition. Most interestingly arc-sections of δ and ϵ show the transformation from curved into straight occurring very quickly less than $1\,\mathrm{s}$ and simultaneously. Indeed, these two sections are initially arranged inversely with the same magnitude of curvature. Starting from that initial configuration, the curvature of these two sections are evolving in synchrony to a value close to zero (straight state). The detrended mean curvature also reveals the strong correlation between these adjacent arc-sections. On the other hand, other sections of α, β, and γ stay in the almost same circular shapes likely because they are strongly adsorbed. On the other hand, Figure 4.5(b) present the MTs undergoing the opposite conformational transition from straight to curved. The two selected sections α (in red) and β (in blue) keep building up opposite curvature in a correlated manner, eventually reaches a constant curvature. Interestingly these transitions and the coexistence of helical and straight states were predicted by a theoretical

the data set. In forecasting models, the process of removing the effects of accumulating data set from a trend to show only the absolute changes in values and to allow potential cyclical patterns to be identified. In our work, detrended is used to investigate the correlation by comparing the absolute changes of curvature in time for two different arc-sections.

[2]For a set of N data points (x_i, y_i), the correlation coefficient is given by $r_{x,y} = C_{xy}/\sqrt{C_{xx}C_{yy}}$, where the quantities in the right part are unnormalized variance and covariance as $C_{xx} = N\mathrm{var}(x)$, $C_{yy} = N\mathrm{var}(y)$, and $C_{xy} = N\mathrm{cov}(x, y)$. In our analysis, $r_{\alpha,\beta}$ is calculated for a set of the mean curvature in time for two distant arc-sections $(\overline{\kappa}_\alpha(t), \overline{\kappa}_\beta(t))$.

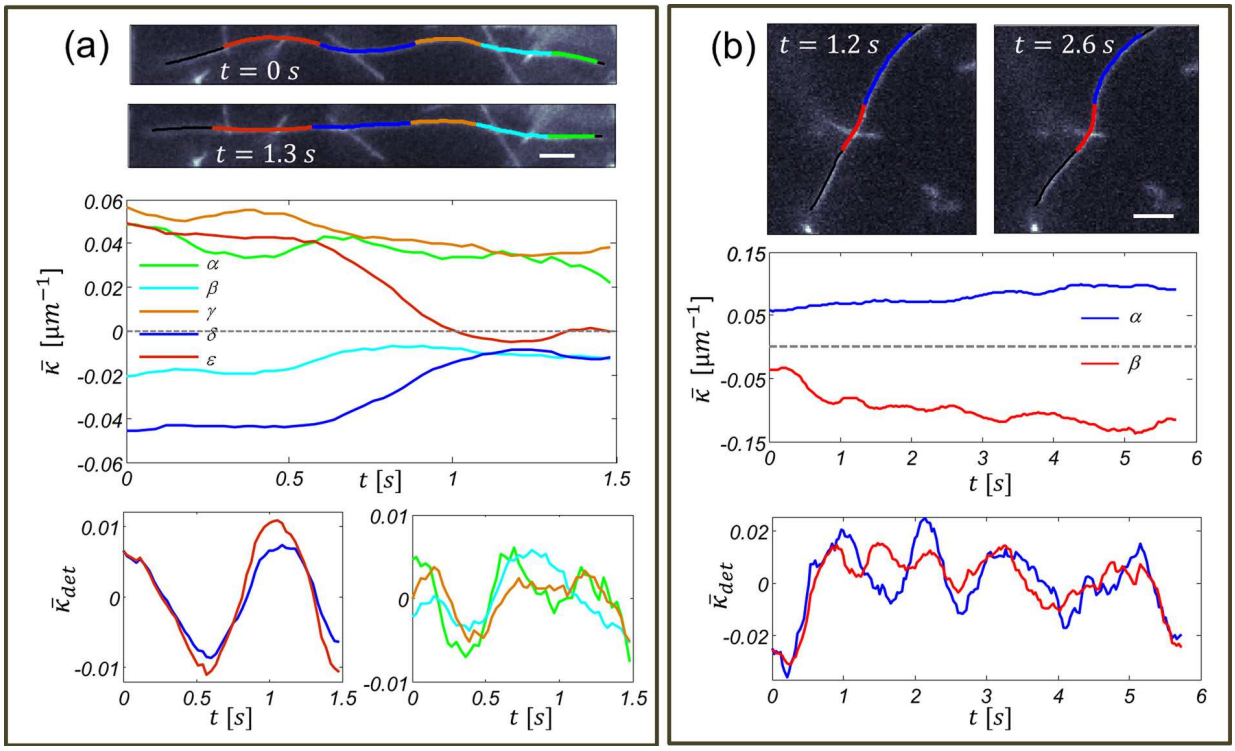

Figure 4.5: Highly cooperative MTs curvature magnitude transitions. (top) The contours of several non-overlapping segments superimposed onto the image. (middle) $\overline{\kappa}$ is traced with time for each sections. (bottom) $\overline{\kappa}_{det}$ of those two sections. The color code is same as in above images. Scale bar is $5\,\mu$m. Correlation coefficient between two arc-sections are obtained as (a) $r_{\epsilon,\delta} = 0.9967$, $r_{\delta,\gamma} = 0.9582$, $r_{\gamma,\beta} = 0.8108$, and $r_{\beta,\alpha} = 0.3002$ (b) $r_{\alpha,\beta} = 0.9072$.

model [116]. Depending on the microscopic elastic and energetic parameters involved (like the free energy of monomer transition from straight to curved) the model predicts that either state (curved or straight) or even both of them can represent local free energy minima.

4.5 Length-dependent stiffness of clamped MTs

As seen in previous chapter MTs display a non-trivial superhelical shape that can dynamically rearrange in time. At this point, in the light of our observations, it is interesting to revisit the classical yet controversial question of MT's persistence length $l_p = B/k_BT$ (with the bending stiffness $B \propto E$ proportional to MTs Young modulus E). As shown by Pampaloni et al. [2]

and Taute et al. [3], clamped MTs seem to exhibit anomalous fluctuations in the direction lateral to the MT axis for a wide range of contour lengths from $2\,\mu$m to $65\,\mu$m. Besides these experiments, there has been many experimental attempts to estimate E of a stabilized MTs by chemical agents *in vitro* [4, 121–125], where the measured values do not show quantitive consistence and typically range from $E = 100\,$MPa to $1.9\,$GPa. Based on that observation, it is hypothesized that some important piece of information about MTs is still missing to understand the results. In this work, we will investigate how the polymorphic dynamics documented above gives rise to an effective length-dependent persistence length $l_p = l_p\,(s)$, where s is the distance to the MT's attachment point. In order to draw closest analogy and to allow comparison with existing experiments [2, 3], we focus our analysis on the population of MTs possessing a partially attached (end) segment and one major portion which remains freely fluctuating. For such partially attached MTs, we avoid trivial spacial rotations of the whole MT as real fluctuations. Instead we focus only on the relevant intrinsic motions with respect to fixed reference frame at the attachment point.

Among the several definitions of the persistence length, we consider the one defined by lateral fluctuation as

$$l_p^* = \frac{L^3}{3\langle(\delta r_\perp(s))^2\rangle}, \tag{4.2}$$

where the variance $\langle(\delta r_\perp(s))^2\rangle = \langle(r_\perp(s) - \langle r_\perp(s)\rangle)^2\rangle$ is obtained by the in-plane lateral displacement $r_\perp(s)$ at position s and $\langle\cdot\rangle$ is the time average. Figure 4.6(a) shows the typical sequences of shapes of confined MTs, where the four contours extracted out of 511 frames are superimposed onto the image in different colors. Figure 4.6(b) to (d) show the measurements of the effective persistence length l_p^* for three different MTs as a function of the position s. The attachment point (AP) is determined as a crossover between plateau (corresponding to adsorbed segments) and linear growth as shown in inset of Fig. 4.6(b). Near the AP, pixel noise becomes dominant over the real signal from the fluorescent MTs leading to growth of l_p^* with s^3 as shown in dotted pink. This leads to an uncertainty of about $\pm\,5\,$pixels, corresponding to less than $1.5\,\mu$m. This uncertainty gives rise to an uncertainty on accurate measurement of l_p^*. The corresponding two error bounds are given by two dotted line throughout the measurements. Despite the error bars within this uncertainty region, l_p^* still robustly displays a remarkable non-monotonic oscillatory behavior around an apparent linear growth with $l_p^* \propto s$. This very unusual feature seems to be a characteristic of clamped MTs as already documented in Refs. [2,3]. Note that this growth of $l_p^*\,(s)$ is in sharp contrast with the standard semiflexible biopolymer models

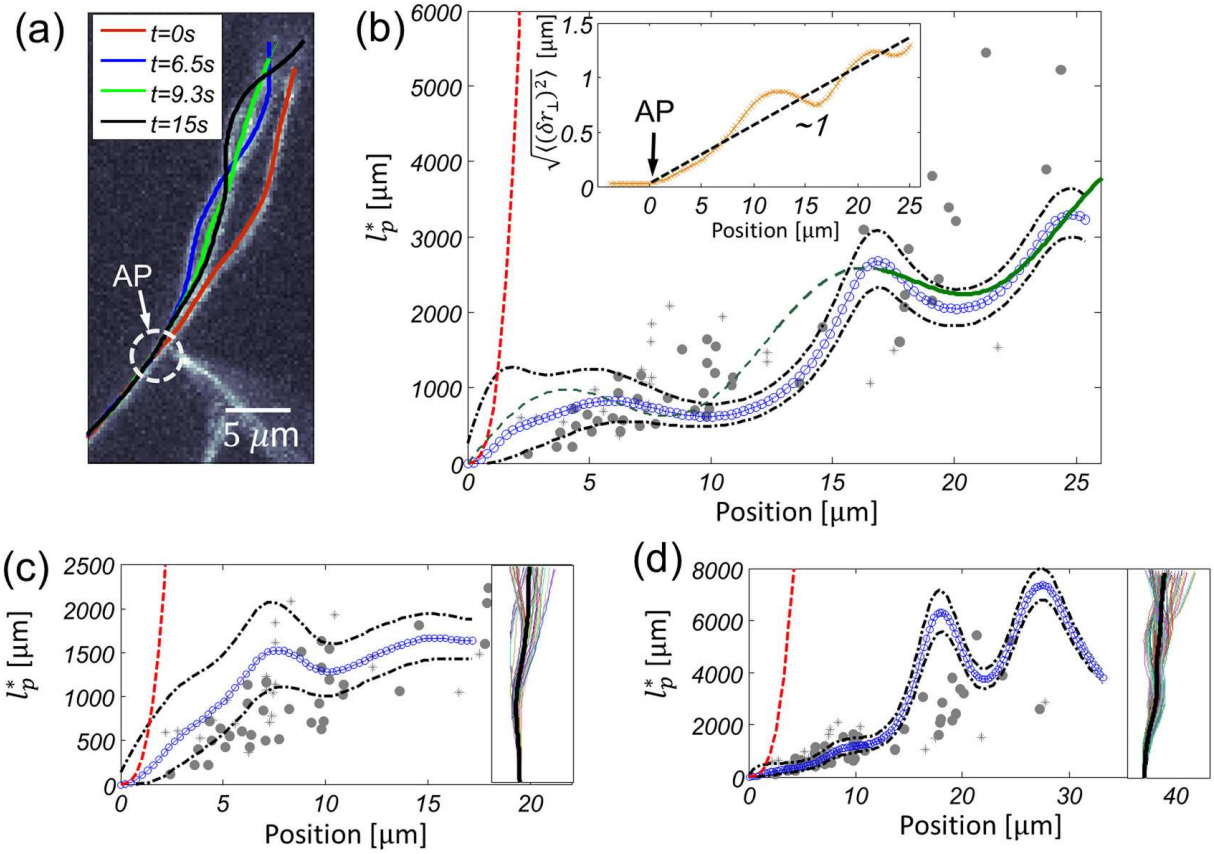

Figure 4.6: Effective persistence length l_p^* as a function of position from the AP along the clamped MT contour: experimental data (in crosses [2] and circles [3]). (a) Fitted contours are superimposed onto the images for various frames, and the region for the AP is shown by dotted circle (in while). For this MTs, (a) l_p is plotted with the error bars calculated from the uncertainty of the AP. (inset) The STD on the transverse displacement is plotted along the position. (c-d) l_p measurement for another two examples of MTs and their contours are presented as inset, where the mean position of the lateral fluctuations is denoted in black line.

(describing e.g. DNA and actin-filament) where l_p is merely given by a constant.

For three MTs in Fig. 4.6, the measured l_p^* agrees well with previous experiment data on clamped MTs [2, 3]. However, it is clearly seen that there is one prominent difference with the data of Pampaloni et al. [2] and Taute et al. [3]. While the data in [2,3] show a linear correlation between the length and l_p^* with a somehow noisy distribution around a line $l_p^* \propto s$,there is no clear oscillation of $l_p^*(s)$ observable from their data, it is possibly because of the large error bars. In contrast to [2, 3], our data display a clear oscillatory trend in $l_p^*(s)$. Interestingly the polymorphic MT model for clamped MTs proposed in [116] predicts a linearly growing $l_p^*(s)$ with oscillations which are an intrinsic geometric signature of a rearranging MT's helical polymorphic state. A direct fit of this theory to our data reveals some differences with previous predictions [116]. While the theory [116] applied to data sets of Pampaloni et al. [2] and Taute et al. [3] predicted a unique helical wavelength (or pitch) $P \approx 7.5\,\mu$m, our data display more spread wavelengths depending on MT specimen - in the range from $P \approx 8\,\mu$m (in blue contour) to $18\,\mu$m (in black contour) in Fig. 4.6(a).

We should note that there are several effects that could influence the MT wavelength in our experiment and in turn modify the outcome of the $l_p^*(s)$ measurement as compared to previous experiments [2, 3]. Firstly the presence of the glass surface in our case will partially hinder the free motion of the polymorphic helix (called "wobbling motion" in [116]). The segment sections closer to the attachment point will be more constrained due to interaction with the substrate, whereas the other end is more free to move in the z-direction and can thus assume more easily the preferred wavelength of free chain. This is visually confirmed by the observation that the ends of chains appear more often out of focus but also more curved than the sections closer to the attachment point. Also, we cannot exclude the effect that we might be dealing with a different lattice type - distinct from that predominantly analysed by Pampaloni et al. [2] and Taute et al. [3]. In their experiments there might have been a slight psychological bias towards the more straight looking MT specimen (for understandable experimental reasons) which in case of multiple lattice / helix types would select in favor of the more slender helices (i.e. those with smaller amplitudes). Keeping in mind that the visible amplitude (radius) of a helix scales as $R \sim \omega_1 P^2$ (where ω_1 is the curvature and P the pitch of the helix) a pitch that is twice as small will give a four times smaller helix radius, and possibly render smaller pitch (smaller radius) helices difficult to identify and observe. In our analysis, to avoid pixel noise and other artifacts we have focussed on most robust and largest amplitude helices and their motions. Consequently we might have possibly created an opposite bias towards larger pitch (and thus

larger radius) helices as compared to those in Refs. [2, 3]. Nevertheless, the overall features of l_p^* profiles measured here are in qualitative agreement with previous experiments. Moreover, our present data provide us with a principal hint towards the mechanism behind the "length-dependent stiffness phenomenon" : the involvement of MTs superhelicity and the polymorphic rearrangement motions.

4.6 Conclusion

In this chapter, we have observed anomalous thermal motion of fluorescently labelled MTs confined in a slab geometry. We have found that taxol-stabilized MTs under confinement often display a wavy shape reflecting a superhelical structure of MTs in 3-d. We have characterized the helicity of the MTs by constructing the relation between helical radius and pitch, and found some correlation between them. This correlation is understood as coming from a 3-d helix of variable pitch and constant curvature squeezed to almost 2-d flat geometry. The analysis of shapes allow us to extract the relevant helical parameters, pitch $\sim 13\,\mu$m$(\pm 4.5\,\mu$m) and radius of curvature $\sim 21\,\mu$m.

Notably we have observed a new type of anomalous thermal motion of MTs which is qualitatively different from usual semiflexible filament behavior. In particular we have witnessed sudden conformational transitions of MT shapes in two general classes: correlated curvature reorientations and correlated curvature magnitude transitions corresponding to transformations from curved to straight shapes and vice versa. These conformational transitions show a high degree of cooperativity as corroborated by correlation coefficients between adjacent sections' mean curvatures. As a possible mechanism for the observed behavior, we suggest switching of the tubulin dimers between straight and curved state and the involvement of cooperative interactions along the protofilament's axis as hypothesized previously in a theoretical model [116]. This polymorphic MT model predicts a high degeneracy of the superhelical ground state and thus a permanently cooperatively reshaping MT with an evolving reference ground state configuration due to thermal fluctuations. The most intriguing potential consequence of our experimental findings in this work is that the superhelicity and its cooperative switching could be caused by a strong cooperative effectively long-range interaction which originates from the specific interactions of tubulin subunits. To test this hypothesis and explore its biological implications remains one of the most fascinating future challenges.

Chapter 5

Helices at flat interfaces: Conformational transformation of a helical chain under two-dimensional confinement

Helically coiled filaments are frequently found in nature as illustrated below in Fig. 5.1. In vitro, the helices are squeezed into flat two-dimensional surfaces. Under such confinement, the helices form peculiar shapes: looped waves, spirals, or circles, which we named "squeelix". In this chapter, we study those conformations by introducing the helical WLC model with bending and twist modulus and preferred curvature and twist. In 3d, the chain has a helical shape (ground state) satisfying preferred curvature and twist everywhere. When confined in 2-d surface, the chain displays a variety of shapes which are similar to those found in experiments. In analogy to soliton physics, we introduce the "twist kink" as a discrete quasi-particle, and discuss the filament shape and its fluctuations in terms of twist kink injection, interaction, and diffusion. Numerical study will show the emergence of squeelix shapes, and those shapes can thermally switch between discrete twist-induced conformational states. The notion of squeelix has been used in the previous chapter on MTs.

5.1 Introduction

Among a number of examples of helically coiled filaments, the most prominent ones are FtsZ [36], Mrb [37], bacterial flagella [75,76], tropomyosin [126], and intermediate filaments [38]. More recently microtubules were suggested to spontaneously form large scale superhelices [4]. Even whole microorganisms exhibit helicity inherited from their constituent filaments [127]. The superhelicity of filaments is in some cases of strong evolutionary benefit as in the example of swimming bacteria utilizing the rotational motion of their helical flagellar filament for propulsion [128] and tropomyosin's helical "Gestalt-binding" around actin [126]. In addition to biological evolution artificial, man-made helically coiled structures have been created including coiled carbon nanotubes [129–131], DNA nanotubes [132], and coiled helical organic micelles [133].

As observed in experiments, we introduce 2-d confinement to simplify observational conditions. This changes the physical properties of the helical chain in initially unanticipated but physically rather interesting manner. The purpose of this work is to investigate the rich physical effects of confinement on helical filaments. As we will show, the confinement changes the shapes dramatically, and statistical mechanics of the confined helix generates several notable effects: (i) Enhancement of cyclization probability, (ii) Enhancement of end-to-end distance fluctuations, and (iii) Generation of conformational multistability (despite apparent linearity of constitutive relations). We will see that the conformational dynamics of confined helices is most naturally described in terms of the "twist kinks" entities (cf. Fig. 5.1). We show that these "twist kinks" are completely analogous to overdamped Sine-Gordon-kinks from soliton physics [134] as well as loops in stretched elastic filaments [135]. These analogies will help us to develop a phenomenological understanding of the underlying physics. The peculiar shapes specified above appear not be rationalized by the conventional Worm Like Chain model. This riddle feature is the starting point of our investigation. In this chapter, we propose a new augmented model of confined intrinsically curved and twisted chains that leads to a variety of 2-d shapes matching experimental observations.

5.2 The Phenomenology of Squeezed Fluctuating Helices

Consider a filament of bending modulus B, twist modulus C and preferred curvature ω_1 and twist ω_3. In 3d, preferred curvature and twist are satisfied everywhere simultaneously by the proper helix. In 2d, some frustration cannot be avoided. Phenomenologically, the main effect of confinement is to introduce narrow regions where the twist is localized (concentrated) and the curvature flips. We call this inflection points as "twist-kinks" borrowing the concept of kinks in soliton physics [134]. Depending on the control parameter $\gamma \sim \frac{B\omega_1^2}{C\omega_3^2}$, two regimes can be distinguished:

(i) $\gamma > 1$: Twist kinks having a positive self-energy are essentially expelled and can only be thermally activated

(ii) $\gamma < 1$: Twist kinks have a negative self-energy and the ground state involves a finite density of twist kinks.

In both cases, the generic shape is a circular arc or closed circles. The twist kinks, if present, separate arcs of opposite curvature orientations resulting in a wavy undulatory 2-d shape. For a squeelix with $\gamma > 1$, the ground state over the surface is a circular arc shape that can favor the occurrence of closed filaments. This is very unlikely in the free helical state (in absence of confinement).

Our study is based on the analytical analysis of the confined Helical WLC Hamiltonian and numerical Monte Carlo simulations using the density of states method [137]. In this simulation, the parameter set (B, C, ω_1, ω_3) is assigned primarily to illustrate circularization enhancement, which allows us to focus on the most curious case of twist expulsion ($\gamma > 1$). In this regime, the chain will also comprise excited (wavy looking) states involving a discrete number of thermally activated twist-kinks. The shapes of excited states can be "hyperflexible" because an isolated twist-kink almost freely diffuses along the filament. In other words, large shape fluctuations are induced by simple translational sliding motion of the twist-kink along the contour. For parameter sets not resulting in twist expulsion ($\gamma < 1$), the ground state itself is periodically wavy. This case is less exciting as effects like circularization and hyperflexibility will be absent. For this reason we will entirely focus on more illuminating and surprising limit $\gamma > 1$.

This conceptual consideration seems appropriate for an experimentalist concerning interpreting real filaments (in real world experiments). Bacterial flagella and MTs are known to be helical filaments, but their mechanical characteristics are generally (in experimental practice) not always quite uniform along the filament. There could be frozen-in lattice defects like a jump

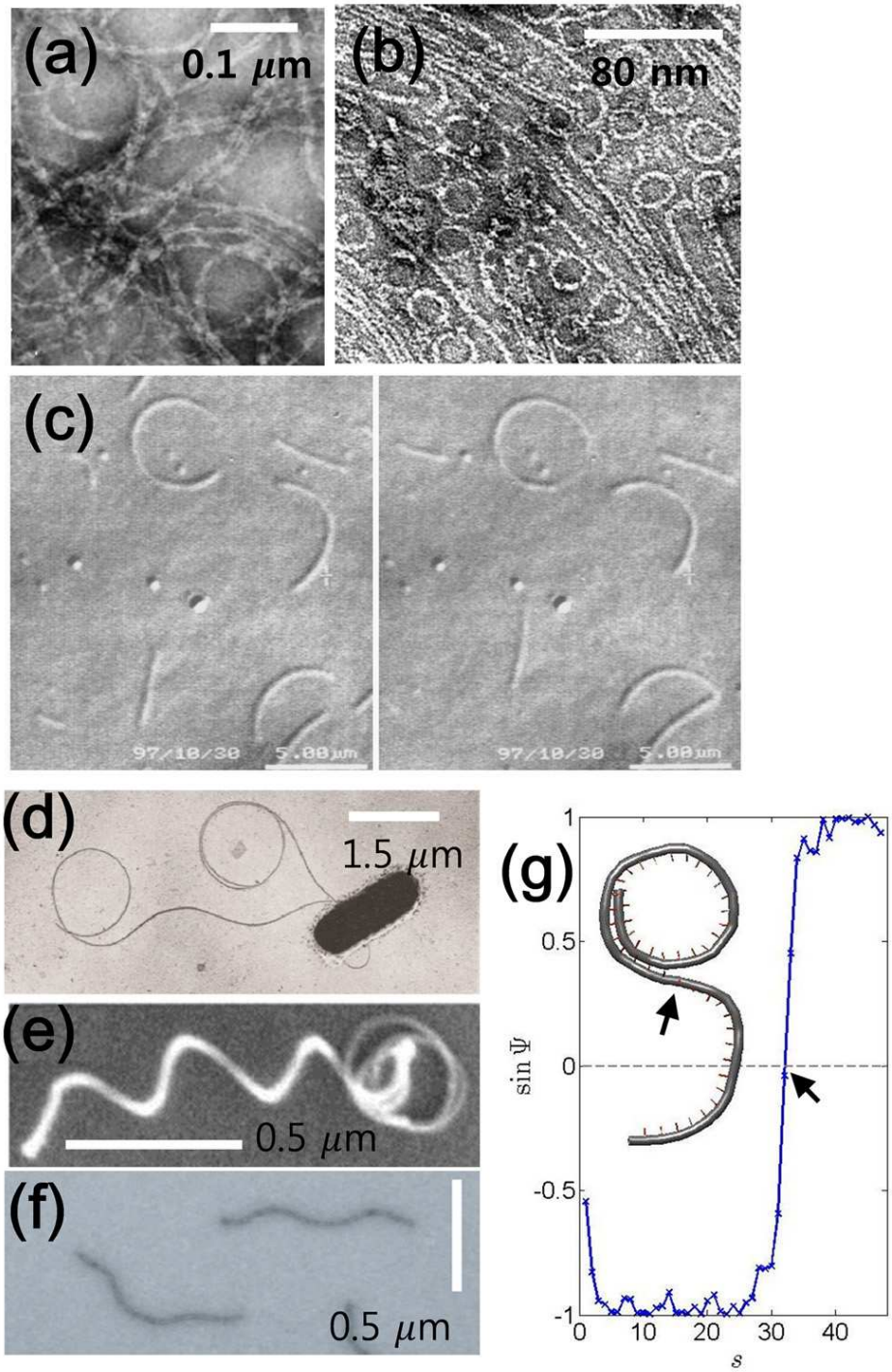

Figure 5.1: Several examples of helically coiled filaments at 2-d surface. (a) Intermediate filament [38] (b) Coiled FtsZ filament [36] (c) Gliding essay of MTs over the kinesin-coated surface showing a circular shape [136] (Scale bar: $5\,\mu$m). (d) Polymorphic helical bacterial flagella [75]. Artificial helices also show a peculiar shape. (e) Coiled carbon nanotube when adsorbed onto the substrate [129], (f) Helical DNA nanotubes [132]. (g) The simulated squeelix appears in coexisting wavy and coiled circular shapes and display a discrete "twist kink" (curvature flipping point) indicated by arrow. Twist kink is characterized by a rapid inversion of the binormal vector along the contour and by a localized twist-angle ψ variation.

in the number of protofilaments for microtubules [138] or annealed defects like a boundary between different polymorphic states in bacterial flagella. In the cases of interest, the mechanical parameters are uniform within some correlation length, which may even be larger for cleanly prepared filaments than the contour length under scrutiny. Our model is generic in the sense that it always applies to an uniform sub-filament, provided that twist kinks and boundary layers are much smaller. A clean observation of the shapes described below further supposes that shape equilibration is possible with stable mechanical parameters, i.e. before polymorphic switching.

5.3 The squeezed helical worm-like chain model

The various shapes of helices can be understood by simple considerations of their elastic energy. The elastic energy of a HWLC is written as a function of the curvatures $\Omega_{1,2}$ and twist Ω_3 as:

$$E\left[\mathbf{\Omega}\right] = \frac{1}{2}\int_{-L/2}^{L/2}\left[B(\Omega_1-\omega_1)^2 + B\Omega_2^2 + C(\Omega_3-\omega_3)^2\right]ds, \tag{5.1}$$

where B and C are the bending and torsional stiffness, respectively. The intrinsic bending and twist curvature ω_1 and ω_3 are related to the 3-d ground state of a helix with radius $R = \frac{\omega_1}{\omega_1^2+\omega_3^2}$ and pitch $P = \frac{2\pi\omega_3}{\omega_1^2+\omega_3^2}$. In order to proceed and access the filament shapes, it is convenient to express Ω_i through the Euler angles (θ, ϕ, ψ).

$$\begin{aligned}\Omega_1 &= \phi'\sin\theta\sin\psi + \theta'\cos\psi\\ \Omega_2 &= \phi'\sin\theta\cos\psi - \theta'\sin\psi\\ \Omega_3 &= \phi'\cos\theta + \psi'\end{aligned}$$

, where $()' = \frac{d}{ds}$ and s is the arc length parameter along the contour.

By imposing $\theta = \frac{\pi}{2}$, the helical chain is projected onto 2-d surface, which considerably simplifies Ω_i as:

$$\Omega_1 = \phi'\sin\psi, \quad \Omega_2 = \phi'\cos\psi, \quad \Omega_3 = \psi' \quad (\text{squeelix}). \tag{5.2}$$

Then, the elastic energy of the squeelix is written as a function of ϕ, ψ:

$$E\left[\phi,\,\psi\right] = \frac{1}{2}B\int_{-L/2}^{L/2}\left((\phi')^2 - 2\omega_1\phi'\sin\psi + \omega_1^2\right) + c\left(\psi'-\omega_3\right)^2 ds, \tag{5.3}$$

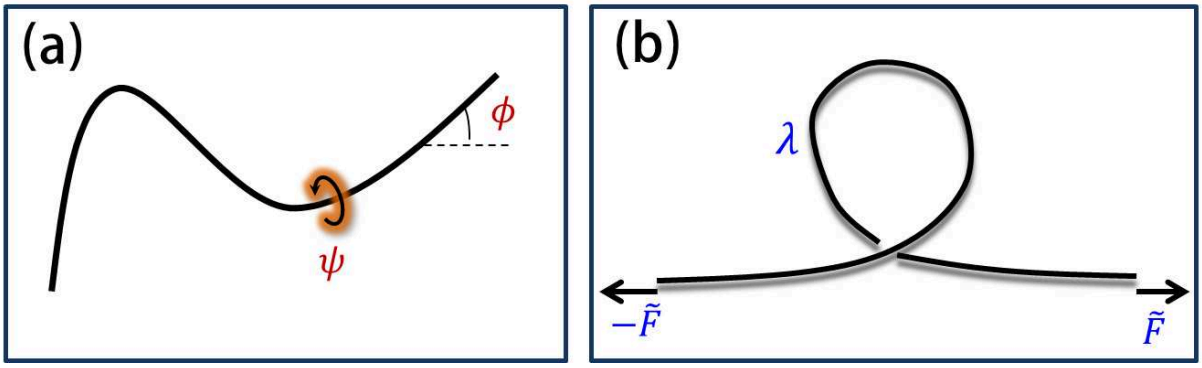

Figure 5.2: Schematic description of (a) squeelix with local twist ψ and tangent angle ϕ and (b) WLC under tension with a loop size λ.

where $c = C/B$. Now, $\phi'^2(s) = \Omega_1^2 + \Omega_2^2 \equiv \kappa^2(s)$ is in-plane local curvature of the chain and $\psi'(s) = \Omega_3$ is the local twist. The optimal shape of chain is obtained via the Euler-Lagrange equations:

$$\begin{aligned} \frac{\partial E}{\partial \phi} &= B\frac{d}{ds}\left(\phi' - \omega_1 \sin\psi\right) = 0 \\ \frac{\partial E}{\partial \psi} &= 2\omega_1\phi' \cos\psi + 2c\frac{d}{ds}\left(\psi' - \omega_3\right) = 0. \end{aligned}$$

For an uniform "helix" with constant ω_1 and ω_3:

$$\phi' = \omega_1 \sin\psi \tag{5.4}$$

$$\psi'' + \frac{\omega_1^2}{2c}\sin 2\psi = 0. \tag{5.5}$$

If there is no external torque applied on the HWLC, the twist must satisfy the boundary conditions $\psi'(-L/2) = \psi'(L/2) = \omega_3$. As shown in Eq. 5.4, under the confinement the curvature is determined by the twist and is no more an independent parameter as for a free chain. This obviously is at the origin of the localization of twist. From Eq. 5.5, we see that $\psi(s)$ is solution of a pendulum equation and thus is the Elliptic Jacobi function[1].

[1]The solution is $\psi(s) = am\left(\sqrt{a}(s - s_0)|\frac{\omega_1^2}{ca}\right)$ (elliptic amplitude function) where the constants of integration a and s_0 are determined by the boundary conditions.

Analogy with WLC under tension

For better intuition, we map our problem into a WLC under tension (hereafter, WLCT). To do so, we introduce a new angle $\vartheta/2$ as $\psi = \pi/2 + \vartheta/2$. By plugging Eq. 5.4 in Eq. 5.3, the energy is rewritten as a function of ϑ

$$E\left[\vartheta\right] = \int_{-L/2}^{L/2} \left[\frac{1}{2}\tilde{A}\vartheta'^2 + \tilde{F}\left(1-\cos\vartheta\right)\right] ds - \frac{M}{2}\left[\vartheta\left(L/2\right) - \vartheta\left(-L/2\right)\right], \tag{5.6}$$

where we represent $\tilde{A} = C/4$ as the effective bending modulus of the WLCT and $\tilde{F} = B\omega_1^2/4$ as the effective external force acting on it (cf. Fig. 5.2). The first integral term is precisely the WLCT energy. The last term represents an energy related to the loop accumulation, where the notation $M = \omega_3 C$ is introduced to stand for two external antagonistic torques exerted on both ends. If the torque is large enough, extra n turns or loops are accumulated on the contour, which enforces $\vartheta\left(L/2\right) - \vartheta\left(-L/2\right) = 2\pi n$ or in the ψ representation n twist-kinks along the squeelix.

The phenomenology of the stretched chain makes the mapping attractive. The decay length of a localized distortion (correlation length) λ is also the optimal size of loop grown against the tension $\tilde{F}$ (in the loop picture) or kinks-spatial extension (in the twist-kink picture, this will be discussed below):

$$\lambda = \sqrt{\frac{\tilde{A}}{\tilde{F}}} = \frac{1}{\omega_1}\sqrt{\frac{C}{B}}. \tag{5.7}$$

The WLCT loop stores a typical energy $\sim \lambda\tilde{F}$. If the work of the external torques $2\pi M$ per loop reduces sufficiently the WLCT energy, loops form spontaneously (otherwise they can be thermally activated). We hence conclude that the ground state is wavy for $M \gtrsim \lambda\tilde{F}$, which translates into $\frac{B\omega_1^2}{C\omega_3^2} \lesssim 1$, and circular otherwise.

Now, let us return to a circular shape, in this case the twist expulsion parameter $\gamma > 1$, which corresponds to a WLCT without loops in the ground state. We hence consider a WLCT with $\vartheta = 0$ (no loop) everywhere along the chain except at the ends where there is a small deformation due to the boundary condition $\vartheta'(-L/2) = \vartheta'(L/2) = 2\omega_3$. The solution for the WLCT without loop corresponds to a constant angle $\psi = \pi/2$ along the chain, and there is no twist in this case $\psi' = 0$ and the curvature is constant $\phi' \approx \omega_1$. This corresponds to a circular arc of constant curvature, from which the twist has been completely expelled.

Concerning the small deviation at the edges, the energy of a nearly circular shape can be

determined by expanding Eq. 5.6 for small deformation $\vartheta \ll 1$:

$$E[\vartheta] \simeq \int_{-L/2}^{L/2} \left(\frac{1}{2}\tilde{A}\vartheta'^2 + \frac{1}{2}\tilde{F}\vartheta^2 \right) ds - \frac{M}{2} \left[\vartheta(L/2) - \vartheta(-L/2) \right]. \tag{5.8}$$

The associated elastic Euler-Lagrange equation produces a differential equation $\vartheta'' = \lambda^{-2}\vartheta$. Applying the boundary condition, the solution is obtained as

$$\vartheta(s) = \frac{4}{\pi\sqrt{\gamma}\cosh(L/2\lambda)} \sinh(s/\lambda), \tag{5.9}$$

where the control parameter γ is introduced with prefactor (see below):

$$\gamma = \frac{4}{\pi^2} \frac{B\omega_1^2}{C\omega_3^2}. \tag{5.10}$$

The small deflection hypothesis on the WLCT is satisfied provided $\gamma > 1$, i.e. deep in the twist expulsion regime. In a consistent picture, the twist-kink density should be calculated including shape fluctuations, i.e the coupling of the twist kink to the small thermal deformations. This is taken into account by the simulation presented in this chapter. Simple geometry allows to calculate the shape fluctuations associated with the *free* motion of the narrow twist-kink along the filament in the excited state. This soft mode gives rise to large fluctuations in the excited state reported in this work.

Single twist-kink solution: Shape and Self-energy

For one isolated twist kink on an infinite filament, the solution of Eq. 5.5 can be obtained easily. For this shape, the boundary condition is given by $\psi(\pm L/2) = \pm\pi/2$. By multiplying ψ' to both sides of Eq. 5.5, one can get the first integral:

$$\frac{d\psi}{ds} = \pm\sqrt{a_2 - \frac{\omega_1^2}{c}\sin^2\psi}. \tag{5.11}$$

The boundary condition $\psi'(-L/2) = \psi'(L/2) = 0$ determines $a_2 = \frac{\omega_1^2}{c} \equiv \frac{1}{\lambda^2}$, where we encounter $\lambda = \sqrt{\frac{C}{B\omega_1^2}}$ again. For a squeelix having twist-kinks, λ measures the size of the twist-kink along the contour.

By integrating Eq. 5.11, the solution of Eq. 5.5 is obtained as

$$\psi(s) = 2\arctan\left(\exp(s/\lambda)\right) - \pi/2. \tag{5.12}$$

Rewriting this equation

$$\sin\psi\left(s\right) = \tanh\frac{s}{\lambda}, \tag{5.13}$$

which describes the localized twist-angle ψ variation. The corresponding chain shape is given by:

$$\phi'\left(s\right) = \omega_1 \tanh\frac{s}{\lambda} \quad \text{and} \quad \phi\left(\mathrm{s}\right) = \omega_1\lambda \ln\left|\cosh\frac{\mathrm{s}}{\lambda}\right|, \tag{5.14}$$

in which one can see that the twist-kink is localized provided that $L \gg \lambda$ and separates two flipped regions of almost constant curvature $\approx \omega_1$.

By plugging Eq. 5.12 in Eq. 5.6, the self-energy of the twist-kink is obtained as energy of WLCT featuring one loop:

$$\begin{aligned} E_{1kink} &= \underbrace{8\sqrt{\tilde{A}\tilde{F}}}_{E_{loop}} - \underbrace{\pi M}_{E_{torque}} \\ &= (\sqrt{\gamma} - 1)\pi C\omega_3 \end{aligned} \tag{5.15}$$

where γ is the twist-kink expulsion parameter introduced previously. As mentioned earlier, $\gamma = 1$ separates the regime of positive and negative self-energy.

5.4 Simulation

5.4.1 Simulation model for a squeelix

We modelled a HWLC consisting of N-monomers, whose position vector are represented by $\mathbf{r}_i$ (i=1, 2, ... N). The shape of HWLC can be described by a material orthonormal frame $\{\mathbf{f}_i, \mathbf{v}_i, \mathbf{u}_i\}$ [139] where $\mathbf{u}$ is tangent vector defined as $\mathbf{u}_i = \mathbf{r}_{i+1} - \mathbf{r}_i$ satisfying the constraint $|\mathbf{u}_i| = 1$ for all i. The normal and binormal vector $\mathbf{f}$ and $\mathbf{v}$ are pointing two perpendicular directions to the tangent, and $\mathbf{u}_i = \mathbf{f}_i \times \mathbf{v}_i$. The total energy of a confined helix consists of the elastic and confinement energy $E_{tot} = E_{el} + E_{conf}$. The discretized version of elastic energy is

given by

$$E_{el} = \frac{1}{2}\sum_{i=1}^{N-2} B\left\{(\Omega_{1,i}-\omega_1)^2+\Omega_{2,i}^2\right\} + C(\Omega_{3,i}-\omega_3)^2, \tag{5.16}$$

where the strain tensor $\mathbf{\Omega}_i = (\Omega_{1,i}, \Omega_{2,i}, \Omega_{3,i})$ is defined for each body frame as

$$\begin{aligned}
\Omega_{1,i} &= (\mathbf{u}_{i+1}-\mathbf{u}_i)\cdot\mathbf{f}_i \\
\Omega_{2,i} &= (\mathbf{u}_{i+1}-\mathbf{u}_i)\cdot\mathbf{v}_i \\
\Omega_{3,i} &= (\mathbf{v}_{i+1}-\mathbf{v}_i)\cdot\mathbf{f}_i.
\end{aligned}$$

The chain is confined under harmonic potential so that each monomer located at distance z away from the surface experiences potential $E_{conf} = Kz^2$. In this work, $B = 50$, $C = 25\,k_{\mathrm{B}}Tb$, and $K = 25\,k_{\mathrm{B}}T/b^2$, and the bond length is fixed as $b = 1$. When $K = 0$, we recover the free chain statistics in 3-d.

5.4.2 Monte Carlo simulation using Wang-Landau sampling idea

In order to gain insight into the conformation of squeelices in thermodynamic equilibrium, we performed Monte Carlo simulation using density of states method [137]. The equilibrium conformational statistics of squeelices can be obtained via the calculation of the density of states (DOS), $g(E)$. Once $g(E)$ is obtained, the average of a quantity A that depends on E only can be computed using

$$\langle A\rangle = \frac{\int d\mathbf{r}\, A(\mathbf{r})\exp[-\beta E(\mathbf{r})]}{\int d\mathbf{r}\exp[-\beta E(\mathbf{r})]} = \frac{\sum_E A(E)g(E)e^{-\beta E}}{\sum_E g(E)e^{-\beta E}} \tag{5.17}$$

The bracket denotes an average in the canonical ensemble and $\beta = 1/k_{\mathrm{B}}T = 1$. At given end-to-end distance D, each conformation of energy E_r contributes with statistical weight $\exp\left[-\beta E_r(D)\right]$. To compute an ensemble average at a given extension D, we have to compute the density of states as a two-dimensional function $g(E, D)$, so called JDOS. Sampling of two-dimensional histograms is often computationally more demanding than one-dimensional histograms. For efficient sampling, we used the global update method introduced by [140].

The average end-to-end distance $\langle D \rangle$ can be computed by

$$\langle D \rangle = \frac{\sum_{E,D} D g(E,D) e^{-\beta E}}{\sum_{E,D} g(E,D) e^{-\beta E}}. \tag{5.18}$$

In the calculation of $g(E,D)$, the ranges on E and D are assigned in order to cover the wide range of the conformational states. The bin sizes for the sampling are chosen as $dE = 0.5\, k_{\mathrm{B}}T$ and $dD = 0.5\, b$ (in the unit of monomer size). From the obtained JDOS, we calculate the probability distribution of D within the interval of $[D, D + dD]$ using:

$$p_d(D) = \frac{\sum_{E} g(E,D) e^{-\beta E}}{\sum_{E,D} g(E,D) e^{-\beta E}}. \tag{5.19}$$

In order to generate a new conformation of a chain, we introduced two types of Monte Carlo (MC) moves: pivot and pure twist. Within each pivot move, a randomly selected monomer is rotated by an arbitrary angle around the axis defined by two neighboring monomers. This move changes the chain shape and twist simultaneously. By pure twist, $\mathbf{f}$ and $\mathbf{v}$ are only updated by rotation with respect to the local tangent. To enhance the sampling and avoid being trapped in local energy minimum, the large scale pivot is furthermore introduced once for each MC sweep (MCS). This move is tried in such a way that a vector $\mathbf{r}_N - \mathbf{r}_{i=2,\ldots,N-1}$ defined by a selected $i-$th monomer is reoriented by a set of arbitrary euler angles. Each computation of $g(E,D)$ of 16-mer with accuracy $f_{final} = \exp(10^{-6}) \simeq 1.000001$ reduced from $f_{initial} = \exp(1.0)$ takes approximately 1 hour on a Intel Xenon CPU at 2.40 GHz, 8192 MB RAM running Linux.

5.5 Simulation results

We performed our simulations for several chain lengths, $N = 16, 32, 64$. Throughout the simulation, the mechanical constant is fixed as $B = 50\, k_{\mathrm{B}}Tb$ and $C = 25\, k_{\mathrm{B}}Tb$, respectively. One of main goal of our simulation is to quantitatively study the conformational changes of a helix upon confinement. As discussed above, the twist expulsion parameter γ determines the chain's shape over the surface. We first verify that from the simulation. The results are shown in Fig. 5.3. For $\gamma > 1$, the chain becomes a circular shape as shown in the process $(a) \rightarrow (a')$, where the binormal vectors (shown in red) pointing all the same direction indicates that twist is expelled. The normal vectors (shown in blue) are in-plane and pointing the center of circle.

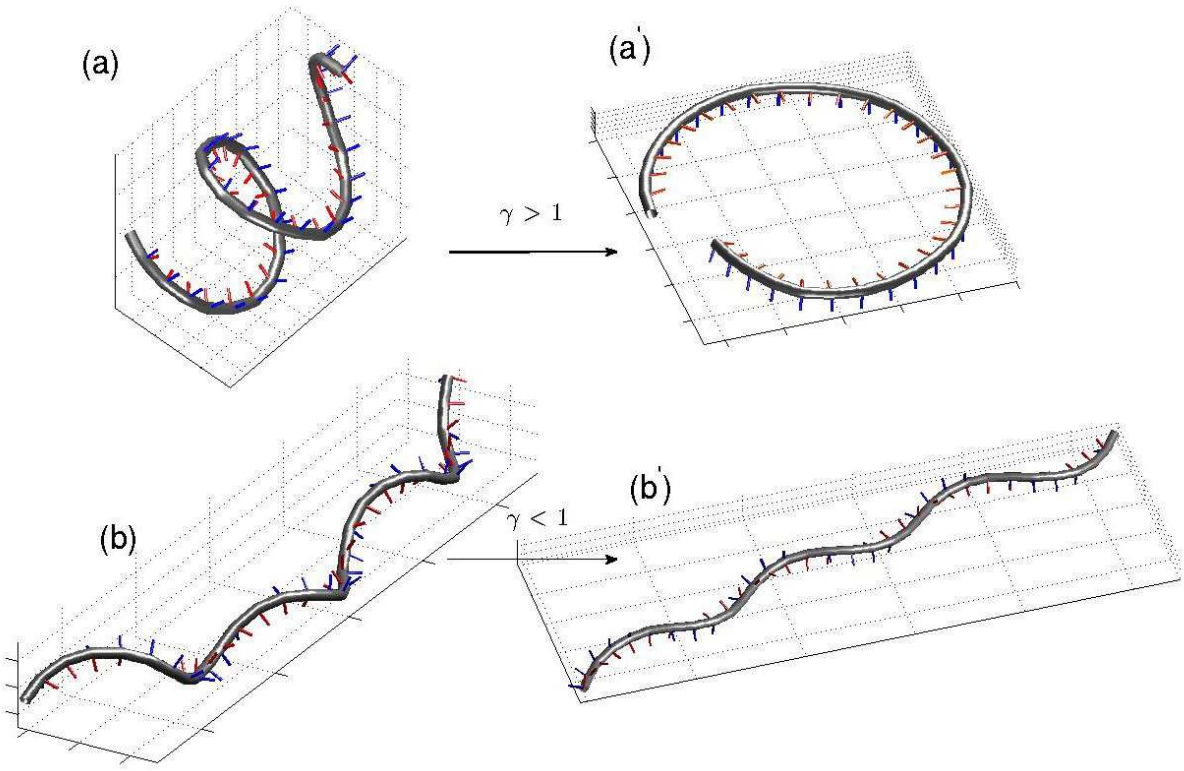

Figure 5.3: Formation of two different types of conformations of a confined helix depending on the twist expulsion parameter γ. The contour is represented by a tube shape with normal (in red) and binormal (in blue) vectors. (a) and (b) are typical helical chain shapes in 3-d before confined. When confined, (a′) untwisted and circularized shape ($\gamma > 1$) and (b′) twisted and wavy shape ($\gamma < 1$) are formed.

For $\gamma < 1$, on the other hand, the chain is twisted and stretched in the process of confinement $(b) \rightarrow (b')$. The "twist-kink" emerges on a wavy shape, where in-plane normal vectors switches their signs. Note that the number of twist-kinks significantly influence on the shape of the chain and its fluctuation.

A variety of chain's shapes is characterized in terms of two quantities, the end-to-end distance D and the number of inflection points $n = \frac{1}{\pi}\sum_i^{N-2}\Omega_{3,i}$. The latter is a statistical analogue of the discrete twist kink number in the theoretical consideration above. The density of states $g(E, D, n)$ is computed in the simulation as a function of these quantities and energy E.

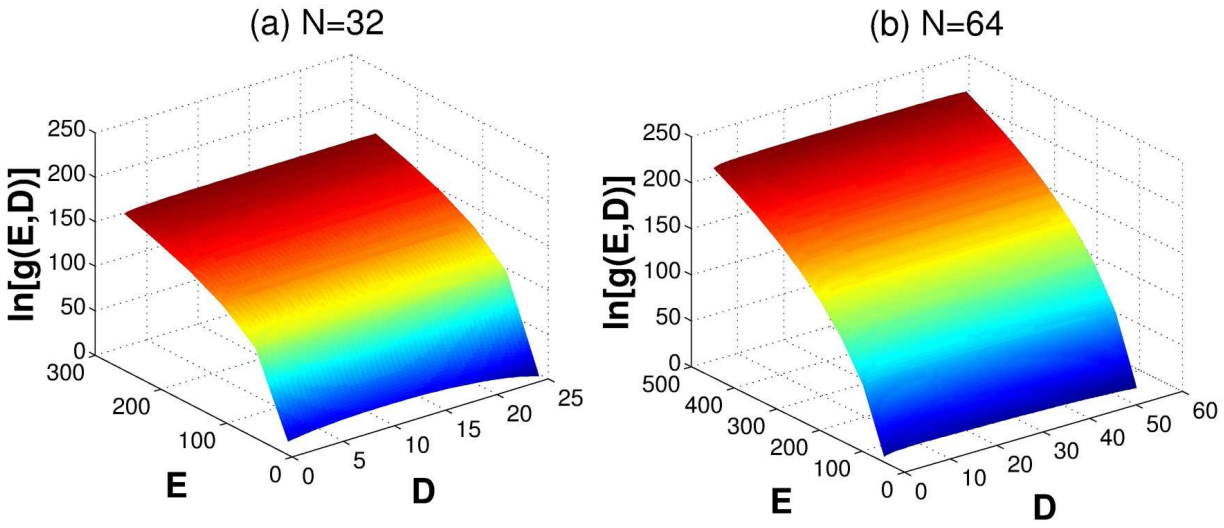

Figure 5.4: Joint density of states for a confined helical chain of length (a) $N = 32$ and (b) $N = 64$. The colored surface represents the $\ln[g(E, D)]$ as a function of total energy E and end-to-end distance D.

5.5.1 Joint Density of States

As the main product of the simulation, we obtained the JDOS for a confined helix of length $N = 32, 64$. The parameter set (ω_1, ω_3) is chosen for $N = 32, 64$ as $(0.15, 0.1)b^{-1}$ and $(0.09, 0.08)b^{-1}$, respectively, and always $\omega_2 = 0$ to make an uniform helix in 2d. The ground state of 2-d is a circular shape satisfying $\gamma > 1$. Figure 5.4 presents the estimated JDOS over a given range of E and D. To avoid the numerical divergence, the logarithmic value of $g(E, D)$ is computed. The range of energy E and end-to-end distance D are assigned to cover large enough conformational states, from a circular shape of ground state to a completely random conformation. For data analysis, the corresponding energy range are chosen in such a way that the largely contributing states to the average are located within the energy range. For $N = 32$ with $E = [10, 300]\, k_{\mathrm{B}}T$, the temperature varies for $T = [0.3, 10]\, k_{\mathrm{B}}^{-1}$.

5.5.2 Hypercyclization

The phenomenological arguments presented in Fig. 5.3 predict a significant circularization enhancement for a twist-expelling chain ($\gamma > 1$). We subject this hypothesis to a simulation test. By using JDOS, the partition function and end-to-end distance distribution can be calculated

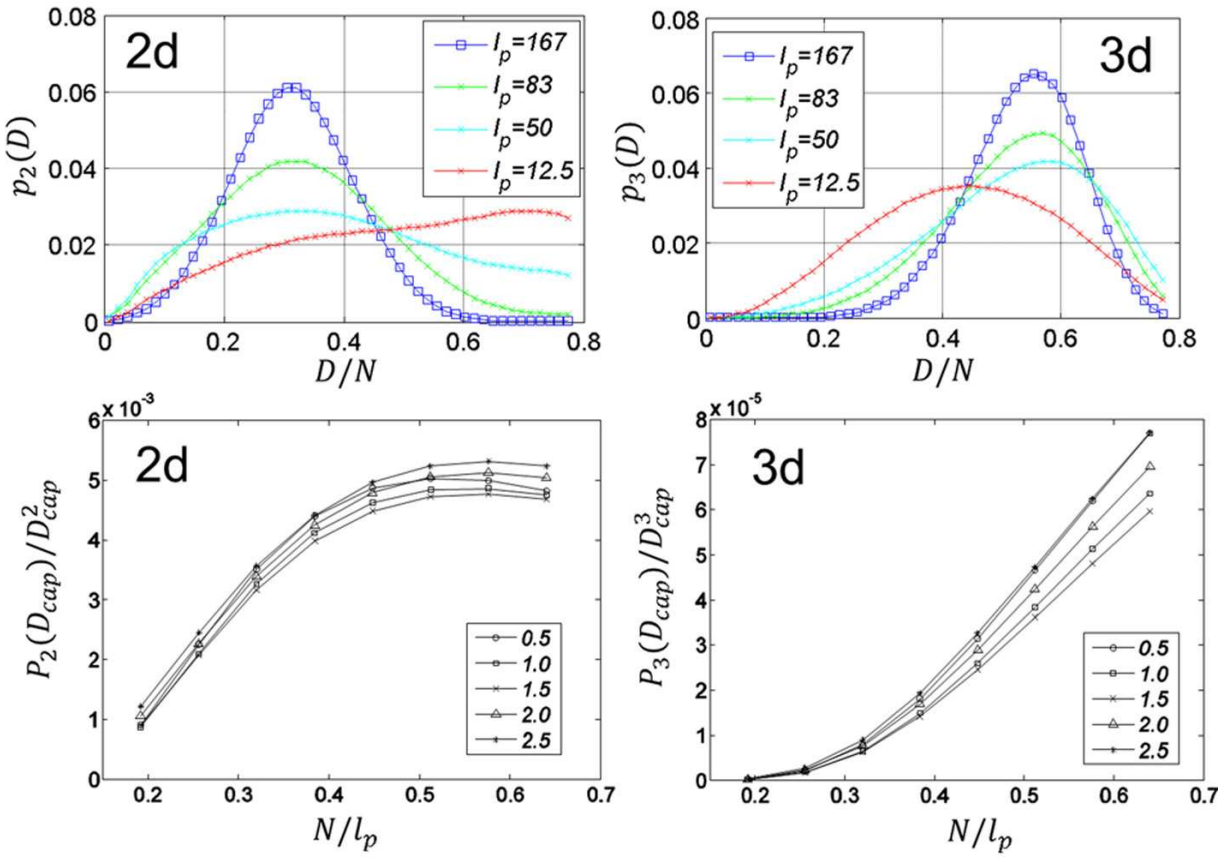

Figure 5.5: (Top panels) The end-to-end distance D distribution $p_d(D)$ at various temperature $l_p = 167,\ 83,\ 50,\ 12.5\, b$. (Bottom panels) Normalized capturing probability $P_d(D_{cap})/D_{cap}^d$ as a function of N/l_p for $D_{cap} = 0.5,\ 1.0,\ 1.5,\ 2.0,\ 2.5\, b$. (a) 2d and (b) 3d. $N = 32$, $\omega_1 = 0.15\, b^{-1}$, $\omega_3 = 0.1\, b^{-1}$, and $\gamma \approx 1.8 > 1$.

as

$$Z(T) = \sum_{E,D} g(E,D) e^{-\beta E} \tag{5.20}$$

$$p_d(D,T) = \frac{1}{Z(T)} \sum_{D} g(E,D) e^{-\beta E}. \tag{5.21}$$

For the geometric parameters $\omega_1 N = 4.8$ and $\omega_3 N = 3.2$ and the elastic constant ratio $B/C = 2$, the twist expulsion parameter is given as $\gamma = 1.82$ larger than unity, which ensures the circular shape of ground state in 2d. In the absence of confinement, the chain with such pa-

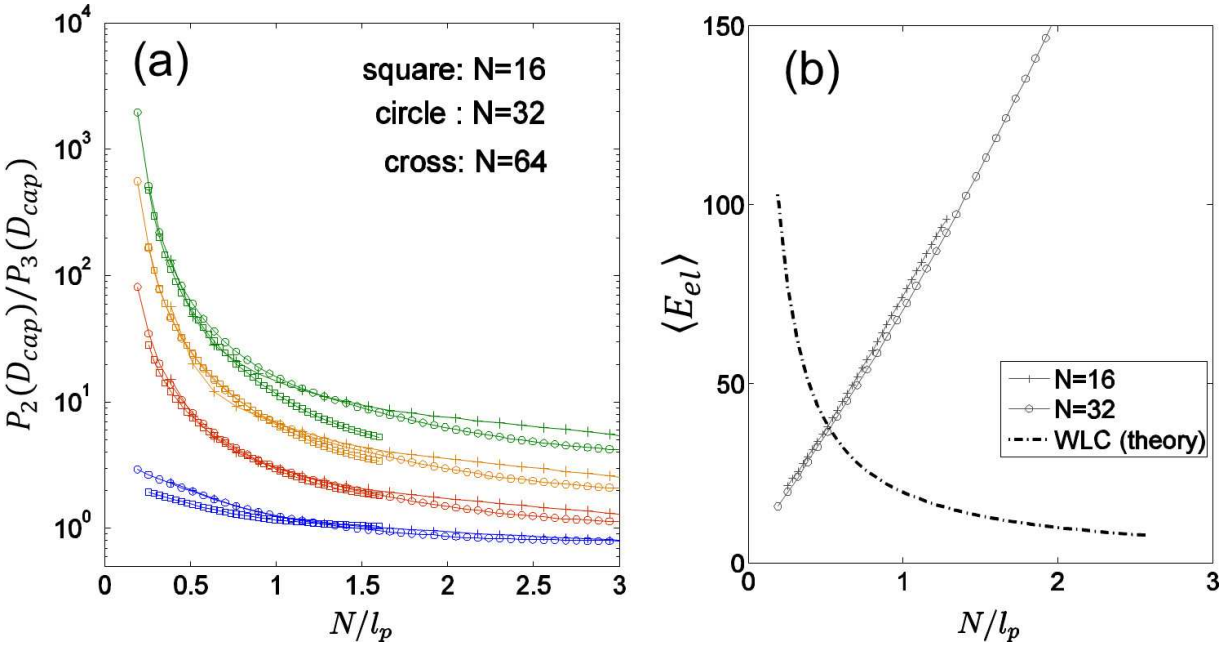

Figure 5.6: (a) Plot of ratio $P_2(D_{cap})/P_3(D_{cap})$ as a function of N/l_p for $N = 16, 32, 64$. The given values are scaled according to the geometric capture distance D_{cap}/N. From top to bottom $D_{cap}/N = 1/16\,(\text{green}),\ 1/8\,(\text{orange}),\ 1/4\,(\text{red}),\ 1/2\,(\text{blue})$. The data collapse for the same geometric ratio. (b) Mean elastic energy of a confined helix $\langle E_{el} \rangle$ plotted as a function of N/l_p. Dashed line indicates the bending energy of a circularized WLC by theory. The simulation data of $N = 16,\ 32$ are collapsed.

rameters has a helical shape whose radius and pitch $R = 0.14Nb$ and $P = 0.62Nb$, respectively. When a chain is confined to 2-d surface, on the other hand, it transforms into a slightly open but approximately circular shape with the end-to-end distance $\frac{D_0}{Nb} \approx \left|\frac{2}{\omega_1 N} \sin\left(\frac{\omega_1 N}{2}\right)\right| = 0.28$. In this case, the newly formed ground state under confinement seems to enhance circularization.

To quantify the circularization enhancement, we define the circularization probability $P_d(D_{cap})$ for both chain ends to meet within the capture distance D_{cap} as

$$P_d(D_{cap}) = \int_0^{D_{cap}} p_d(D) dD, \tag{5.22}$$

where the index $d = 2,\ 3$ stands for the dimensionality of the chains (confined one in 2d or free one in 3d). Figure 5.5 shows the circularization probabilities in both 2d and 3d for chains with various flexibility l_p. Note that l_p is related to the temperature via $l_p = B/k_{\mathrm{B}}T$.

In the top panels of Fig. 5.5, the maximum of $p_3(D)$ (blue line) is located at about

$D = 0.58Nb$ which is close to the expected helical pitch at a given parameter. In contrast, the largest closure probability in 2-d (blue line) is located at about $D \approx 0.3Nb$ which corresponds to D_0 in the estimate of the end-to-end distance of circular shape in the 2-d ground state. At high temperatures, chains are more flexible and the end-to-end distribution broadens due to the thermal fluctuation. In the bottom panels of Fig. 5.5, the normalized circularization probabilities $P_d(D_{cap})/D_{cap}^d$ are presented as a function of chain's flexibility N/l_p for small values of $D_{cap} < 3b$. Note that the probability is normalized by the capture area and the capture volume in each dimension, respectively.

The $P_d(D_{cap})$ reveals the probability enhancement of circularization by 2-d confinement. For quantitative estimation of circularization enhancement are computed as the relative ratio of $P_2(D_{cap})/P_3(D_{cap})$ at various small D_{cap}. As expected, the closure probability is greatly enhanced (more than 10^3) due to the confinement as seen in Fig. 5.6(a). In this graph, the different colors indicate different relative capturing sizes. For $D_{cap}/N = 1/16$ (green), in particular, the most pronounced enhancement on circularization takes place with the smallest capturing size at low temperature, which results from adjusting to a circular shape of ground state at given parameters. This is also checked by the elastic energy measurement as shown in Fig. 5.6(b). As the chain stiffens (small N/l_p), the elastic energy decreases smaller than that of WLC model.

5.5.3 Multi-stability and Hyper-flexibility

The theoretical considerations of kink solutions (Chap. 5.3 and Appendix 5.6) suggest that confining a helical chain generates a complex energy landscape with many metastable states. Some of these states, in particular those comprising only a few kinks, exhibit anomalous hyperflexible behavior due to the energetically low-cost displacement of kinks. For instance, the motion of a single kink on a chain of length L and curvature satisfying a close to "resonance" condition $\omega_1 \approx \frac{2\pi k}{L}$ $(k = 1, 2, ..)$ expects to give rise to most dramatic end fluctuation effects.

In order to get various conformational states specified, we further calculate the JDOS for a chain of length $N = 48$ with $\omega_1 = 0.26b^{-1}$ and $\omega_3 = 0.1b^{-1}$. With the fixed mechanical ratio $B/C = 2$, the control parameter is given as $\gamma \approx 5.5 > 1$. Considering the chain length, the ground state shape of helix in 2-d is a coiled shape with exactly two turns. With given parameters, a chain forms a helix in 3-d with radius $R = 8.09b$ and pitch $P = 3.35b$. For more detailed sampling, we extended our algorithm to have three variables (E, D, n). Note that the

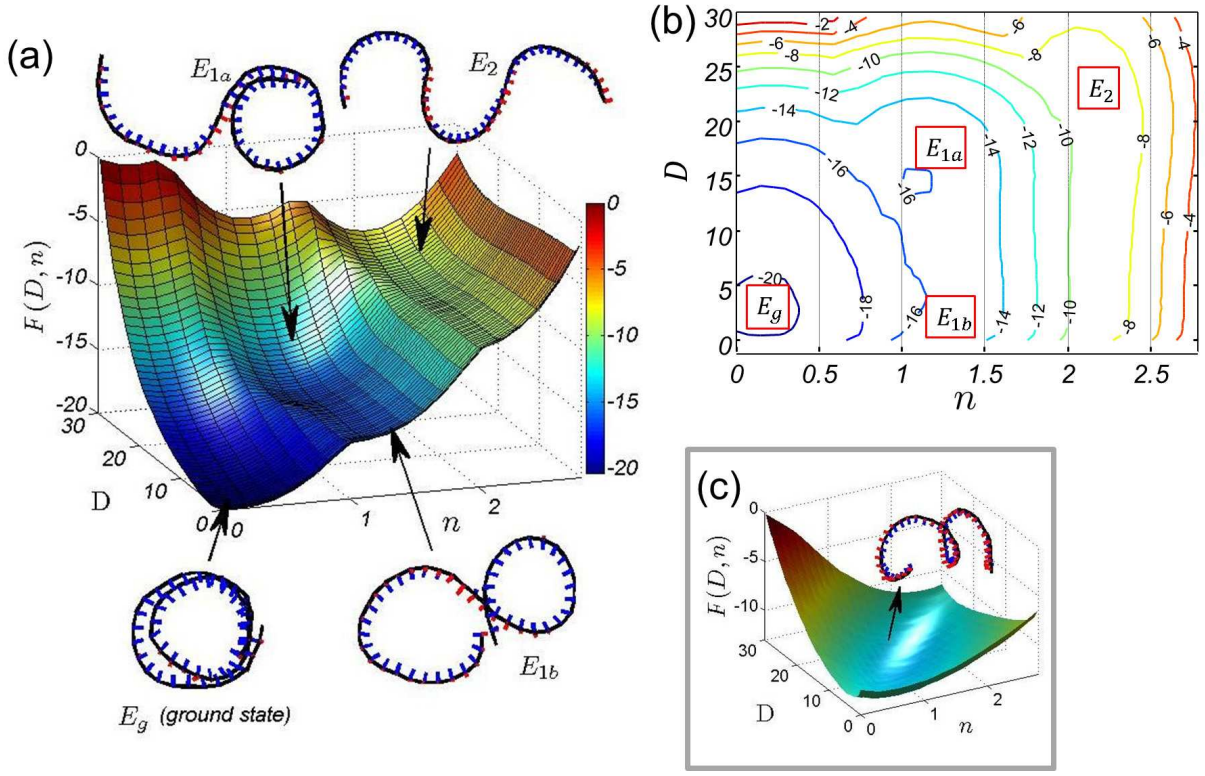

Figure 5.7: For the chain of length $N = 48$ with $\omega_1 = 0.26\, b^{-1}$ and $\omega_3 = 0.1\, b^{-1}$ yielding $\gamma = 5.47 > 1$, the ground state in 2-d is a coiled shape by two turns. Free energy is plotted as a function of the end-to-end distance D and the number of twist kinks n for (a) a helix confined in 2-d and (c) in free space of 3-d. In both graphs, the color code indicates the depth of energy, and the representative shapes of chain are shown for corresponding regions. (b) Contour plot of free energy for 2-d chain, where the numbers denote the value of free energy in the unit of $k_{\mathrm{B}}T$.

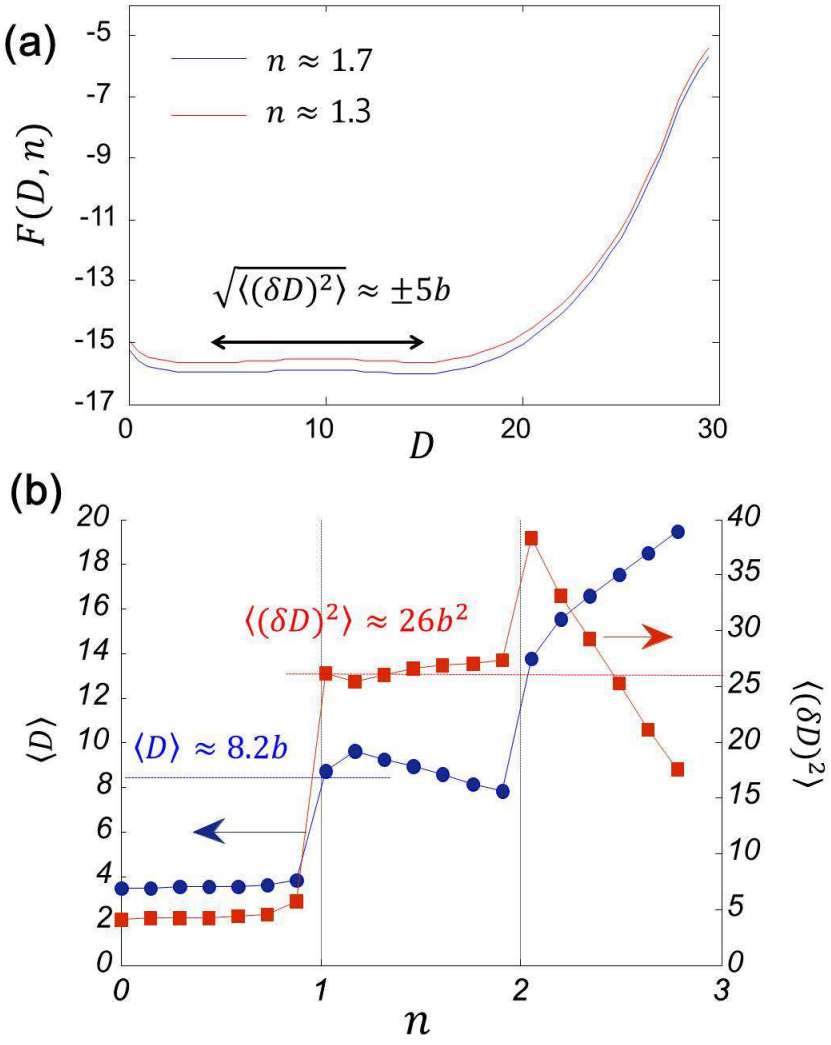

Figure 5.8: (a) Cross section plot of free energy parallel to the $F - D$ plane at $n \approx 1$ states. (b) Mean distance $\langle D\rangle$ (data in blue) and its fluctuations $\langle(\delta D)^2\rangle$ (data in red) are plotted as a function of n on dual axis graph.

number of twist-kinks n is now included in the calculation for JDOS $g(E, D, n)$. Convergence of the JDOS with three variables costs a lot of computational time, which takes about one week with same $f_{final} \approx 10^{-6}$ in the same machine. Once the JDOS is obtained, the calculation of any thermal average is straightforward. Mainly, we focus on the calculation of free energy defined as $\beta F(D, n) = -\ln\left[\sum_E g(E, D, n)e^{-\beta E}\right]$.

Figure 5.7(a) shows the free energy landscape over the $D - n$ plane. As expected, the ground state shape of the chain in 2-d is a coiled circle with exactly two turns. In addition to the ground state, the free-energy along n-axis displays the existence of "excited" metastable states with $n = 1, 2, ...$ These states with distinct n are separated by small free energy barriers, which is clearly seen in the contour plot in Fig. 5.7(b). In particular, the free energy difference between $n = 0$ and $n = 1$ state is only $\Delta F_{1kink} \approx 4\, k_{\mathrm{B}}T$. This value is not far from the theoretical estimation of one kink free energy $\Delta F_{1kink} = E_{1kink} - k_{\mathrm{B}}T \ln N \approx 6.6\, k_{\mathrm{B}}T$, where the $\ln N$ ($N = 48$) term accounts for kinks positional entropy gain along the discrete positions of the chain. As shown in Fig 5.7(c), the free energy landscape of the free chain (not confined) appears rather featureless, displaying no local minima or barriers and lacking the complexity of its confined chain counterpart.

The $n = 1$ state (cf. Fig. 5.8(b)) exhibits an enhanced end-to-end distance fluctuation $\langle(\delta D)^2\rangle$ in qualitative agreement with the mobile kink interpretation. For the given length ($L = 48b$) and curvature, we expect an almost flat free energy landscape as a function the end-to-end distance D in the range $D \in [0, D_{\max}]$. Here, $D_{\max} \approx 4\omega_1^{-1} = 15.4b$ is the maximal extension for the $n = 1$ state. It is reached when the twist-kink is located at a position $\approx L/4$ from any of the borders as seen from straightforward geometric reasoning. The standard deviation expected from analytic estimation $\langle(\delta D)^2\rangle_{n=1} \approx 28b^2$ agrees well with the simulation result $\langle(\delta D)^2\rangle_{n=1} \approx 26b^2$. The larger states $n \geq 2$ display again lower fluctuations. This is in agreement with the interpretation that with growing kink density their repulsion and eventually mutual confinement become important.

5.6 Conclusion

We have shown that the conceptually simple procedure of planar confinement transforms a simple mundane object - a helically coiled filament- into a complex metastable, and anomalously fluctuating filament. The statistical mechanics of this exotic object, the "squeelix", can be

qualitatively understood in terms of the motion of discrete particle-like entities corresponding to sharp curvature inversion points, called "twist kinks". At low twist kink concentrations, they move almost freely along the chain and induce anomalously enhanced conformational fluctuations notably deviating from WLC behavior. The "squeelical" shapes formed under confinement range from almost ideally circular to wavy depending on the value of a single dimensionless "twist expulsion" parameter $\gamma = \frac{4B\omega_1^2}{\pi^2 C\omega_3^2}$. This parameter depends both on the chain's elastic moduli (flexural modulus B and twist modulus C) and the geometric properties (intrinsic curvature ω_1 and twist ω_3). For $\gamma > 1$, the twist is curiously expelled from the chain. Under these conditions the squeelix becomes almost circular (up to minor end-effects) and the circularization probability can be dramatically enhanced. In the other limit $\gamma < 1$ the squeelix comprises densely packed twist-kinks in its ground state which is now wavy. Several authors studied the case when there is no preferred twist and the ground state is circular [141, 142].

We may speculate whether abnormal wavy shapes or enhanced closure of confined filaments found in literature are fingerprints of hidden helical superstructures whose microscopic origin should be elucidated for each type of filament, case by case. Such peculiar behavior under confinement is observed for essential filaments like microtubules [4], F-actin [115] and possibly for intermediate filaments [71]. It also has been observed that actin-filaments circularize on stunningly small scales ($\sim 5\,\mu$m length rings) [115, 143] and exhibit wavy periodic tangent-correlation functions in narrow, flat-channels (cf. Fig.6 in [144]). These phenomena cannot be understood within the naive WLC model. Similarly intermediate filaments under confinement show wiggly periodic shapes [71] suspiciously reminiscent of squeezed helices.

It is our feeling that the illustrated phenomena of multistability, hyperflexibility and enhanced closure probability are just the tip of an ice-berg. The floppy "squeelix" concept will help us to figure out the underlying mechanism on polymorphic conformations of biofilaments. We have evidence that additional lateral confinement of filaments in narrow channels, as encountered in microfluidic devices [71], further enhances the visibly wavy shapes for helical filaments and gives easier access to the underlying mechanical parameters. The potential of the 2-d and especially double confinement experiments (in microchannels) has been vastly underestimated so far. The "squeelix" phenomenology laid out here will serve us as a "dictionary" to decode these peculiar observations in forthcoming works.

Conclusion and perspectives

In this work, the dynamics of confined stabilized biofilaments has been studied. The filaments under consideration are mostly confined to 2-d surface, this provides a good tool for investigating the intrinsic mechanical properties of filaments such as DNA molecule and cytoskeleton filaments. Traditionally, such filaments have been described as an homogeneous elastic rod with a single elastic modulus, and the Worm-Like Chain (WLC) model has been successfully implemented to describe their dynamics. However, many recent experiments indicate that the WLC model may not be enough to explain the elasticity and dynamics, in particular, for the MTs' length-dependent stiffness and polymorphic dynamics for example. This eventually calls for an augmented model to describe such behaviors. In our study, the Helical WLC model (HWLC) has been employed to investigate the unusual features of MTs, and should provided a useful tool for studying other biofilaments.

The first two chapters were dedicated to the dynamics of a semiflexible polymer as a classical model for biofilaments. We studied the conformations of DNA grafted on a streptavidin coated surface on which a biotinilated vesicle spreads. The main issue here is the unraveling of the DNA coil pushed by the vesicle front. Some DNA/DNA-sections appear unable to uncoil at the imposed velocity and are overrolled. Inspired by the experiment, we have performed 2-d Langevin simulation for a semiflexible polymer in an array of obstacles closer than the persistence length. We studied early stages of reptation for a stiff chain with free ends both analytically and numerically. For a chain grafted by one end, we described relaxation via hairpin formation.

The last two chapters present the dynamics of MTs and rationalize it by the "confined HWLC" model. For the MT, image data analysis enabled us to monitor its unusual thermal motion, and revealed its cooperative polymorphic dynamics. The most controversial length-dependent stiffness has been reproduced and accounted for as a consequence of such polymorphic conformational transitions. In our work, the MTs are also confined in 2d plane, where they often displays a wavy shape. This reflects a superhelical structure of the MT in 3d. In

order to investigate the formation of such shapes, we studied the effect of 2d confinement on a generic HWLC. By using an elastic theory and Monte-Carlo simulation, the metastable states corresponding to various shapes are observed in the free energy landscape. The confined HWLC has a soft mode corresponding to the diffusion of particle-like twist-kinks, which accounts for most of the dynamics. We do not explicity discuss the origin of superhelicity which in the case of MTs may be linked to the polymorphism (curved and straight state) of the tubulin dimer associated with the intrinsic helicity of the MT lattice.

The other biofilaments like actin- and intermediate filament also exhibit anomalous structure and dynamics. Open questions about the static and dynamic features could be addressed. For actin-filament, indeed, the unusual dynamics was experimentally observed like annealing process at the end of inter/intra filaments [145] and the polymorphic switching process at the level of the actin monomer [146], which lead to large scale conformational changes. Most intriguing feature is in the formation of small actin-rings in solution confined to the surface by the depletion interaction [115]. For intermediate filament, the various shapes [38] and wavy shapes in narrow channels [71] might imply a possible helical superstructure and its polymorphism. We are left with the feeling that even stabilized biofilaments are far more complex than usually assumed.

Appendix A: Compliance J

The transverse equal time correlation $C_q = \frac{1}{\alpha S}\langle r_{\perp,q} r_{\perp,-q}\rangle$ needs to be calculated under the tension σ_q from the transverse Langevin equation:

$$\zeta_\perp \frac{\partial r_{\perp,q}}{\partial t} = -(l_p q^4 + \kappa + q^2\sigma) r_{\perp,q} + \xi_{\perp,q}, \tag{5.23}$$

with stochastic noise ξ. Here in Eq. 5.23 the tension is assumed to be uniform because the typical transverse wavelength is short [147] (in the harmonic potential, it further saturates at l_1) as compared to the longitudinal one at some time t. The corresponding equation for C_q,

$$\zeta_\perp \frac{\partial C_q}{\partial t} = -2(l_p q^4 + \kappa + q^2\sigma) C_q + 2, \tag{5.24}$$

where the additive constant 2 comes from the noise and allows for the equilibrium correlation ($\sigma_{eq} = 0$) can be solved perturbatively [147]. After Laplace Transform with respect to time we obtain:

$$C_q(p) = \frac{1}{p(\kappa + l_p q^4)} - \frac{2q^2}{(l_p q^4 + \kappa)\{2(l_p q^4 + \kappa) + p\zeta_\perp\}}\sigma, \tag{5.25}$$

where only the linear term in σ is relevant according to the definition of longitudinal coordinates. Finally $\langle \frac{\mathrm{d}\delta r_{\parallel,s}}{\mathrm{d}s}\rangle$ is related to the tension σ via the equation: $\langle \frac{\mathrm{d}\delta r_{\parallel,s}}{\mathrm{d}s}\rangle = -\frac{\alpha}{2}\int \frac{\mathrm{d}q}{2\pi} q^2 C_q(p) = J\sigma$. Performing the integration, we obtain the expression of the compliance J for two confined transverse directions ($\alpha = 2$):

$$J = \frac{l_1^3}{l_p^2} \frac{1}{2\sqrt{2}\{1 + (1+\tilde{p})^{1/4}\}\{1 + (1+\tilde{p})^{1/2}\}} \quad \text{with} \quad \tilde{p} = p\tau_e, \tag{5.26}$$

where τ_e is the entanglement time introduced earlier as $\tau_e = \zeta_\perp/2\kappa = \zeta_\perp l_1^4/2l_p$.

Appendix B: Reorientation of a semiflexible polymer

In this part, we will briefly study on relaxation of stiff chains freely rotating around the grafting point by two dimensional computer simulations and scaling argument. The main focus is on the orientational relxation of the whole chain (soft mode) and some end-section by means of the auto-correlation function $P(t) = \langle \cos\theta \rangle$ and similarly we define $P_e(t)$ for an end-section (See Fig. 5.9 for schematic description). Here, we only present them for both obstacle free space and in the presence of obstacles. In order to characterize the relaxation of the initial overall chain orientation, we define a relaxation function $P(t)$ as $\langle \cos\theta(t) \rangle$, where θ is an angle between the initial end-to-end vector $\mathbf{R}_E(0)$ and the end-to-end vector at time t, $\mathbf{R}_E(t)$. The relaxation function is computed from the simulation data as: $P(t) = \left\langle \frac{\mathbf{R}_E(t)\cdot\mathbf{R}_E(0)}{R_E(t)R_E(0)} \right\rangle$. A more detailed description can be found in Ref [148].

Reorientation of a grafted stiff chain in obstacle free space

In the soft mode, the angle θ is a Gaussian variable obeying a diffusion equation with (angular) diffusion constant $D_\theta = 3/(\zeta S L^2)$, where L is the average end-to-end distance of the chain. The correlation function is hence,

$$P(t) = P_0 \exp\left(-\frac{t}{\tau_{rot}}\right), \quad \text{where} \quad \tau_{rot} = \frac{1}{3}\zeta S L^2. \tag{5.27}$$

As the major contribution for the orientational relaxation comes from the soft mode for stiff filaments ($S < l_p$), we may approximate $P_0 \approx 1$.

Figure 5.10 shows the relaxation function $P_e(t)$ of a short end-section of length $\delta = S - s$ for a stiff filament $S = 16b$ and $\delta = 2b$. The bending modes provide about half of the relaxation,

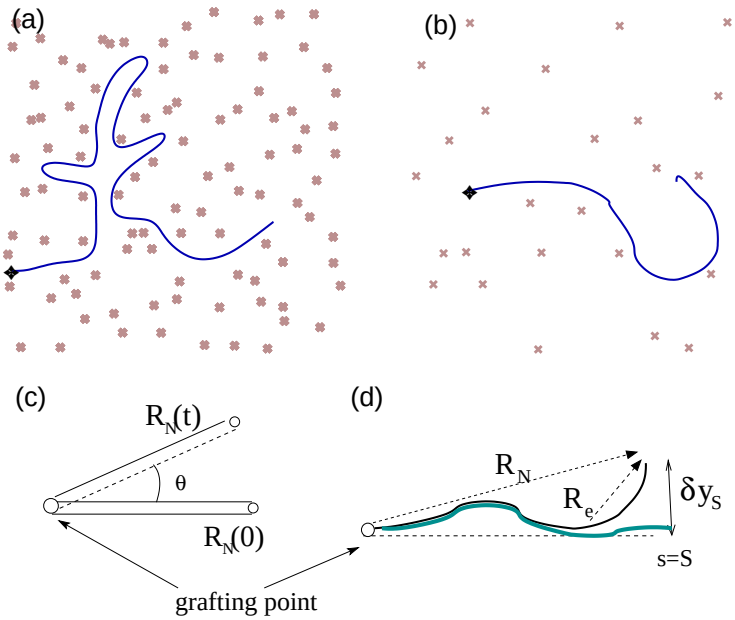

Figure 5.9: (a) Illustration of a grafted polymer chain surrounded by obstacles with many hernias (b) formation of a hairpin (c) Soft mode (d) The orientation of the whole chain R_E and end section R_e.

and the final relaxation is due to the soft overall rotation mode. A shoulder is observed where the two regimes match. There is a rather robust regime for intermediate times between the longest relaxation time of the bending modes of the short end section $\tau_\delta \approx \zeta \left(4/5\pi\right)^4 \delta^4/l_p$ and the longest relaxation time of the bending modes of the whole filament $\tau_1 \approx \zeta \left(4/5\pi\right)^4 S^4/l_p$. In this regime the relaxation is independent of the specific length of the end-section.

$$P_e(t) = 1 - \frac{1}{\Gamma[3/4]} \left(\frac{t}{\zeta l_p^3/4} \right)^{1/4} \qquad (\tau_\delta < t < \tau_1). \tag{5.28}$$

The detailed derivation can be found in Ref [148]. In Fig. 5.10(b), the predicted power-law is depicted by the log-log plot of $1 - P_e(t)$. Note that this relaxation is independent of chain length. The existence of this scale free regime for the average orientation can be understood in a simple way. Once the active bending modes have wavelength larger than some length λ, the average orientation of the end section is independent of its specific length provided that it is shorter than λ. It is then easy to recover the power $\alpha = 1/4$ in $1 - P_e(t) \sim t^\alpha$, asking for a smooth crossover between the early regime $1 - P_e(t) \sim l_p^2 \left(t/\zeta l_p^3\right)^{3/4}/\delta^2$ for $t < \tau_\delta$, similar to

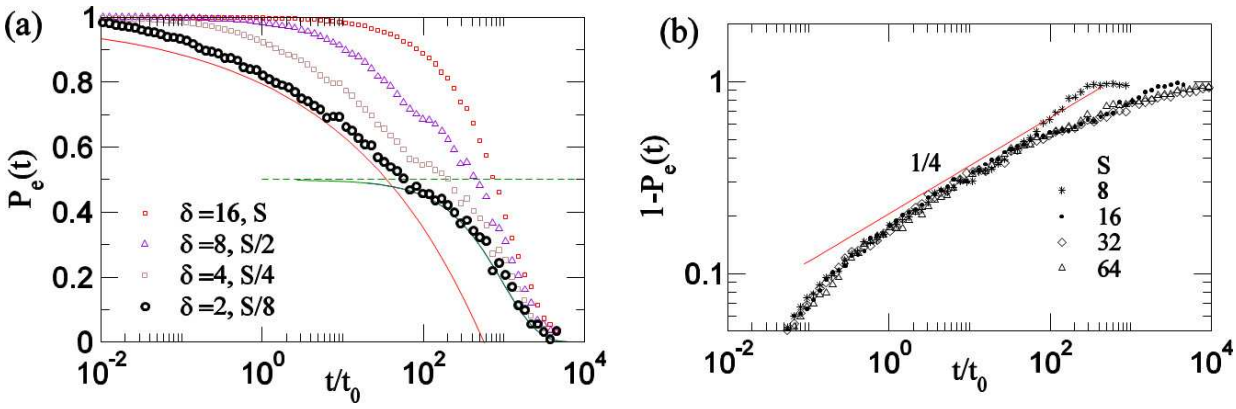

Figure 5.10: Relaxation function $P_e(t) = \langle \cos\theta \rangle$ for $N = 16$ for various end-section length δ. $P_e(t)$ for $\delta = 2b$ ($\circ$) is fitted with Eq. 5.28 (red line) describing the internal fluctuation and Eq. 5.27 describing overall chain rotation. The dashed line indicates the fitted amplitude 0.5 of the final exponential relaxation with predicted relaxation time $SL^2/3$. The measured value of L from simulation is $L = 13.5b$ for $S = 16b$.

short time regime $1 - P(t) \sim t^{3/4}$ and the scale free regime $1 - P_e(t) \sim t^{\alpha}$ for $t > \tau_\delta$ where $\tau_\delta \sim \delta^4$. Indeed the crossover scaling obeys $1 - P_e(t) = \left(t^{3/4}/\delta^2\right) F\left(t/\tau_\delta\right)$ with F an unknown scaling function and by construction $F(x) \to \text{constant}$ for $x \ll 1$. The large x asymptote must restore the scale free regime, this imposes the power law asymptotics $F \to x^{-1/2}$ hence $1 - P_e(t) \sim t^{1/4}$. The very simple result Eq. 5.28 is useful as long as $\delta \ll S$. For the special case under consideration, $S = 16, \delta = 2$ the soft mode relaxes about half of the initial correlation $\left(P(0) = 1\right)$ and $P(t) = 0.5 \exp\left(-t/\left(\zeta S L^2/3\right)\right)$.

Reorientation of a grafted stiff chain in the presence of obstacles

In the presence of obstacles, the rotational degree of freedom is strongly hindered if the obstacles are spaced closer than L. Rather than rotating the whole end-to-end vector, the chain orientation can relax by retracting part of the chain and renewing its path. The retraction through the obstacles can be established mainly via two processes: (a) small retraction by thermal fluctuation and (b) retraction upon storing extra length in activated hernias beyond typical thermal fluctuations. Activated hernias provide the late relaxation mechanism. In this section, we study only the relaxation mechanism by hernias.

When the formation of the hairpin is activated, a required nucleation time is $\tau_{nc} \sim \tau_0 e^{E_{hp}}$.

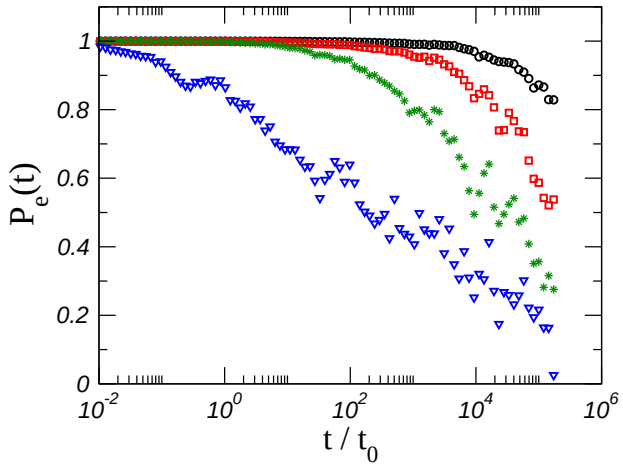

Figure 5.11: The end section relaxation function $P_e(t)$ for chain N=64 with average obstacle spacings h=7b in semi-log scale. From the top to bottom, the relaxation function $P(t)$ of the whole chain($\delta = S$), half-chain($\delta = S/2$), quarter chain ($\delta = S/4$) and end segment ($\delta = S/32$) are shown.

The nucleated hairpins can develop further against entropic force. To retract a length of s_1, the additional free energy penalty is $\epsilon_H \sim s_1/(2l_1)k_BT$ as the conformation of one strand of the double stranded loop of length $s_1/2$ is merely set by the other half. Thus the energy for retracting length s_1 via the formation of a meandering hairpin is $\epsilon_H + E_{hp}$, with $\epsilon_H = \alpha s_1/(2l_1)k_BT + E_{hp}$, where α is the proportionality constant of order unity. The time required for a hairpin with total retracted length s_1 is

$$t_h(s_1) \sim \tau_0 \exp[(E_{hp} + \epsilon_H(s_1))/k_BT]. \tag{5.29}$$

Writing s as a function of $t(s)$ and recalling that $\langle \delta y(t)^2 \rangle \sim s(t)^3/l_p$ for stiff chains ($S < l_p$), we obtain the relaxation function as

$$1 - P(t) \sim \frac{\langle \delta y^2 \rangle}{2L^2} \approx \frac{l_1^3}{l_p L^2} \left(\log \frac{t}{\tau_{nc}} \right)^3 \tag{5.30}$$

with $\tau_{nc} = \tau_0 e^{E_{hp}/k_BT}$.

For flexible chains ($S > l_p$), Eq. 5.30 holds for short times ($t < t_h(l_p)$) with $L^2 = 2Sl_p$. Somewhat larger hairpins ($s > l_p$) relax as flexible strands with $\langle \delta y_S^2 \rangle = sl_p$. The relaxation

function at times $t > t(l_p)$ is dominated by flexible hairpins ($s > l_p$) and:

$$1 - P(t) \approx \frac{l_1}{S}\left(\log\frac{t}{\tau_{nc}}\right) \tag{5.31}$$

Figure 5.11 shows the relaxation function $P_e(t)$ of end-sctions belonging to rather flexible chain $N = 64$, $l_p = 10b$ in the matrix with obstacle spacing $h = 7b$. The simulation results show that the terminal segment exhibits the short time power-law relaxation as a free chain followed by logarithmic decay as described in Eq. 5.31. By analogy with the case of the free chain, the crossover from power-law to logarithmic relaxation, indicated by the shoulder, should be located at the entanglement time τ_e for smallest end-section which is indeed of order t_0.

Appendix C: Multi-kinks solution

We start with the ansatz that the two discrete twist-kinks are separated by a distance d in such way that $\lambda \ll d \ll L$,

$$\vartheta(s) = 4\arctan(e^{(s+d/2)/\lambda}) + 4\arctan(e^{(s-d/2)/\lambda}), \tag{5.32}$$

where λ is the size of twist-kink and $\vartheta(s) = 2\psi(s) - \pi$ as described in Chap. 5. The shape of chain is then given by Eq. 5.4 as

$$\phi(s) = \omega_1 \int_0^s \sin\psi(s) ds. \tag{5.33}$$

The integration gives

$$\phi(s) - \phi(0) = -\omega_1\lambda \left[\frac{s}{\lambda} - \coth\left(\frac{d}{2\lambda}\right) \ln\left(\frac{1+e^{(d+2s)/\lambda}}{e^{d/\lambda}+e^{2s/\lambda}}\right)\right]. \tag{5.34}$$

The energy of the two twist-kinks is then given by (with $2\psi = \vartheta + \pi$)

$$E_{WLCT}[\vartheta] = \int_{-L/2}^{L/2} \left(\frac{1}{2}\tilde{A}\vartheta'^2 + \frac{\tilde{F}}{2}\vartheta^2\right) ds, \tag{5.35}$$

where $\tilde{A} = \frac{C}{4}$ and $\tilde{F} = \frac{B\omega_1^2}{4}$. The elastic energy of chain with two twist-kinks is obtained in the limit $L \to \infty$:

$$E_{2kinks} = 16\sqrt{\tilde{A}\tilde{F}} + 16\sqrt{\tilde{A}\tilde{F}}\exp(-d/\lambda) + O(\exp(-2d/\lambda)), \tag{5.36}$$

where $16\sqrt{\tilde{A}\tilde{F}}$ corresponds to the energy of two independent twist-kinks, and the interaction energy of them is given by

$$U_{int} = 16\sqrt{\tilde{A}\tilde{F}}\exp(-d/\lambda) \tag{5.37}$$

The wavy squeelix shapes obtained for $\gamma < 1$ can be described in such a way that the twist-kink density along the filament is limited by their mutual repulsion. Generally speaking, the gas of twist kink is then less compressible and the end-to-end distance fluctuations of the squeelix are weaker. It can be shown that the pair repulsion between twist-kinks decreases with their distance d as $U_{int} \sim \pi C\omega_3\sqrt{\gamma}\mathrm{f}(d/\lambda)$ with $\mathrm{f}(x) \sim 1/x$ for $x \ll 1$ and $\mathrm{f}(x) \sim e^{-x/2}$ at small $x \gg 1$. The dense twist kink regime deserves special consideration, a more detailed description explicitly involves Jacobi functions.

Bibliography

[1] F. Gittes, B. Mickey, J. Nettleton, and Jonathon Howard. Flexural rigidity of microtubules and actin filaments measured from thermal fluctuations in shape. *J Cell Biol.*, **120**(4):923–934, 1993.

[2] F. Pampaloni, G. Lattanzi, A. Jonas, T. Surrey, E. Frey, and E.-L. Florin. Thermal fluctuations of grafted microtubules provide evidence of a length-dependent persistence length. *Proc. Natl. Acad. Sci. U.S.A*, **103**:10248, 2006.

[3] K. M. Taute, F. Pampaloni, E. Frey, and E.-L. Florin. Microtubule dynamics depart from the wormlike chain model. *Phys. Rev. Lett.*, **100**:028102, 2008.

[4] P. Venier, A. C. Maggs, M.-F. Carlier, and D. Pantaloni. Analysis of microtubule rigidity using hydrodynamic flow and thermal fluctuation. *J. Biol. Chem*, **269**:13353, 1994.

[5] H. Mohrbach, A. Johner, and I. M. Kulić. Tubulin bistability and polymorphic dynamics of microtubules. *Phys. Rev. Lett.*, **105**:268102, 2010.

[6] S. Asakura, G. Eguchi, and T. Iino. Salmonella flagella: in vitro reconstruction and over-all shapes of flagellar filaments. *J. Mol. Biol.*, **16**:302, 1966.

[7] J. M. G. Cowie. *Polymers: chemistry and physics of modern material*. Nelson Thornes Ltd; 2nd edition, 1990.

[8] J.-M. Lehn. Supramolecular chemistry. *Science*, **260**:1762–1763, 1993.

[9] B. Hasenknopf, J.-M. Lehn, B. O. Kneisel, G. Baum, and D. Fenske. Self-assembly of a circular double helicate. *Angew Chem Int Ed*, **35**:1838–1840, 1996.

[10] J. Howard. *Mechanics of Motor Proteins and the Cytoskeleton*. Sinauer Associates, 2001.

[11] M. B. Omary and P. A. Coulombe. *Intermediate Filament Cytoskeleton, Volume 78 (Methods in Cell Biology)*. Academic Press, 2004.

[12] E. H. Egelman, N. Francis, and D. J. DeRosier. F-actin is a helix with a random variable twist. *Nature (London)*, **298**:131, 1982.

[13] C. Rivetti, C. Walker, and C. Bustamante. Polymer chain statistics and conformational

analysis of DNA molecules with bends or sections of different flexibility. *J. Mol. Biol.*, **280**:41, 1998.

[14] J. D. Moroz and P. Nelson. Torsional directed walks, entropic elasticity, and DNA twist stiffness. *Proc. Natl. Acad. Sci. USA*, **94**:14418, 1997.

[15] C. Bouchiat and M. Mézard. Elasticity model of a supercoiled dna molecule. *Phys. Rev. Lett.*, **80**:1556–1559, 1998.

[16] Z. Bryant, M. D. Stone, J. Gore, S. B. Smith, N. R. Cozzarelli, and C. Bustamante. Structural transitions and elasticity from torque measurements on DNA. *Nature*, **424**:338, 2003.

[17] N. Mücke, L. Kreplak, R. Kirmse, T. Wedig, H. Herrmann, U. Aebi, and J. Langowski. Assessing the flexibility of intermediate filaments by atomic force microscopy. *J. Mol. Biol.*, **335**:1241, 2004.

[18] http://www.sparknotes.com/biology/cellstructure/intracellularcomponents/section1.rhtml.

[19] http://www.biozentrum.unibas.ch/research/groups-platforms/overview/unit/schoenenberger/.

[20] P. G. de Gennes. *Scaling Concepts in Polymer Physics*. Cornell University Press, 1979.

[21] P. G. de Gennes. Reptation of a polymer chain in the presence of fixed obstacles. *J. Chem. Phys.*, **55**:572, 1971.

[22] P. Flory. *Principles of Polymer Chemistry*. Cornell University Press, Ithaca, New York, 1971.

[23] P. Pincus. Excluded volume effects and stretched polymer chains. *Macromolecules*, **9**:386, 1976.

[24] T. Odijk. The statistics and dynamics of confined or entangled stiff polymers. *Macromolecules*, **16**:1340, 1983.

[25] T. Odijk. Scaling theory of DNA confined in nanochannels and nanoslits. *Phys. Rev. E*, **77**:060901(R), 2008.

[26] M. C. Williams. Stuffing a virus with DNA: dissecting viral genome packaging. *Proc. Natl. Acad. Sci. U.S.A*, **104**:11125, 2007.

[27] S. Jun and B. Mulder. Entropy-driven spatial organization of highly confined polymers: lessons for the bacterial chromosome. *Proc. Natl. Acad. Sci. U.S.A*, **103**:12388, 2006.

[28] V. Ramakrishnan and P. B. Moore. Atomic structures at last: the ribosome in 2000. *Curr. Opin. Struct. Biol.*, **11**:144, 2001.

[29] Q. Wen and P. A. Janmey. Polymer physics of the cytoskeleton. *Current Opinion in Solid State and Materials Science*, **15**:177, 2011.

[30] M. S. e Silva, Martin Depken, B. Stuhrmann, M. Korsten, F. C. MacKintosh, and G. H. Koenderink. Active multistage coarsening of actin networks driven by myosin motors. *Proc. Natl. Acad. Sci. USA*, **108**:9408, 2011.

[31] C. P. Brangwynne, G. H. Koenderink, F. C. MacKintosh, and D. A. Weitz. Nonequilibrium Microtubule Fluctuations in a Model Cytoskeleton. *Phys. Rev. Lett.*, **100**:118104, 2008.

[32] C. P. Brangwynne, F. C. MacKintosh, S. Kumar, N. A. Geisse, J. Talbot, L. Mahadevan, K. K. Parker, D. E. Ingber, and D. A. Weitz. Microtubules can bear enhanced compressive loads in living cells because of lateral reinforcement. *J. Cell. Biol.*, **173**:733, 2006.

[33] A. D. Bicek, E. Tüzel, A. Demtchouk, M. Uppalapati, W. O. Hancock, D. M. Kroll, and D. J. Odde. Anterograde microtubule transport drives microtubule bending in LLC-PK1 epithelial cells. *Mol Biol Cell*, **20**:2943, 2009.

[34] L. A. Amos and W. B. Amos. The bending of sliding microtubules imaged by confocal light microscopy and negative stain electron microscopy. *J. Cell. Sci. Suppl.*, **14**:95–101, 1991.

[35] R. D. Vale, C. M. Coppin, F. Malik, F. J. Kull, and R. D. Milligan. Tubulin gtp hydrolysis influences the structure, mechanical properties and kinesin-driven transport of microtubules. *J. Biol. Chem.*, **269**:23769–24775, 1994.

[36] C. Lu, M. Reedy, and H. P. Erickson. Straight and curved conformations of FtsZ are regulated by GTP hydrolysis. *J. Bacteriol.*, **182**:164, 2000.

[37] F. van den Ent, L. A. Amos, and J. Löwe. Prokaryotic origin of the actin cytoskeleton. *Nature*, **413**:39, 2001.

[38] H. Herrmann and U. Aebi. INTERMEDIATE FILAMENTS: molecular structure, assembly mechanism, and integration into functionally distinct intracellular scaffolds. *Annu. Rev. Biochem*, **73**:749, 2004.

[39] J. L. Höög, S. M. Huisman, Z. Sebö-Lemke, L. Sandblad, J. Richard McIntosh, C. Antony, and D. Brunner. Electron tomography reveals a flared morphology on growing microtubule ends. *J. Cell. Sci.*, **124**:693–698, 2011.

[40] T. Sanchez, D. Welch, D. Nicastro, and Z. Dogic. Cilia-like beating of active microtubule bundles. *Science*, **333**:456–459, 2011.

[41] Z. Li, M. J. Trimble, Y. V. Brun, and G. J. Jensen. The structure of ftsz filaments in vivo suggests a force-generating role in cell division. *EMBO J.*, **26**:4694–4708, 2007.

[42] C. H. S. Aylett, Q. Wang, K. A. Michie, L. A. Amos, and J. Löwe. Filament structure of bacterial tubulin homologue tubz.

[43] W. Reisner, K. J. Morton, R. Riehn, Y. M. Wang, Z. Yu, M. Rosen, J. C. Sturm, S. Y. Chou, E. Frey, and R. H. Austin. Statics and dynamics of single dna molecules confined in nanochannels. *Phys. Rev. Lett.*, **94**:196101, 2005.

[44] S. Jun, D. Thirumalai, and B.-Y. Ha. Compression and stretching of a self-avoiding chain in cylindrical nanopores. *Phys. Rev. Lett.*, **101**:138101, 2008.

[45] D. K. Klimov, D. Newfield, and D. Thirumalai. Simulations of β-hairpin folding confined to spherical pores using distributed computing. *Proc. Natl. Acad. Sci. U.S.A*, **99**:8019, 2002.

[46] B. Maier and J. O. Rädler. Conformation and self-diffusion of single DNA molecules confined to two dimensions. *Phys. Rev. Lett.*, **82**:1911–1914, 1999.

[47] E. A. Strychalski, S. L. Levy, and H. G. Craighead. Diffusion of DNA in nanoslits. *Macromolecules*, **41**:7716, 2008.

[48] D. J. Bonthuis, C. Meyer, C. Stein, and C. Dekker. Conformation and Dynamics of DNA Confined in Slitlike Nanofluidic Channels. *Phys. Rev. Lett.*, **101**:108303, 2008.

[49] M. C. Choi, C. D. Santangelo, O. Pelletier, J. H. Kim, S. Y. Kwon, Z. Wen, Y. Li, P. A. Pincus, C. R. Safinya, and M. W. Kim. Direct Observation of Biaxial Confinement of a Semiflexible Filament in a Channel. *Macromolecules*, **38**:9882, 2005.

[50] J. Käs, H. Strey, J. X. Tang, D. Finger, R. Ezzell, E. Sackmann, and P. A. Janmey. F-actin, a model polymer for semiflexible chains in dilute, semidilute, and liquid crystalline solutions. *Biophys. J.*, **70**:609, 1996.

[51] T. T. Perkins, D. E. Smith, and S. Chu. Direct observation of tube-like motion of a single polymer chain. *Science*, **264**:819, 1994.

[52] K. Kremer and G. S. Grest. Dynamics of entangled linear polymer melts: a molecular dynamics simulation. *J. Chem. Phys.*, **92**:5057, 1990.

[53] M. L. Hisette, P. Haddad, T. Gisler, C. M. Marques, and A. P. Schröder. Spreading of bio-adhesive vesicles on DNA carpets. *Soft Matter*, **4**:828–832, 2008.

[54] O. Kratky and G. Porod. Röntgenuntersuchung gelöster fadenmoleküle (x-ray investigation of dissolved thread molecules). *Rec. Trav. Chim.*, **68**:1106–1123, 1949.

[55] D. W. Sumners and S. G. Whittington. Knots in self-avoiding walks. *J. Phys. A*, **21**:1689, 1988.

[56] S. R. Quake. Topological effects of knots in polymers. *Phys. Rev. Lett.*, **73**:3317–3320, 1994.

[57] P. G. De Gennes. Tight knots. *Macromolecules*, **17**:703, 1984.

[58] F. B. Dean, A. Stasiak, T. Koller, and N. R. Cozzarelli. Duplex DNA knots produced by Escherichia coli topoisomerase I. Structure and requirements for formation. *J. Biol. Chem.*, **260**:4975, 1985.

[59] H. A. Nash. Integration and excision of bacteriophage lambda: the mechanism of conservation site specific recombination. *Annu. Rev. Genet.*, **15**:143–167, 1981.

[60] J. C. Wang. DNA Topoisomerases. *Annu. Rev. Biochem.*, **54**:665–697, 1985.

[61] S. A. Wasserman and N. R. Cozzarelli. Determination of the stereostructure of the product of Tn3 resolvase by a general method. *Proc. Natl. Acad. Sci. U.S.A.*, **82**:1079–1083, 1985.

[62] J. H. White, K. C. Millett, and N. R. Cozzarelli. Description of the topological entanglement of dna catenanes and knots by a powerful method involving strand passage and recombination. *J. Mol. Biol.*, **197**:585, 1987.

[63] A. N. Semenov. Influence of topological constraints on polymer dynamics in dilute and semidilute θ -solutions. *J. Phys. France*, **49**:175, 1988.

[64] B. Duplantier. Statistical mechanics of polymer networks of any topology. *Journal of Statistical Physics*, **54**:581, 1989.

[65] B. Duplantier. Intersections of random walks. a direct renormalization approach. *Comm. Math. Phys.*, **117**:279, 1988.

[66] A.N. Semenov and A. Johner. Theoretical notes on dense polymers in two dimensions. *Eur. Phys. J. E*, **12**:469, 2003.

[67] C. Elie-Caille, F. Severin, J. Helenius, J. Howard, D. J. Muller, and A. A. Hyman. Straight GDP-Tubulin Protofilaments Form in the Presence of Taxol. *Curr. Biol.*, **17**:1765, 2007.

[68] T. Muller-Reichert, D. Chretien, F. Severin, and A. A. Hyman. Structural changes at microtubule ends accompanying GTP hydrolysis: information from a slowly hydrolyzable analogue of GTP, guanylyl (alpha, beta)methylenediphosphonate. *Proc. Natl. Acad. Sci. USA*, **95**:3661–3666, 1998.

[69] H. W. Wang and E. Nogales. Nucleotide-dependent bending flexibility of tubulin regulates microtubule assembly. *Nature*, **435**:911–915, 2005.

[70] H. W. Wang, S. Long, K. R. Finley, and E. Nogales. Assembly of GMPCPP-bound tubulin into helical ribbons and tubes and effect of colchicine. *Cell Cycle*, **4**:1157–1160, 2005.

[71] B. Nöding and S. Köster. Intermediate filaments in small configuration spaces. *Phys. Rev. Lett.*, **108**:088101, 2012.

[72] S. K. Lakkaraju and W. Hwang. Critical buckling length versus persistence length: What governs biofilament conformation? *Phys. Rev. Lett.*, **102**:118102, 2009.

[73] F. Pampaloni and E.-L. Florin. Microtubule architecture: inspiration for novel carbon nanotube-based biomimetic materials. *Trends in Biotechnology*, **26**:302, 2008.

[74] K. Namba and F. Vonderviszt. Molecular architecture of bacterial flagellum. *Q. Rev. Biophys.*, **30**:1, 1997.

[75] R. Kamiya and S. Asakura. Helical transformations of salmonella flagella *in vitro*. *J. Mol. Biol.*, **106**:167, 1976.

[76] E. Hasegawa, R. kamiya, and S. Asakura. Thermal transition in helical forms of salmonella flagella. *J. Mol. Biol.*, **160**:609, 1982.

[77] R. Everaers, F. Jülicher, A. Ajdari, and A. C. Maggs. Dynamic fluctuations of semiflexible filaments. *Phys. Rev. Lett.*, **82**:3717–3720, 1999.

[78] M. Doi and S. F. Edwards. *The Theory of Polymer Dynamics*. Clarendon Press, Oxford, 1986.

[79] M. Rubinstein and R. H. Colby. *Polymer Physics*. Clarendon Press, Oxford, 2003.

[80] T. Kreer, J. Baschnagel, M. Müller, and K. Binder. Monte carlo simulation of long chain polymer melts: crossover from rouse to reptation dynamics. *Macromolecules*, **34**:1105, 2001.

[81] W. Paul, K. Binder, D. W. Heermann, and K. Kremer. Dynamics of polymer solutions and melts. reptation predictions and scaling of relaxation times. *J. Chem. Phys.*, **95**:7726, 1991.

[82] K. Kremer and G. S. Grest. Simulations for structural and dynamic properties of dense polymer systems. *J. Chem. Faraday Trans.*, **88**:1707, 1992.

[83] R. Faller and F. Müller-Plathe. Chain stiffness intensifies the reptation characteristics of polymer dynamics in the melt. *ChemPhysChem*, **2**:180, 2001.

[84] S. Ramanathan and D. Morse. Simulations of dynamics and viscoelasticity in highly entangled solutions of semiflexible rods. *Phys. Rev. E*, **76**:R010501, 2007.

[85] D. Morse. Viscoelasticity of tightly entangled solutions of semiflexible polymers. *Phys. Rev. E.*, **58**:R1237, 1998.

[86] D. Morse. Viscoelasticity of concentrated isotropic solutions of semiflexible polymers. 1. model and stress tensor. *Macromolecules*, **31**:7030, 1998.

[87] D. Morse. Viscoelasticity of concentrated isotropic solutions of semiflexible polymers. 2. linear response. *Macromolecules*, **31**:7044, 1998.

[88] V. Yamakov and A. Milchev. Diffusion of a polymer chain in porous media. *Phys. Rev. E*, **55**:1704, 1997.

[89] R. Evaraers, F. Jülicher, A. Ajdari, and A. C. Maggs. Dynamic fluctuations of semiflexible filaments. *Phys. Rev. Lett.*, **82**:3717, 1999.

[90] G. Nam, A. Johner, and N.-K. Lee. Reptation of a semiflexible polymer through porous media. *J. Chem. Phys.*, **133**:044908, 2010.

[91] P. A. Thompson and S. M. Trojan. A general boundary condition for liquid flow at solid surfaces. *Nature*, **389**:360, 1997.

[92] J. F. Marko and E. D. Siggia. Stretching DNA. *Macromolecules*, **28**:8759, 1995.

[93] E. Farge and A. C. Maggs. Dynamic scattering from semiflexible polymers. *Macromolecules*, **26**:5041, 1993.

[94] R. Granek. From semi-flexible polymers to membranes: anomalous diffusion and reptation. *J. Phys. II (Paris)*, **7**:1761, 1997.

[95] L. Harnau and P. Reineker. Equilibrium and dynamical properties of semiflexible chain molecules with confined transverse fluctuations. *Phys. Rev. E*, **60**:4671, 1999.

[96] G. Nam, N.-K. Lee, and A. Johner. Drift and diffusion of a confined semiflexible chain. *Eur. Phys. J. E*, **32**:119, 2010.

[97] P. Dimitrakopoulos. Longitudinal relaxation of initially straight flexible and stiff polymers. *Phys. Rev. Lett.*, **93**:217801, 2004.

[98] P. Dimitrakopoulos. Conformational evolution of initially straight flexible and stiff polymers over extended time periods via the scaling law methodology. *J. Chem. Phys.*, **119**:8189, 2003.

[99] G. S. Grest and K. Kremer. Molecular dynamics simulation for polymers in the presence of a heat bath. *Phys. Rev. A*, **33**:3628, 1986.

[100] F. Hofling, T. Munk, E. Frey, and T. Franosch. Entangled dynamics of a stiff polymer. *Phys. Rev. E*, **77**:060904(R), 2008.

[101] F. Hofling, E. Frey, and T. Franosch. Enhanced diffusion of a needle in a planar array of point obstacles. *Phys. Rev. Lett.*, **101**:120605, 2008.

[102] T. Munk, F. Hofling, E. Frey, and T. Franosch. Effective perrin theory for the anisotropic diffusion of a strongly hindered rod. *Europhys. Lett.*, **85**:30003, 2009.

[103] H. Tao, T. Lodge, and E. D. von Meerwall. Diffusivity and viscosity of concentrated hydrogenated polybutadiene solutions. *Macromolecules*, **33**:1747, 2000.

[104] M. C. Choi, C. D. Santangelo, O. Pelletier, J. H. Kim, S. Y. Kwon, Z. Wen, Y. Li, P. A. Pincus, C. Safinya, and M. W. Kim. Direct observation of biaxial confinement of a semiflexible filament in a channel. *Macromolecules*, **38**:9882, 2005.

[105] B. Obermayer and O. Hallatschek. Coupling of transverse and longitudinal response in stiff polymers. *Phys. Rev. Lett.*, **99**:098302, 2007.

[106] F. Thüroff, B. Obermayer, and E. Frey. Longitudinal response of confined semiflexible polymers. *Phys. Rev. E*, **83**:021802, 2011.

[107] T. B. Liverpool and A. C. Maggs. Dynamic scattering from semiflexible polymers. *Macromolecules*, **34**:6064, 2001.

[108] D. Cuvelier and P. Nassoy. Hidden dynamics of vesicle adhesion induced by specific stickers. *Phys. Rev. Lett.*, **93**:228101, 2004.

[109] N.-K. Lee and S. P. Obukhov. Diffusion of a polymer chain through a thin membrane. *J. Phys. II (Paris)*, **6**:204, 1996.

[110] N.-K. Lee, C. Abrams, A. Johner, and S. P. Obukhov. Arrested swelling of highly entangled polymer globules. *Phys. Rev. Lett.*, **90**:225504, 2003.

[111] M. Adam and M. Delsanti. Viscosity and longest relaxation time of semi-dilute polymer solutions: II. theta solvent. *J. Phys. France*, **45**:1513, 1984.

[112] C. R. Calladine. Construction of bacterial flagella. *Nature (London)*, **255**:121, 1975.

[113] P. G. Leiman, P. R. Chipman, V. A. Kostyuchenko, V. V. Mesyanzhinov, and M. G. Rossmann. Three-Dimensional Rearrangement of Proteins in the Tail of Bacteriophage T4 on Infection of Its Host. *Cell*, **118**:419, 2004.

[114] J. W. Shaevitz, J. Y. Lee, and D. A. Fletcher. Spiroplasma Swim by a Processive Change in Body Helicity. *Cell*, **122**:941, 2005.

[115] T. Sanchez, I. M. Kulić, , and Z. Dogic. Circularization, Photomechanical Switching, and a Supercoiling Transition of Actin Filaments. *Phys. Rev. Lett.*, **104**:098103, 2010.

[116] H. Mohrbach, A. Johner, and I. M. Kulić. Cooperative lattice dynamics and anomalous fluctuations of microtubules. *Eur. Biophys. J.*, **41**:217, 2012.

[117] M. B. Smith, H. Li, T. Shen, X. Huang, E. Yusuf, and D. Vavylonis. Segmentation and tracking of cytoskeletal filaments using open active contours. *Cytoskeleton*, **67**:693, 2010.

[118] C. R. Calladine. Design requirements for the construction of bacterial flagella. *J. Theor. Biol.*, **57**:469, 1976.

[119] S. Maki-Yonekura, K. Yonekura, and K. Namba. Conformational change of flagellin for polymorphic supercoiling of the flagellar filament. *NAT STRUCT MOL BIOL*, **17**:417, 2010.

[120] C. P. Brangwynne, F. C. MacKintosh, and D. A. Weitz. Force fluctuations and polymer-

ization dynamics of intracellular microtubules. *Proc. Natl. Acad. Sci. U.S.A.*, **108**:16128, 2007.

[121] J. Mizushima-Sugano, T. Maeda, and T. Miki-Noumura. Flexural Rigidity of Single Microtubules Estimated from Statistical Analysis of Their Contour Lengths and End-to-End Distances. *Biochim. Biophys. Acta.*, **755**:257, 1983.

[122] B. Mickey and J. Howard. Rigidity of microtubules is increased by stabilizing agents. *J. Cell Biol.*, **130**:909, 1995.

[123] H. Felgner, R. Frank, and M. Schliwa. Flexual rigidity of microtubules measured with the use of optical tweezers. *J Cell Sci.*, **109**:509, 1996.

[124] A. Vinckier, C. Dumortier, Y. Engelborghs, and L. Hellemans. Dynamical and mechanical study of immobilized microtubules with atomic force microscopy. *J. Vac. Sci. Technol.*, **B 14**:1427, 1996.

[125] P. J. D. Pablo, I. A. T. Schaap, F. C. Mackintosh, and C. F. Schmidt. Deformation and Collapse of Microtubules on the Nanometer Scale. *Phys. Rev. Lett.*, **91**:098101, 2003.

[126] X. (Edward) Li, K. C. Holmes, W. Lehman, H. Jung, and S. Fischer. The shape and flexibility of tropomyosin coiled coils: implications for actin filament assembly and regulation. *J. Mol. Biol.*, **395**:327, 2010.

[127] C. W. Wolgemuth, Y. F. Inclan, J. Quan, S. Mukherjee, G. Oster, and M. A. Koehl. How to make a spiral bacterium. *Phys. Biol.*, **2**:189, 2005.

[128] H. C. Berg and R. A. Anderson. Bacteria swim by rotating their flagellar filaments. *Nature*, **245**:380, 1973.

[129] A. Volodin, M. Ahlskog, E. Seynaeve, and C. Van Haesendonck. Imaging the elastic properties of coiled carbon nanotubes with atomic force microscopy. *Phys. Rev. Lett.*, **84**:3342, 2000.

[130] S. M. Douglas, J. J. Chou, and W. M. Shih. From the cover: dna-nanotube-induced alignment of membrane proteins for NMR structure determination. *Proc. Natl. Acad. Sci. U.S.A.*, **104**:6644, 2007.

[131] R. Martel, H. R. Shea, and P. Avouris. Rings of single-walled carbon nanotubes. *Nature*, **398**:299, 1999.

[132] F. A. Aldaye, P. K. Lo, P. Karam, C. K. McLaughlin, G. Cosa, and H. F. Sleiman. Modular construction of dna nanotubes of tunable geometry and single- or double-stranded character. *Nat. Nanotechnol.*, **4**:349, 2009.

[133] E. D. Sone, E. R. Zubarev, and S. I. Stupp. Semiconductor nanohelices templated by

supramolecular ribbons. *Angew. Chem. Int. Ed.*, **41**:1705, 2002.

[134] J. F. Currie, J. A. Krumhans, A. R. Bishof, and S. E. Trullinger. Statistical mechanics of one-dimensional solitary-wave-bearing scalar fields: exact results and ideal-gas phenomenology. *Phys. Rev. B.*, **22**:477, 1980.

[135] I. M. Kulić, H. Mohrbach, R. Thaokar, and H. Schiessel. Equation of state of looped DNA. *Phys. Rev. E*, **75**:011913, 2007.

[136] K. J. Böhm, R. Stracke, W. Vater, and E. Unger. *Inhibition of kinesin-driven microtubule motility by polyhydroxy compounds*. In Micro- and Nano-structures of Biological Systems (eds. Hein H-J, Bischoff G) Shaker Verlag Aachen, 2001.

[137] F. Wang and D. P. Landau. Efficient, Multiple-Range random walk algorithm to calculate the density of states. *Phys. Rev. Lett.*, **86**:2050, 2001.

[138] D. Chrétien, F. Metoz, F. Verde, E. Karsenti, and RH Wade. Lattice defects in microtubules: protofilament numbers vary within individual microtubules. *J. Cell. Biol.*, **117**:1031, 1992.

[139] G. Chirico and J. Langowski. Kinetics of DNA supercoiling studied by brownian dynamics simulation. *Biopolymers*, **34**:415, 1994.

[140] C. Zhou, T. C. Schulthess, S. Torbrugge, and D. P. Landau. Wang-Landau algorithm for continuous models and joint density of states. *Phys. Rev. Lett.*, **96**:120201, 2006.

[141] T. Charitat and B. Fourcade. Metastability of a circular o-ring due to intrinsic curvature. *Eur. Phys. J. B*, **1**:333, 1998.

[142] S. K. Ghosh, K. Singh, and A. Sain. Effect of intrinsic curvature on semiflexible polymers. *Phys. Rev. E*, **80**:051904, Nov 2009.

[143] J. X. Tang, J. A. Käs, J. V. Shah, and P. A. Janmey. Counterion-induced actin ring formation. *Euro. Biophys. J.*, **30**:477, 2001.

[144] S. Köster, D. Steinhauser, and T. Pfohl. Brownian motion of actin filaments in confining microchannels. *J. Phys. Condens. Matter*, **17**:4091, 2005.

[145] D. Popp, A. Yamamoto, and Y. Maéda. Crowded surfaces change annealing dynamics of actin filaments. *J. Mol. Biol.*, **368**:365, 2007.

[146] J. Kozuka, H. Yokota, Y. Arai, Y. Ishii, and T. Yanagida. Dynamic polymorphism of single actin molecules in the actin filament. *NAT CHEM BIOL*, **2**:83, 2006.

[147] I. A. Nyrkova and A. N. Semenov. Dynamic scattering of semirigid macromolecules. *Phys. Rev. E*, **76**:011802, 2007.

[148] G. Nam, A. Johner, and N.-K. Lee. Relaxation of a semiflexible grafted polymer. *J.*

Chem. Phys., **133**:164901, 2010.

List of Figures

Dynamics of confined biofilaments

Thèse soutenue par Gi-Moon Nam le 28 Septembre 2012 (Université de Strasbourg)

Résumé

Cette thèse est consacrée à la mécanique et à la mécanique statistique de biofilaments/biopolymères et de leur modèle le plus répandu le Worm-Like Chain (WLC) qu'il s'avère nécessaire d'étendre. Nous étudions WLC à 2-d en présence d' obstacles plus proches que la longueur de persistance. Nous caractérisons le mouvement aux temps courts par des simulations numériques complétées par des calculs analytiques. Des concepts similaires servent à décrire des ADN greffés balayés par le front d'une vésicule en cours d'étalement, l'adhésion de la vésicule est promue par des paires biotine/streptavidine qui contraignent les molécules d'ADN sur des chemins étroits où ils peuvent être imagés. Les microtubules (MT) ici stabilisés au taxol, présentent par contre certains comportements qui échappent au WLC et doivent être ramenés à leur structure interne : i)les déflexions latérales d'un MT attaché par un bout correspondent à une longueur de persistance apparente qui augmente avec la longueur ii) les MT adoptent des formes super-hélicoïdales. Ces deux points sont établis au moyen d'analyses de forme des MT. Des transitions de forme corrélées le long du MT mises en évidence sont compatibles avec un modèle basé sur la bistabilité du dimère de tubuline. Finalement un modèle de chaîne super-hélicoïdale comprenant une courbure et une torsion spontanées élargi le WLC. Confiné à 2-d, HWLC peut adopter un état fondamental circulaire ou sinueux caractérisé par le nombre de points d'inflexion où se concentre la torsion (twist-kink). Dans le cas circulaire, il existe des états métastables proches, à petit nombre de twist-kinks, hyperflexibles.

Summary

This PhD is devoted to the mechanics and statistical mechanics of biofilaments and their most widespread model, the Worm-Like Chain (WLC) model, which, as it turns out, needs to be extended. We study the WLC in 2-d in the presence of obstacles closer than their persistence length. We characterize the short time motion by numerical simulations complemented by analytical calculations. Similar concepts serve to describe grafted DNAs swept by the front of a spreading vesicle whose adhesion is promoted by biotin/streptavidin bonds, which constrain the DNAs on narrow paths where they can be imaged. Microtubules (MT), here stabilized by taxol, show features which cannot be rationalized by the WLC and shall be related to their internal structure : i)lateral deflections of a clamped MT correspond to an effective persistence length growing with the MT size ii) MT adopt super-helical shapes. These two points are proven by refined image analysis. We analyze shape transitions correlated along the MT which are compatible with a model based on dimer bi-stability. Finally, a super helical chain model (HWLC) allowing for spontaneous curvature and twist is developed which extends the WLC. When confined to 2-d, the HWLC can adopt a ground state which is circular or wavy with inflection points where twist accumulates, so-called twist-kinks. In the circular case there exist close metastable states, with a small number of twist-kinks, which are hyper-flexible.

Keywords: polymer fibres, porous materials, reptation dynamics, self-entanglement, confined filament, superhelical filament, hyperflexibility, length-dependent stiffness of microtubules